CALIFORNIA STATE POLYTECHNIC UNIVERSITY, POMONA
THESIS ELECTRONIC SIGNATURE PAGE

Submitted: Term Fall Year 2021
Bronco ID: 009591361
Email Address: andrewg2@cpp.edu

THESIS INFORMATION

THESIS TITLE	LANDSLIDE FAILURES ALONG MT. BALDY ROAD AND TESTING OF METHODS TO BACK CALCULATE
AUTHOR	Andrew Garcia
PROGRAM	Geology, M.S.

SIGNATURES

Jonathan Nourse
Committee Chair Name
Thesis Committee Chair
Position
Geological Sciences
Department
Organization

DocuSigned by:
Jonathan Nourse
562E96F6E80E44B...
12/14/2021
Signature
janourse@cpp.edu
Email

Nicholas Van Buer
Committee Member 2 Name
Thesis Committee Member
Position
Geological Sciences
Department
Organization

Signature
njvanbuer@cpp.edu
Email

Stephen Osborn
Committee Member 3 Name
Thesis Committee Member
Position
Geological Sciences
Department
Organization

Signature
sgosborn@cpp.edu
Email

Upload Thesis Attachment:

LANDSLIDE FAILURES ALONG MT. BALDY ROAD AND TESTING OF METHODS TO BACK CALCULATE SAFETY FACTOR

A Thesis

Presented to the

Faculty of

California State Polytechnic University Pomona

In Partial Fulfilment

Of the Requirements for the Degree

Master of Science

In

Geology

By

Andrew Garcia

2021

SIGNATURE PAGE

THESIS: LANDSLIDE FAILURES ALONG MT. BALDY ROAD AND TESTING OF METHODS TO BACK CALCULATE SAFETY FACTOR

AUTHOR: Andrew Garcia

DATE SUBMITTED: Fall 2021

Department of Geological Sciences

Dr. Jonathan Nourse
Thesis Committee Chair
Geological Sciences _____

Dr. Nicholas Van Buer
Geological Sciences _____

Dr. Stephen Osborn
Geological Sciences _____

ACKNOWLEDGEMENTS

I would like to express my thanks to the Geology Department at Cal Poly Pomona for helping me on my journey as both an undergrad and grad student. I would like to first thank Dr. Nourse for helping me out throughout different parts of my journey at Pomona and assisting me on the unique challenges presented by this thesis. My mom for always being there for me with a word of encouragement and helping to take data when the terrain was rough. I also would like to thank her for being there at all times whenever I needed a word of encouragement or to point out questions to things that I did not see. I would like to thank Emmons McKinney for her help when going out to the field and also the hours we spent together to figure out special ways to use ArcGIS. I also would like to give thanks to all of the professors here in the geology department who provided guidance and knowledge to help me navigate through this journey.

ABSTRACT

The area around Mt. Baldy Road to the west of the San Antonio Canyon within the San Gabriel mountains is an area which has had a multitude of both small and large scale landslide failures during its history. The purpose of my study is to look at three small events (LS1, LS2 and LS3) that happened recently and investigate different methods to back calculate their safety factor parameters. I completed eleven trips to the area measuring orientations of fractures with the help of a GPS to constrain locations. Fractures plotted on stereonets revealed features needed to assess slope stability. A laser rangefinder was used in conjunction with ArcGIS to create high-resolution topographic maps in the areas near the landslides. These maps and related data manipulations facilitated volume calculation of debris cones and allowed me to estimate the missing volume at LS1 site.

Observations and measurements from the area helped to determine the most likely failure geometries for LS1, LS2 and LS3 so that the appropriate safety factor could be applied to each unique case. Solving the volume of the debris cones of the different slides was complicated in that the roadcut in front of the failures was generally about 70 degrees of dip necessitating the use of complex formulas for the cones. Failure sites generally had multiple failures over time so the original surface may have been masked or lost. Safety factor equations from Hoek and Bray (1981) and Wyllie and Mah (2004) were used to solve for wedge failure at LS1 and LS2 for conditions for friction only (cohesion = 0); also, conditions that included cohesion and/or the presence of water. Back calculation of these equations for SF=1 yielded a range of possible cohesion values (C= 0 to 186 lbs/ft^2 (8.91kN/m^2)) and friction angles (Φ= 35.7 to 7) that in combination could have produced the observed failures at LS1 and LS2. Safety factor equations from the previously

mentioned authors were used to calculate it for LS3 under wet and dry conditions with two different surface areas since it was possible that some of the surface area was obscured. Back calculation for the smaller area for SF=1 yielded possible cohesion values (C = 0 to 625 lbs/ft^2 (29.93 kN/m^2)) and friction angles (Φ= 39.6 to 7) that in combination could have produced the observed failure. Back calculation for the larger area for SF=1 yielded possible cohesion values (C = 0 to 509 lbs/ft^2 (24.37 kN/m^2)) and friction angles (Φ= 42 to 7) that in combination could have produced the observed failure.

TABLE OF CONTENTS

LIST OF TABLES

LIST OF FIGURES

CHAPTER 1: INTRODUCTION

1.1 Purpose and Objectives

The purpose of my study is to investigate three small-scale landslides along parts of Mt. Baldy Road by using various surveying and measuring techniques alongside computer programs for modeling. Exploration of these failures will employ field mapping, stereonet analysis, ArcGIS and safety factor calculations using different methods. The primary goal is to see if reasonable cohesion and friction values can be back calculated using conventional safety factor equations. A secondary goal is to gather data points using a laser range finder to create a 3D model of the wedge landslide in order to create a new method by which missing volume can be calculated. Understanding of the field area will be accomplished through the following objectives:

A. Mapping and noting the location of various small-scale landslides along Mt. Baldy Road with use of a GPS.

B. Taking measurements of foliations, fractures, rakes and other notable geologic features with use of a Brunton Compass while noting locations with both GPS and cross referencing with a field map.

C. Plotting all measurements onto a map base in ArcGIS.

D. Creating stereonets in the local areas along Mt. Baldy Road to discern fracture/foliation interactions in the mountainside determine the orientations of these geologic features and determine if there are other areas of potential failure.

E. Using photos taken across a period of time to determine if further failures have occurred as well as to gain a general idea of the debris cones produced by the landslides.

F. Using a laser range finder to create a data set by which 3D images could be formed of the landslides and imported into ArcGIS to calculate the missing displaced volume within the failure areas.

G. Back-calculating of appropriate safety factor formulas depending on the landslide type to understand the different cohesion and friction values which could have been in play to cause the failure.

Accomplishment of these objectives should result in a general understanding of the complex nature of fracture interactions that caused the failures along Mt. Baldy Road. Usage of the 3D modeling will allow for a more accurate determination of the volume of the slides and determination of the values utilized in the safety factor calculations.

1.2 Location and Access

My field site for this research is located within the eastern San Gabriel Mountains of Southern California about 35 miles east of Los Angeles and 11.5 miles north northeast of Pomona. This area contains primarily igneous and metamorphic rocks that are both fractured as well as faulted to a high degree with many deposits being out of place resulting in a plethora of landslides which are visible up and down Mt. Baldy Road (Fig. 1). The three landslides are located on the western side of the road with one being north of the parking area and two to the south of it.

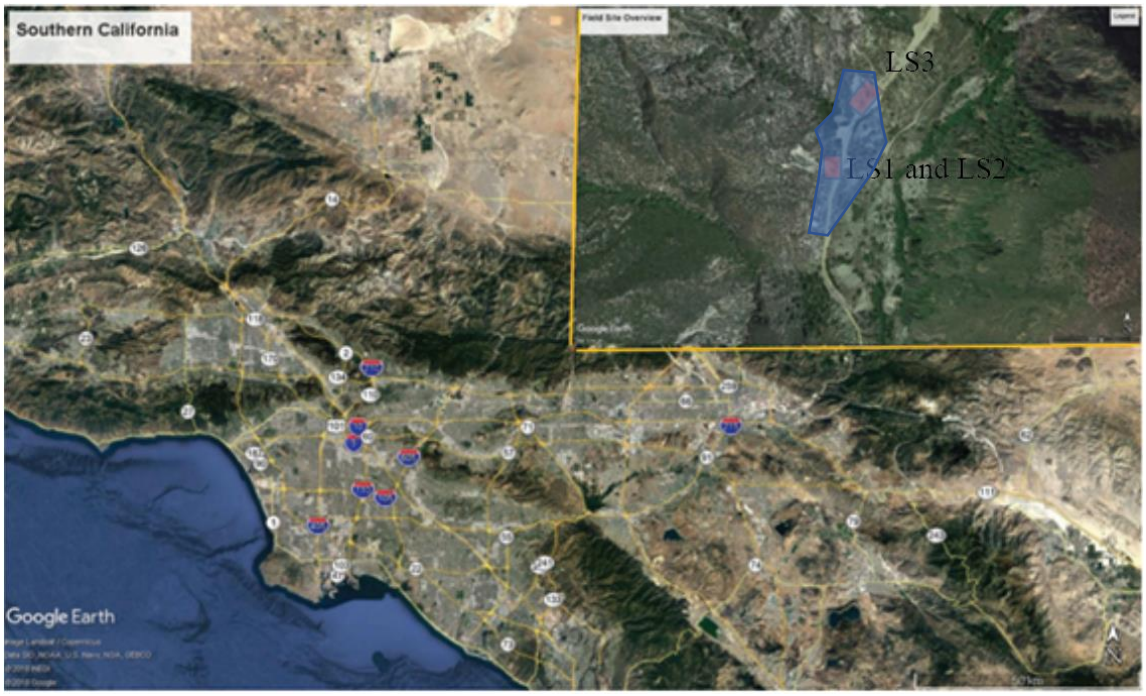

Figure 1: Overview of California with field site blown up and highlighted in blue. LS sites in orange. SW corner of inset is location on larger scale map.

Most of the field site is accessible using Mt. Baldy Road and the Sierra Powerhouse access road which branches down into San Antonio Canyon. Much of the field site has high topographic relief which makes hiking up the slopes difficult, if not impossible, without risking the safety of myself and others who happen to accompany me during the research therefore much of the data collected is closer to the base of the slopes. There are no other barriers to entry save for the potential risk of wildfires in the area due to the dry climate of Southern California which caused the occasional closure of Mt. Baldy Road. On one occasion I was turned away due to an accident that had occurred further up the road which had closed it since it is only two lanes wide and has the potential of no traffic being able to pass through the scene. Wintertime also can prove to be treacherous due to low temperatures leading to the formation of black ice so that the closure of the road to vehicles without chains is necessitated.

1.3 Regional Geologic Setting

The study area for the project is within the Eastern San Gabriel Mountains with it being in the San Antonio Canyon. Here there are many unique features due to the geologic setting in which it has formed over time. The Eastern San Gabriel Mountains are part of a larger range called the Transverse Ranges which runs from east to west and came into existence due to the compressional forces due to the bend in the San Andreas fault which is located just north of the mountains. Much of the area have formed steep mountains due to continuous pressure causing folding and faulting which can be seen in much of the ranges, causing large sections that are susceptible to landslides and general instability. Much of the research area contains Precambrian felsic gneiss and some parts of Cretaceous quartz diorite.

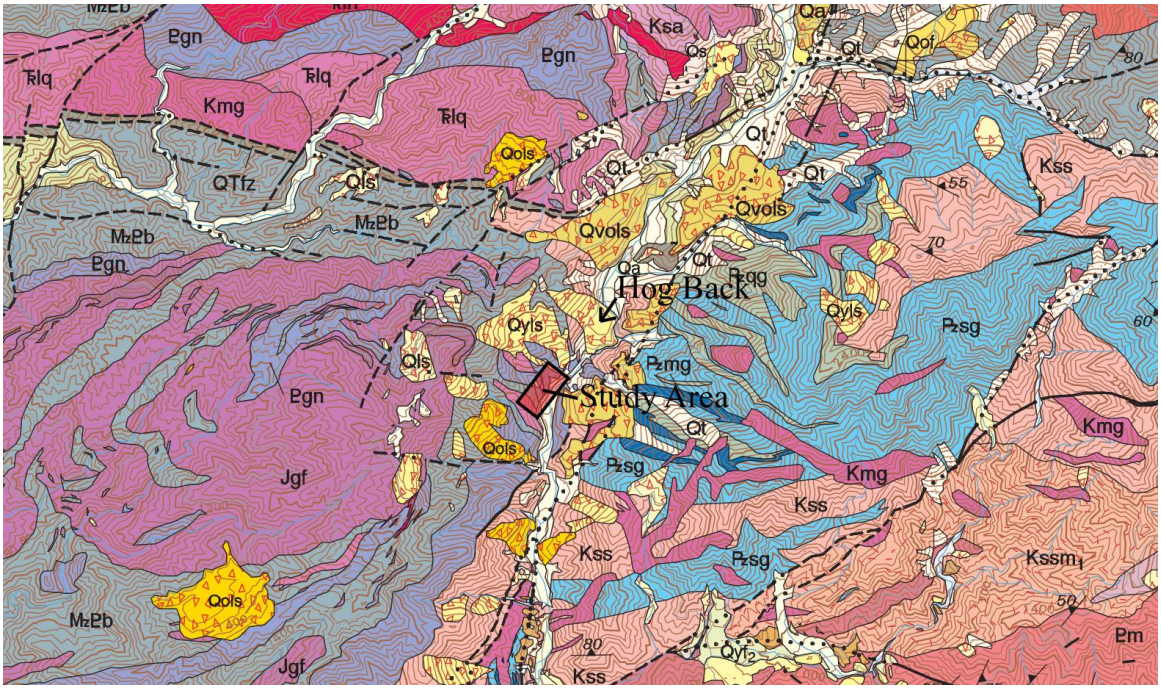

Figure 2: Overall geologic map showing the gneiss, quartz diorite and landslides in the area (Morton et. al., 2003). Study area shown in red.

1.4 Previous Research

Along this portion of the San Gabriel Mountains there have been several previous failures within close proximity to the wedge landslide being researched currently. One of these landslides is the Hog Back Landslide (Fig. 3; Herber 1987). Though this landslide was a bit different in that it was a translational landslide, it is still derived from the same crystalline rock as the wedge landslide that occurred just a few years ago. Both landslides occurred in rocks that were gneissic and strongly foliated. Hog Back is on a slope of about 31 degrees and the layering within the gneiss dips between 30 to 45 degrees to the south (Herber, 1987; Agunwah, 2020). Looking towards the north at the Hog Back Landslide from the current field site, you can see the large scale of moved material, how it affected the stream, and shift in topography. It is significant in that it allowed for the study of fresh surfaces in the scar area (Fig. 3) which is important in determining some of the parameters to calculate a rough safety factor under various conditions (Agunwah, 2020).

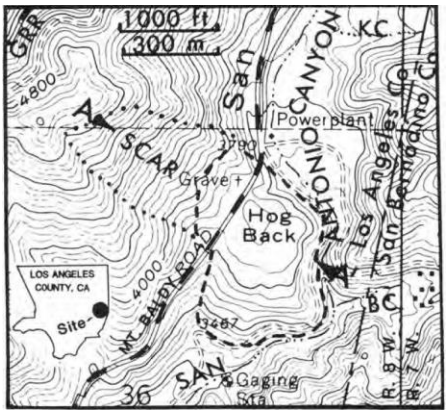

Figure 3: Mini map of the Hog Back landslide which is less than a kilometer north of the current study area (Herber, 1987).

Both hornblende-plagioclase gneiss and biotite-plagioclase gneiss are seen along Mt. Baldy Road near Hogback slide as well as in the landslides of my study area with the former being the more predominant one. There are also a lot of slickensided surfaces that

are coated in epidote and show the different trajectories in which those rocks were moving at different points throughout more recent geologic times. Most of these would be along faults that are seen throughout the region due to deformational events. Some of these would indicate the direction that these rocks have travelled to give an idea of the overall direction that they travelled.

The Sunset Peak Landslide was another one that developed in close proximity to the current wedge landslide (Rogers et. al., 1992; Fig. 4). Like the aforementioned one, the gneiss dipped to the south and into slope about 31 degrees and bears many similarities with the other landslides allowing for the assumption that this general dip to the south-southwest is characteristic of the area. The only difference being if it was into or out of slope. Friction angles of 40 degrees for rock to rock with slightly undulatory joints, 30 degrees for rock to rock with smooth planar joints and 25 degrees for discontinuities filled with epidote. These values seem to have been assigned based off observations and not experiments. What caused this landslide was the dip of the joints of about 50 degrees to the west allowing for it to overcome the friction that would hold back the sliding mass. This was a multistage landslide that had different components to it. According to a paper by Rogers et al. (1998), there were three main components to this specific failure involving the toppling of some of the jointed rocks followed by wedge events. It was suspected that these wedge events put material at the toe of the main landslide which slowed down the overall creep. This only lasted for some time until the stalling affect caused by the wedges was overcome by the inter-block strain. It is believed what helped to overcome the effect of these wedges within the blocks was some paleoseismic event (Herber, 1991).

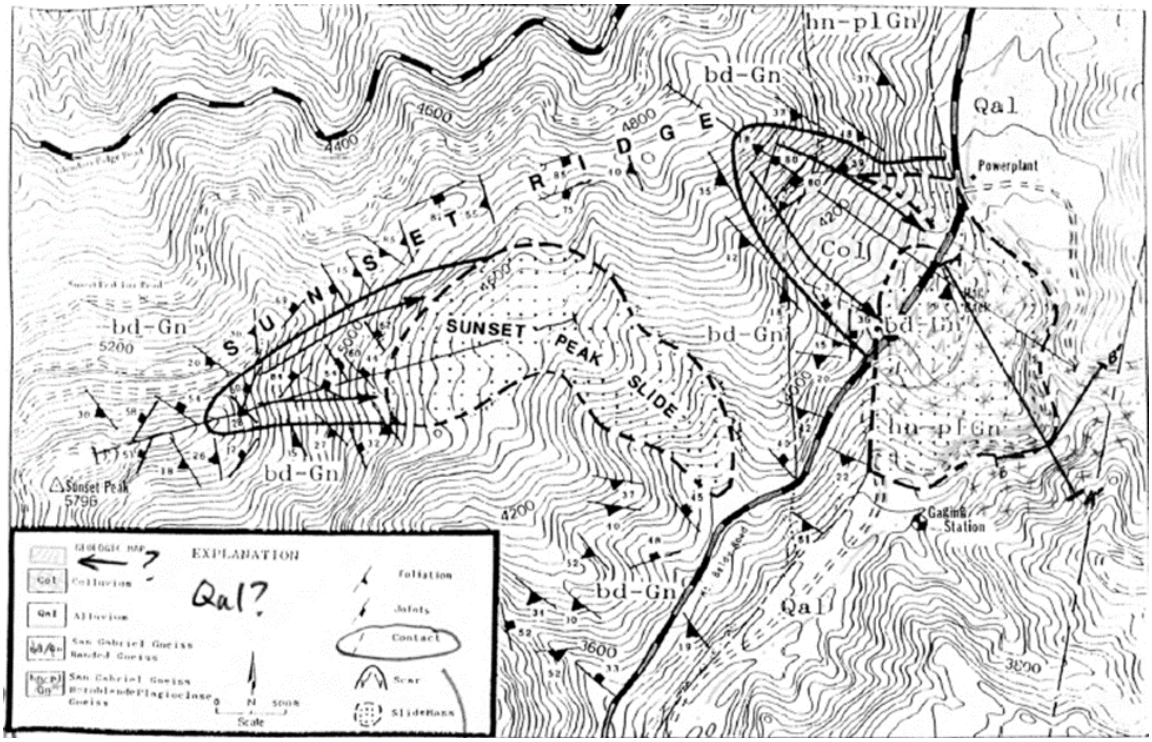

Figure 4: This is a topographic overview of the area showing two large landslides near the research area. (Rogers et al., 1992)

A thesis by Agunwah in 2020 provided some of the ways in which calculations could be executed on landslide debris. He was able to look at the dimensions from drawings by Herber, (1987) which allowed him to estimate the volume of the slide by using a more rectangular prism method so he could estimate both the area and the volume with the average width being used. Most of these numbers were average numbers and approximates in order to calculate reasonable values for the slide area, width and height that yielded good results for the cohesion and friction numbers in the safety factor calculations.

There has been other research done within crystalline rock landslides in other parts of the world which may have certain applications for the wedge failure that occurred in the Mt. Baldy area. An example of a modern-day event which has been carefully monitored and characterized is one in Preonzo, Switzerland (Gschwind, 2019). Though the location

is different, there are some striking similarities in how this landslide has been failing in comparison to the hypothesized mechanics of failure in the San Gabriel Mountains landslides, with the most notable being the interactions between the tension fractures and slide surfaces (Fig. 5). Toppling was observed prior to the start of the more significant events which caused for the current massive sliding events. Like the one suspected for the Sunset Peak, this toppling created wedges which did stabilize the landslide temporarily but would be overcome in a similar way. What was interesting from this event that may be applicable to the current research of the wedge landslide on Mt. Baldy Road are the various orientations of tension cracks and fractures within the crystalline rock. Tension cracks and fractures played a critical role in how the landslide would fail. Some led to toppling failures which has also been observed at the current field site.

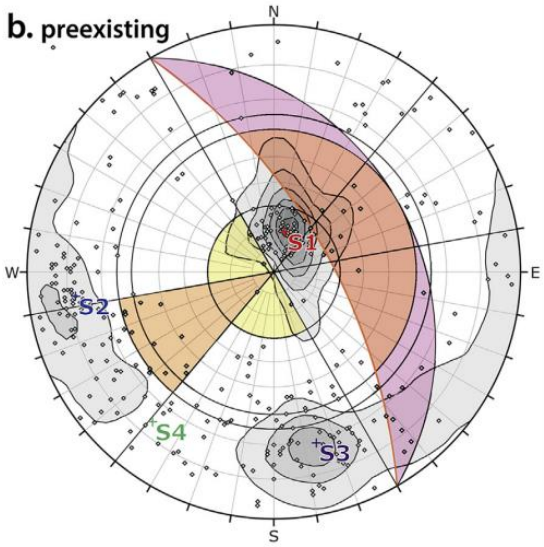

Figure 5: A sample stereonet from research done on a modern crystalline landslide in Switzerland (Gschwind, 2019). S1, S2, S3, and S4 on the + symbols are the average of the four fracture sets seen in the area. Poles here represent critical intersection zones with those in the red zone being critical for wedge sliding. Those in orange and yellow are the areas of potential toppling.

In the case of the landslide in Switzerland, there were four sets of distinct tension cracks, fractures and gravitational discontinuities (Gschwind, 2019). The interactions between these four fractures and the gneiss foliations caused for the toppling as well as

wedge failures to occur. Wedge failures here are mostly tetrahedral in character which is different from the one currently under investigation at Mt. Baldy which seems to be more simplistic geometrically since it was more like a triangular prism. Despite this, investigating the different fractures may prove useful in providing further insight into the relationship between them, faults and the natural foliation of the gneiss in the Mt. Baldy wedge failure.

1.5 Research Questions and Hypothesis

My investigation will evaluate the following hypothesis: Specially orientated fracture and fault systems are the cause of repeated small-scale failures along Mt. Baldy Road. Back calculation of the different safety factor equations can yield reasonable shear strength parameters for C and Φ that allow one to see how these and other variables like water affect the safety factor itself.

Research questions related to my hypothesis include:

1. What are the predominant fracture orientations along the road cut at each of the failure sites? Understanding the orientations will allow for knowing how these interact with one another.
2. Can past landslides be modeled as simple plane, wedge, or complex combinations of these? Modeling will allow for knowledge of how these landslides generally happen and the style they fail in.
3. What are the likely quantitative effects of water saturation during heavy storm events? It is well understood that water pressure and ice reduce the resistance of the rock when it infiltrates fractures.

4. What are the appropriate safety factor equations to use in different situations? Different equations are used for different situations such as the planar and wedge landslides. These two geometries have significant differences in the equations which makes them unique so understanding what equation to use and when it is vital to this study.

5. What terms of the safety factor equations can be directly measured or reasonably estimated?

Each of these research questions will be developed through acquisition and interpretation of new data sets and addressed in the discussion section of this thesis.

CHAPTER 2: METHODS

2.1 Field Observations and Planar Measurements

Several different field methodologies were implemented in the research of the wedge landslide above Mt. Baldy Road along with the surrounding area, including the area along the Sierra Powerhouse Access Road which branches down from the main road. The data collection consisted of going to the field site and using a Brunton compass along with a handheld GPS unit to record where the data points were taken. Strikes and dips of foliations were taken with a Brunton with these measurements being recorded in a field notebook by either myself or another person if the area where the measurement was done is too precarious for safely recording the data. A Brunton was also be used in recording the slopes which are inaccessible from afar using other methods which allow for sighting from the ground and taking close, approximate measurements. Measurements taken on the various geologic features may be used plotted on a stereonet to determine the 3D structural geometry of an area; also for comparison to structures in the surrounding region. This should make it simpler to see if the area exhibits specific slope stability issues.

2.2 Photography

Observations in the area began in May 2018 when I started to go out to the site and continued to the final observations in January of 2020. Photographs were taken at there over time to compare if there were any significant changes in what happened and for later reference when looking at the field notes. Differences in the seasons over time would be noted for further analysis such as climate, more failures, etc.

2.3 Stereonet Analysis

One of the main analytical methods used in assessing the geology of the area is stereonet interpretation. Being able to plot on stereonets the different characteristics of the area including foliations, lineations, fractures or joints, rakes and other significant geologic features allows for direct comparisons. Visualizing how these structures correlate to one another and relate to the cut slopes is imperative in the pursuit of analyzing data so that a better understanding can be drawn from it. I used a program called Stereonet version 11.1.0 developed by Dr. Rick Allmendinger from Cornell University to plot my orientation measurements into multiple stereonet projections (Allmendinger, 2019). This program is useful in that it provides both 2D and 3D views of the stereonets which will be utilized to offer different perspectives of the surfaces being studied.

Stereonets are useful because they are extensively used in the process of understanding landslide mechanics as well as the types of failures which could occur (Hoek and Bray, 1981; Wyllie and Mah, 2004). While the failure involved that of a wedge failure in this area, there could be other types of failures such as toppling which could happen close to the failure such as seen in Fig. 6 (Agliardia, 2013).

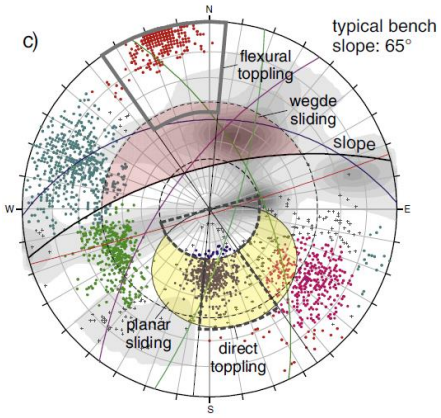

Figure 6: Stereonet from a quarry showing how different types of failures can be plotted on one stereonet (Agliardia, 2013.) Black line shows the typical bench slope of 65°. Colored lines represent different joints, fractures and structures most likely related to a strike slip fault in the site. Different colored and box areas represent different failure modes possible in those parts of the stereonet that are labeled.

A contour map which shows the areas of strongest correlation of measurements from this stereonet could be used to identify other potential failure areas. Information provided from this data analysis will give a better understanding as to what the 3-D geometry of a given slope is. Geometric features can help in determining certain parameters of the safety factor of different areas and can also be used to compare currently stable areas to see if there is a chance that they could potentially have activity in the future. A comprehensive risk assessment can be done as to assist with forward modeling of hazard zones. Figure 7 shows some preliminary research which shows the different interactions between the foliations and fractures within the rock that create a general wedge-type failure situation.

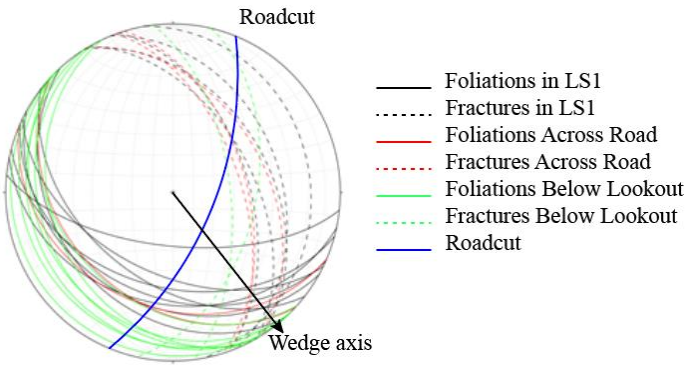

Figure 7: Example of early research done on LS1 in and around the wedge landslide. Black lines represent measurements in LS1, red across the road, green below the lookout. Solid lines are foliation planes, dashed are cracks. Later stereonets will have more complete data and different color codes.

2.4 High Resolution Topographic Surveying

A laser range finder (Fig. 8) was used in surveying the area to create a high-resolution topographic map with contour interval much less than the standard USGS CI of 40 ft (Appendix A). This is possible as the laser range finder will output an azimuth, horizontal distance and vertical distance for accurate measurements to within a tenth of a meter. A topographic map can also be created from this data which will be of high resolution, allowing to see and understand more of the features from the various landslides in greater detail than those provided by the USGS (e.g.s, Wicks, 2010). Maps can then be overlain on one another to spot difference for pre and post landslide events. Seeing how different features related to one another gives clarity on their interactions from a geologic perspective.

Figure 8: Me surveying the landslides with the yellow laser rangefinder.

Determining the volume of the landslide has been mostly done by one method which is to measure dimensions of the debris field and calculate its volume using some kind of geometric approximation (Agunwah, 2020). This was done in my study area by taking measurements to gather the dimensions of the area and applying the volume of a partial cone formula with a slanted backside in order to get a rough estimate of the total volume of landslide clasts plus voids. Afterwards, porosity estimates would be applied and back-calculated into the number to get a close estimate as to what the actual solid volume of the landslide block was before failure. In my study there will also be a secondary method applied which takes a different approach altogether by using the aforementioned laser range finder data to calculate a precise volume.

Position of Tripod	Easting	Northing	Error	Elevation	
(Determined from GPS)	437696	3785814	4	1043	
Notes	HD	VD	AZ	Easting	Northing
Bottom of Cone	14.3	-2.2	273.1	437681.7566	3785815.271
	14.4	-2.2	274.9	437681.7043	3785815.73
	15.2	-2.3	275.8	437680.9406	3785816.063
	15.2	-2.3	276.7	437680.9749	3785816.299
Going along top	15.4	-2.3	277.6	437680.8157	3785816.568
	15.1	-2.3	278.6	437681.1577	3785816.778
	15.9	-2.1	279.6	437680.4248	3785817.197
	16.5	-2.2	280.1	437679.8666	3785817.459
	17.5	-2.2	280.2	437678.8952	3785817.698
	16	-2	280.3	437680.3673	3785817.408
	16.5	-2	280.6	437679.8974	3785817.599

Figure 9: Sample of data compiled into excel. Negative VD values here due to pointing down relative to the height of where the laser rangefinder was positioned. Units in meters.

Data points taken from the laser rangefinder were compiled into an Excel document (Fig. 9) where the initial GPS coordinates of the location from which the measurements were taken are put in. Azimuth, horizontal and vertical distances were also input into the spreadsheet before using two different formulas to determine the easting and northing. The laser rangefinder was known to be a few degrees off as plotting uncorrected points caused for the data to not place correctly on the map, so a correction was also input into the excel formula. Easting = Easting of tripod + horizontal distance * COS((180-(Azimuth-270+2))*PI()/180) with Northing = Northing of tripod + horizontal distance * SIN((180-(Azimuth-270+2))*PI()/180) (Fig. 9). Once completed, the excel file was changed into a .csv file type in order to be able to import it into ArcGIS.

2.5 ArcGIS Manipulations

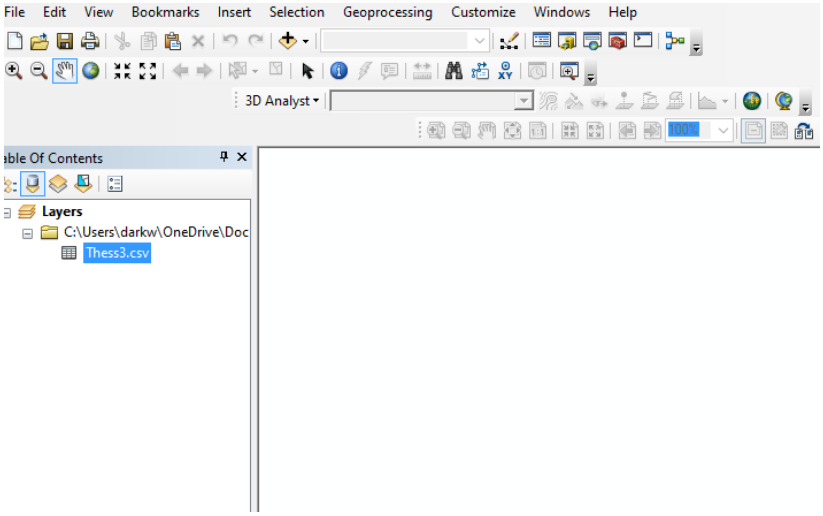

Figure 10: Where the file appears on the right-hand side.

Adding the data in with the add data option, there will now be the name of the file in the table of contents (Fig. 10).

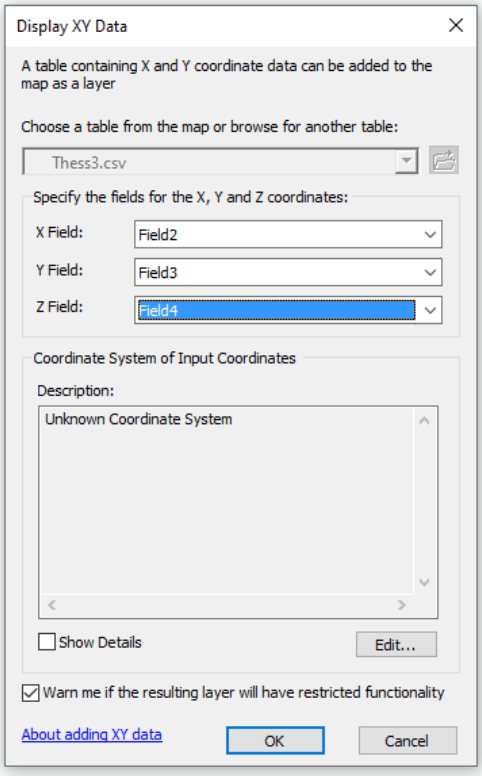

Figure 11: Selecting which data is for the three options.

Right clicking the added data allows for the display XY data to be clicked where the options to select which column is your X, Y and Z data (Fig. 11). Once this is done, one can isolate the points which form the outer edges of the landslide profile to give rough elevations at these points. Creating a second file in excel with the points along the edges of the landslide data allows for the outline of the landslide to be separate for future calculations and import that data in using the same method as before.

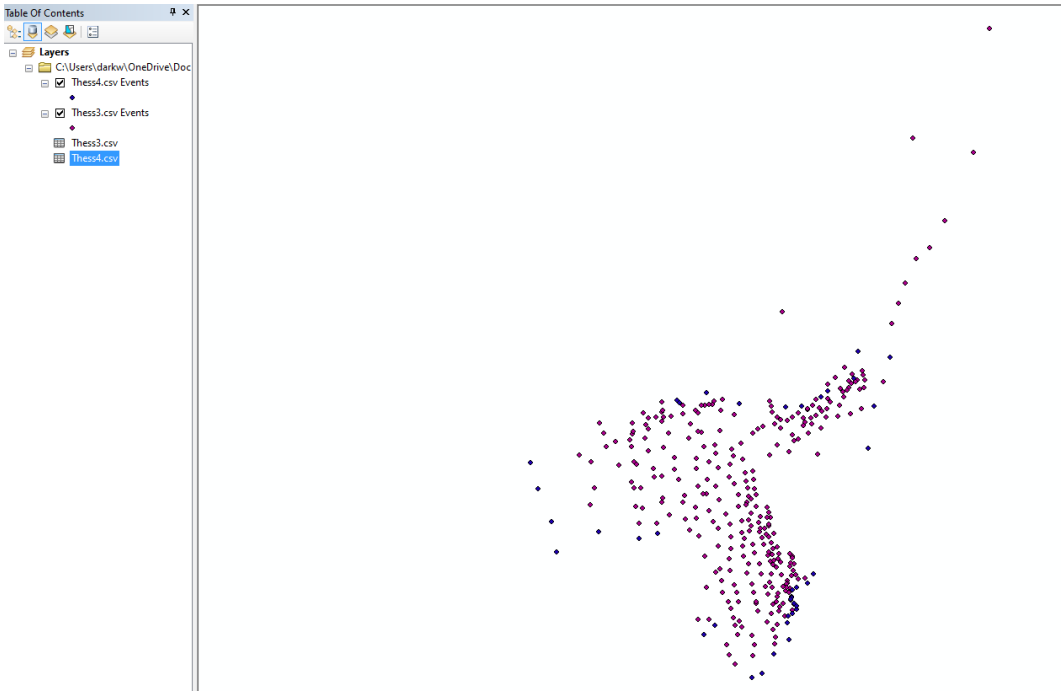

Figure 12: Table of contents and data plot after processes are completed.

This will create four items in the table of contents as well as sets of data that appear in the map area (Fig. 12).

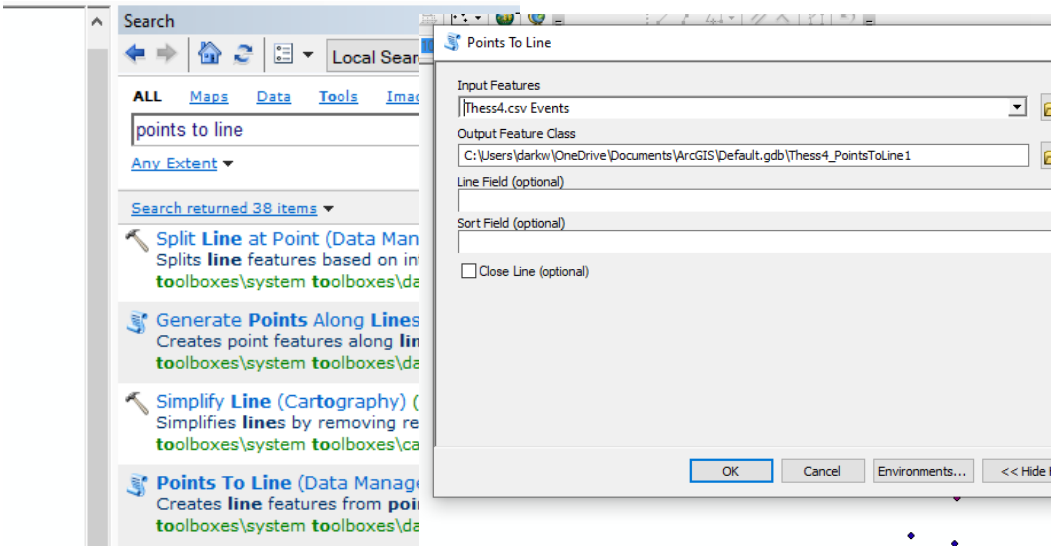

Figures 13 & 14: The menu to get the points to line feature and where to select the data from the dropdown menu.

On the exported data set for the outer edges of the landslide, I used the points to line feature (Figs 13 & 14) to create the face of the landslide and then selected OK. This kept all elevation data and created a "face" for the original surface prior to the landslide.

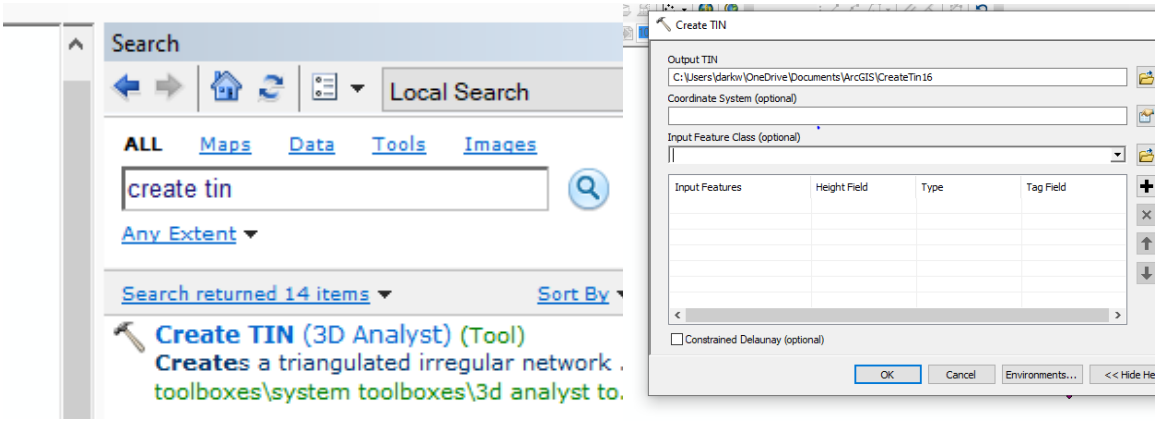

Figures 15 & 16: How to create a tin and how to select data under the input feature class.

I used the Create Tin feature on the side for both data sets (Figs. 15 &16). One will use the base data and the other will use the one from the points to line result. This created two

unique surfaces with one of being the current landslide area and one that is a rough projection of what the area was prior to the landslide.

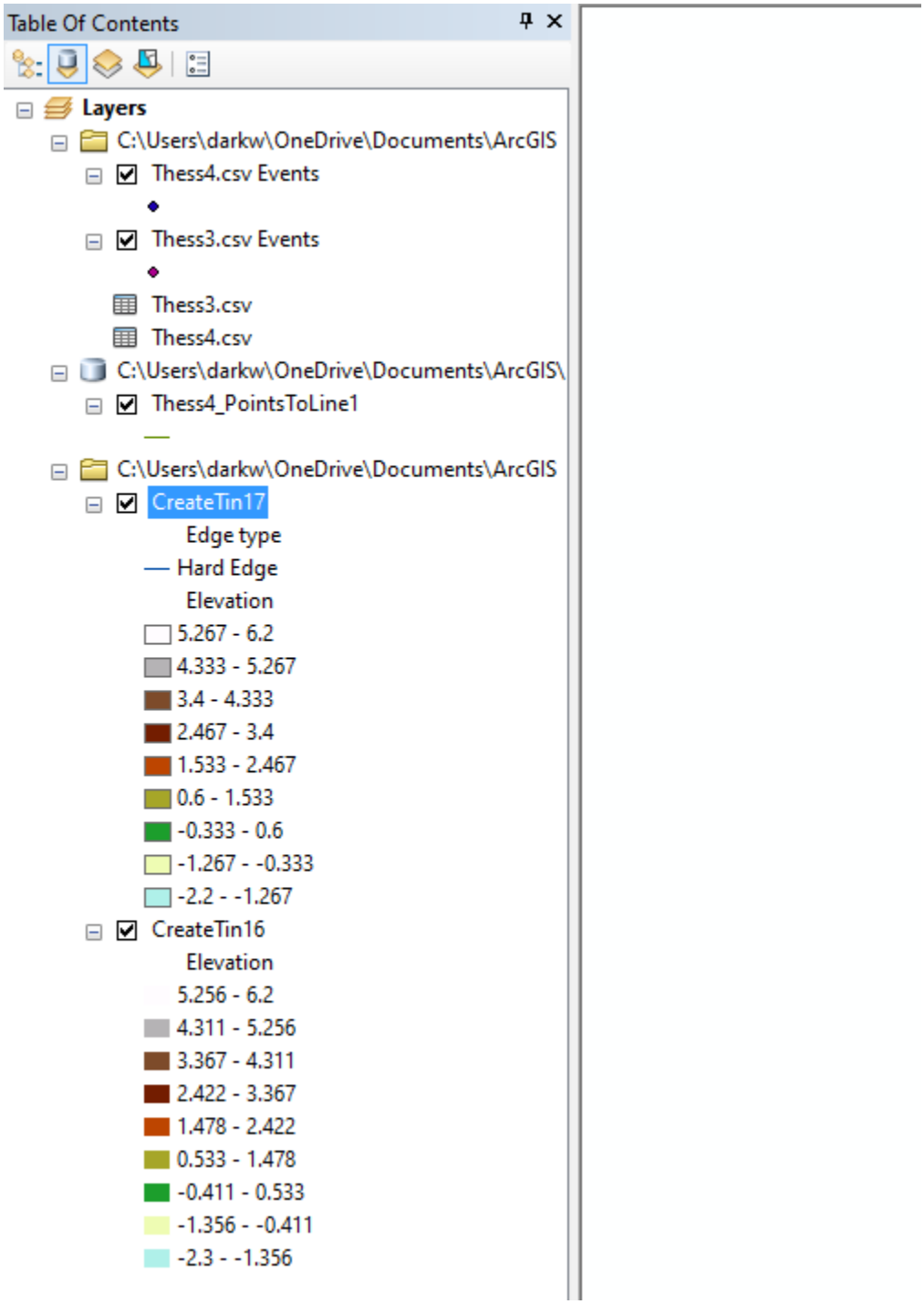

Figure 17: How the table of contents looks after all data is input properly.

I double checked that the two tins are from the current landslide surface and that of the exported line surface and also checked the table of contents to ensure that the data is all there (Fig. 17).

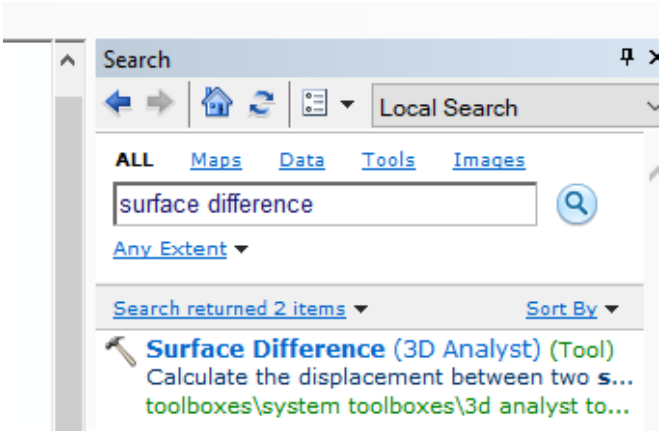

Figure 18: How to get the surface difference tool from the search menu.

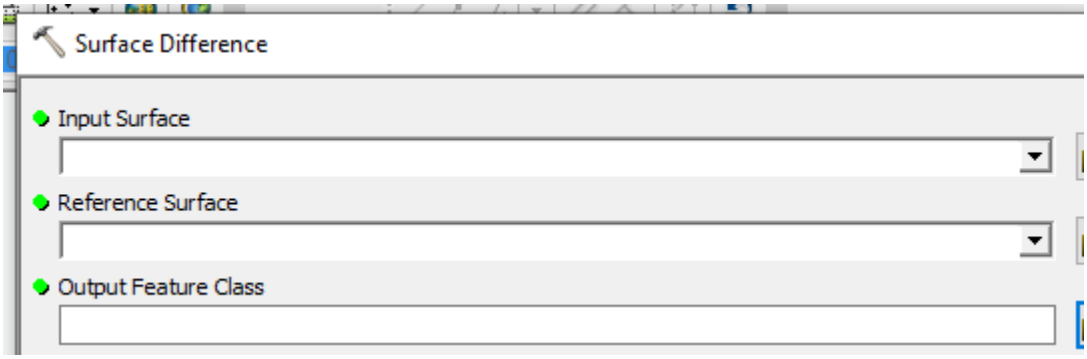

Figure 19: Menu for selecting the input surface and the reference surface.

I then used the Surface Difference tool to determine the differences between them. Note that one would want the input surface to be that of your current topography post landslide and the reference surface to be the inferred surface prior to the landslide event (Fig. 19).

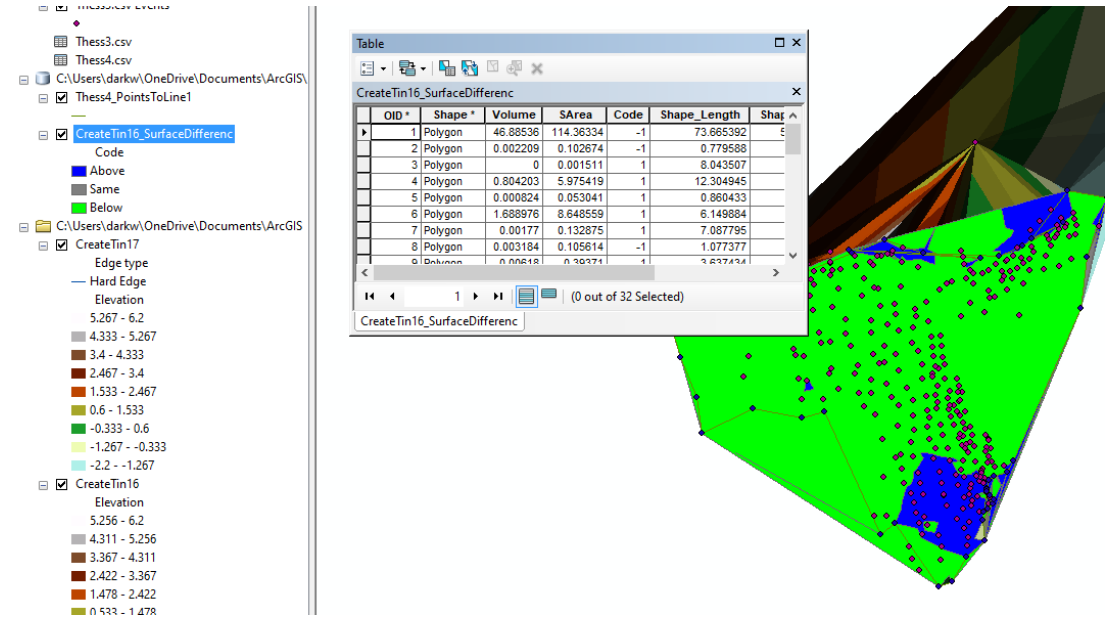

OID *	Shape *	Volume	SArea	Code	Shape_Length	Shap
1	Polygon	46.88536	114.36334	-1	73.665392	
2	Polygon	0.002209	0.102674	-1	0.779588	
3	Polygon	0	0.001511	1	8.043507	
4	Polygon	0.804203	5.975419	1	12.304945	
5	Polygon	0.000824	0.053041	1	0.860433	
6	Polygon	1.688976	8.648559	1	6.149884	
7	Polygon	0.00177	0.132875	1	7.087795	
8	Polygon	0.003184	0.105614	-1	1.077377	

Figure 20: Results of the calculations.

After all of this one would get the volume calculations which would be the differences in the empty space between the current surface and the hypothetical original face of the hillside. To see the table, I had to right click on the SurfaceDifference tin so I could see the results of all the volumes.

2.6 Kinematic Analysis Methods

Another method which is integral in the assessment of the area is using kinematic models with both theoretical (estimated) and quantifiable numbers (e.g., angles and dimensions measured in the field) to determine the various stability characteristics of a landslide (Raghuvanshi, 2017). This is where looking at the data collected in the field and plotted on a stereonet allows for certain parameters to be ascertained and geometric modeling to be done. Modeling also allows for ranges of different variables to be examined

that could influence the safety factor of the area (Fig. 21). Such factors include the cohesion, friction and the variable effects of gravity and water content on the driving forces.

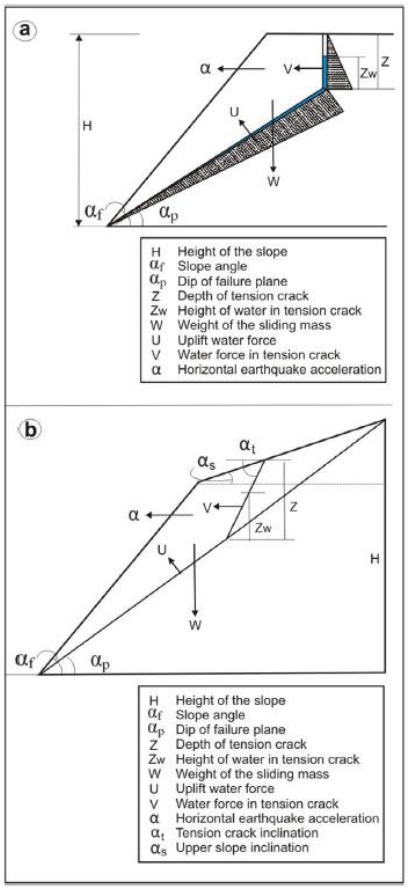

Figure 21: Key dimensions and different kinematic forces which act upon a landslide mass. It should be noted that a lot of these factors can change depending on the climate or other external factors (Raghuvanshi, 2017.) Things which influence driving stress such as the force of water, earthquake acceleration and the weight with respect to the slope are promoting failure while the weight in the downward direction, friction and cohesion are resisting failure.

Research done previously by Rogers, et. al. (1992) has estimated different phi (angles of friction) values for a variety of the expected surfaces in this area. There are three types of fracture surfaces that are found extensively in this area that might have different phi values. These values are: 40° for rock to rock contact with slightly undulatory joints and no mineralogic infillings, 30° for rock to rock contact with smooth, planar joints and no mineralogic infillings and 25° for discontinuities with slickensided epidote infillings (Rogers et al., 1992). Clay gouge caused by chemical weathering is also an important factor

which would reduce the phi value. These were directly measured in studies cited in Wyllie and Mah (2004) so it would be assumed to possibly reduce it to 15 degrees or even 7 degrees. Another important factor besides the phi value would be the influence of water on the behavior of tension cracks as. In the San Gabriel Mountains, there will be seasonal variations because of changes in climate. Water is usually not as present during the dryer months as well as in years that are within the drought parameters yet there are years with abnormally high amounts of precipitation. This would drastically alter both the cohesion and friction values within the given parameters above that could push the safety factor to be much lower than normal. Cohesion is the final important variable which is looked at which is the shear strength of the rock under zero normal stress. This factor is effectively the bonding strength between mineral grains that is generally very high in rocks (20,000-500,000 lbs/ft^2) but can be greatly reduced by fracturing or presence of clay in fractures.

The chart in Fig. 22 looks at how blocky and massive a rock which could also give a sense of how unstable the area could be. Different types of rocks could be more or less susceptible to failing depending on how blocky the rocks are. In a paper by Hoek, 2000, he showed how a chart could be formed to show the decrease in surface quality which affects the friction angle and the interlocking component of rock pieces that is another description for cohesion (Fig. 22). Assessing these conditions could give a better insight as to how accurate calculations will be. Measurements of the internal part of the landslide will be used to create a diagram of the landslide to calculate the rough amount of material which was moved in the event. This will aid in the calculation of a safety factor for the granitic gneiss in the area. Angles of friction are used from different papers that have calculated the angle of which the driving stress overcomes the natural friction of the rock. The friction

will be used since this area has already shown many previous failures which would make the rock much weaker.

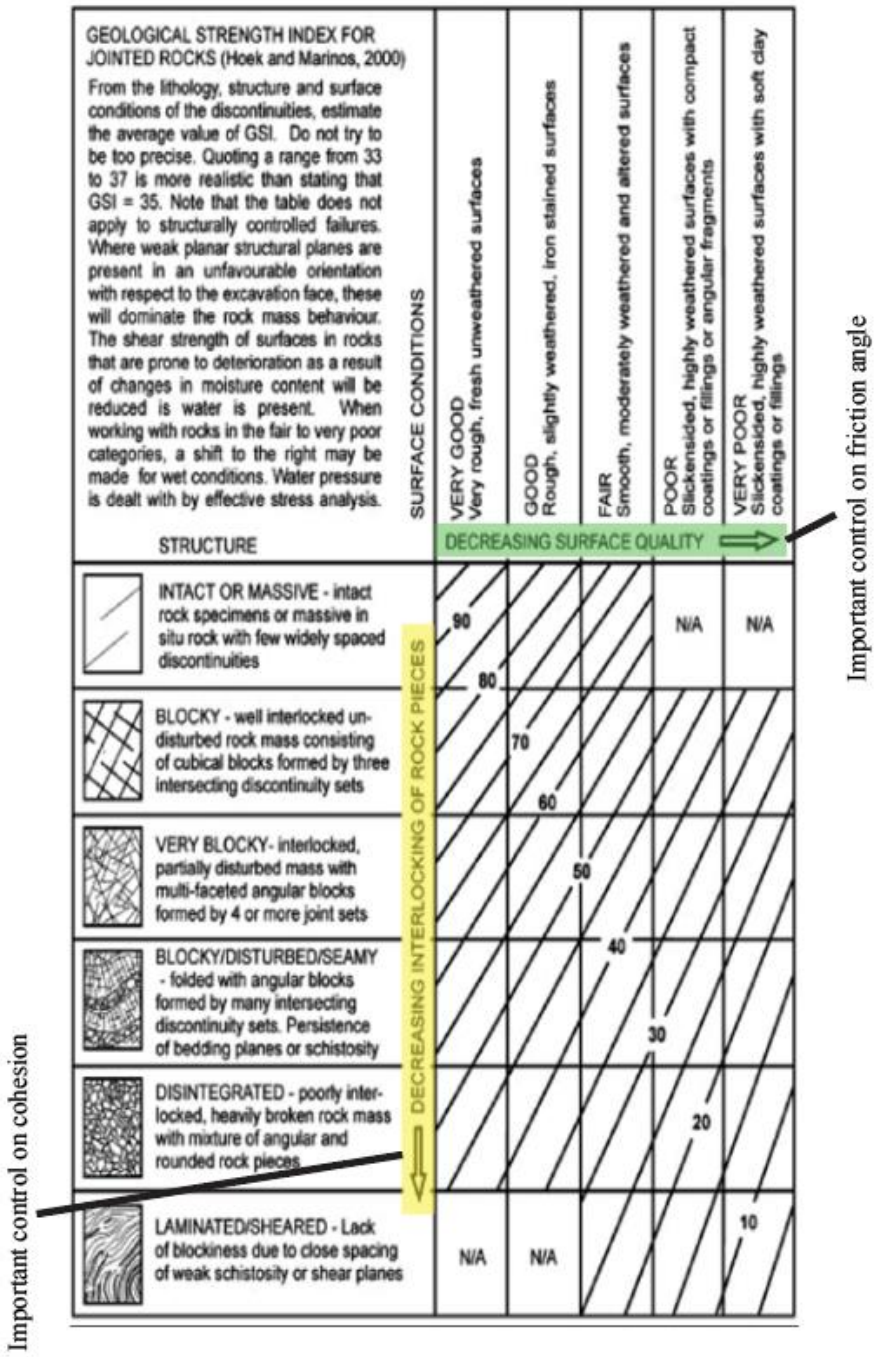

Figure 22: A diagram showing how both the blockiness as well as surface quality influence the strength of jointed rocks which will be useful in assessing the area (Hoek and Marinos, 2000).

2.7 Safety Factor Analysis

Safety factor calculations were done independently for different features and areas of the study area. The basic premise of the safety factor is the calculation of the resisting shear strength over the driving shear stress. It is the balance of these two numbers which determines whether or not a slope is stable. In other words, failure occurs when $SF = \frac{Resisting\ Stress}{Driving\ Stress} \leq 1$. Most of the formulas used to calculate this number are given within other studies. I used the approach of Wyllie and Mah (2004) that follows the pioneering work of Hoek and Bray (1981).

$$SF = \frac{Resisting\ Stress}{Driving\ Stress} = \frac{C + tan\Phi[\frac{(Weight)cos\theta}{Area}]}{\frac{(Weight)sin\theta}{Area}}$$ The formula is for the use within translational landslides in dry cases is given below and a more complicated SF equation includes terms for P_{H2O} acting upward along the base and also at the rear of the slide mass.

$$SF = \frac{Resisting\ Stress}{Driving\ Stress} = \frac{C + tan\Phi[\frac{(W)cos\theta - F_{H2O}\sin(50)}{A} - average\ P_{H2O}Up]}{\frac{(W)sin\theta + F_{H2O}\cos(50)}{A}}$$ is used for wet conditions. Fig. 23 shows the applicable stresses.

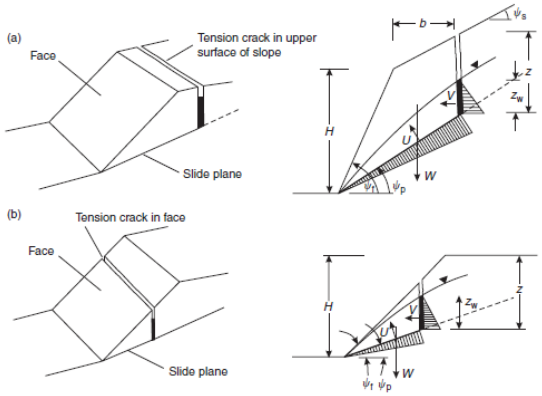

Figure 23: Diagrams showing how a planar landslide occurs and things measured (Wyllie and Mah, 2004).

There is a different formula used by Wyllie and Mah to calculate the safety factor of a wedge landslide which is: $FS = \frac{(R_A + R_B)tan\Phi}{Wsin\psi_i}$ with $R_A + R_B = \frac{W * cos\psi_i * sin\beta}{sin\frac{1}{2}\xi}$ This

simplifies to $FS = \frac{sin\beta}{\sin(\frac{\xi}{2})} * \frac{tan\Phi}{tan\psi_i}$ if it is used, assumed a slide caused only by friction with no cohesion. In this case the weight term cancels out. Fig. 24 shows the geometric parameters. R_A and R_B relate to the two sides of the landslide with W equal to the weight of the slide. ψ is the angle of the slide plane and phi is the potential angle of friction. A different formula is used under conditions to find cohesion and angles of friction for failure (Hoek, 1981). Derivation of this equation is show in Wyllie and Mah pgs. 157-160.

$$F = \frac{3c_A}{\gamma H} \cdot X + \frac{3c_B}{\gamma H} \cdot Y + \left(A - \frac{\gamma_w}{2\gamma} \cdot X\right) Tan\phi_A + \left(B - \frac{\gamma_w}{2\gamma} \cdot Y\right) Tan\phi_B$$

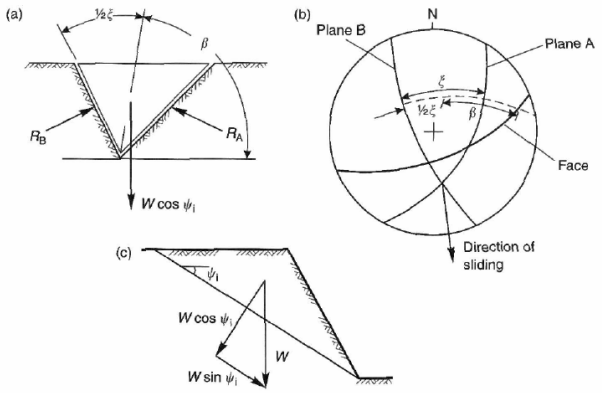

Figure 24: Parameters for a friction only wedge landslide (Wyllie and Mah, 2004).

What makes a slope unstable would be if the FS is a number less than or equal to one meaning that the driving shear stress has overcome the resisting shear strength so that the slope would be able to fail. If this number is greater than one, than the slope would be safe and stable. However, this formula can be modified to take into account more factors than the base equation which is seen within the model from Figure 25 alongside the stereonet from Figure 26 and the formula below.

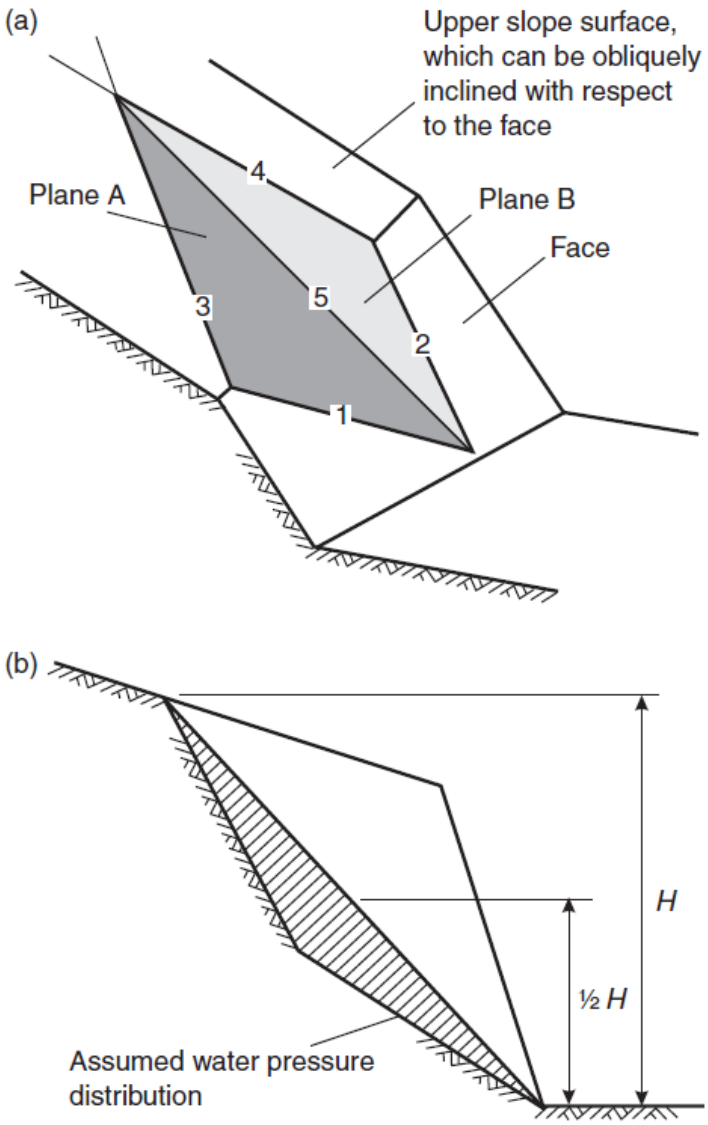

Figure 25: Diagrams showing the parameters that will be shown on a stereonet and also where to measure the height along with where water pressure distribution is thought to be in a wedge (Wyllie and Mah, 2004).

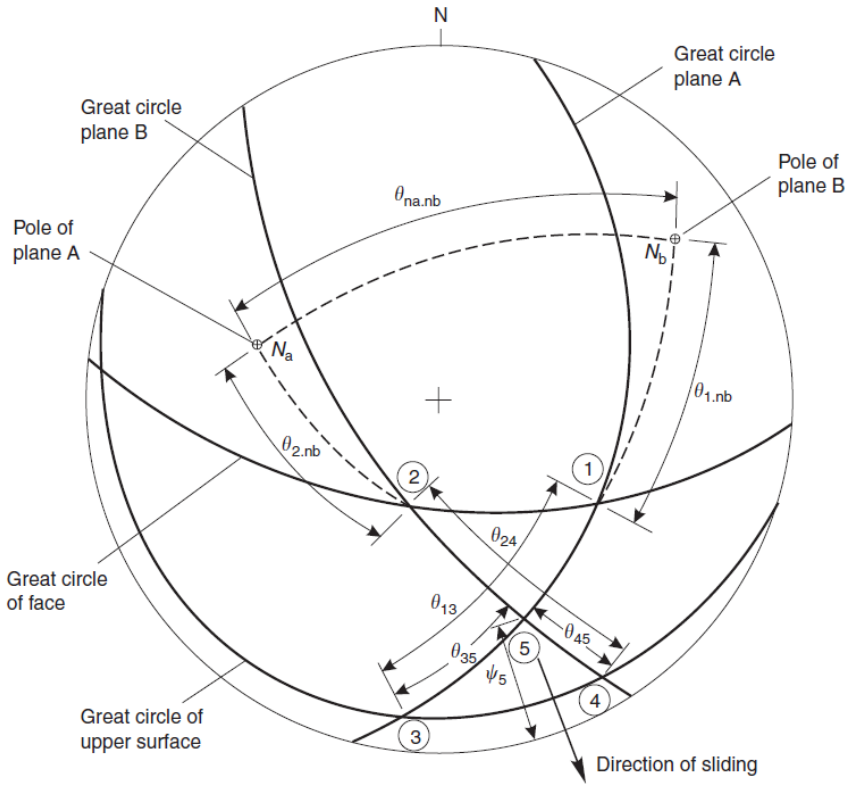

Figure 26: Stereonet diagram showing some of the parameters in the complex failure safety factor equation for a wedge situation. It is complex in that it goes into an increase in parameters which are taken into account. Great circle of the upper surface is the top of the original surface prior to failure. More details given in the safety factor section of the document (Wyllie and Mah, 2004).

CHAPTER 3: RESULTS

Observations made at the field site are noted in this section. Three subareas studied in detail are highlighted on Fig. 27a representing LS1 wedge landslide, LS2 wedge landslide and LS3 planar landslide. Many photographs and data were taken along both Mt. Baldy Road as well as the fire escape road which leads down towards the San Antonio creek which has been influenced in its path by the Hog Back landslide which is roughly a quarter mile north of the main field site. Figures 27b and 27c are maps showing the areas of the laser rangefinder data, volume calculations and strike and dip data taken with a Brunton Compass compiled together by location. Stereonets used to help determine the angular parameters for landslides are described below.

Figure 27a: Map showing the different areas of where measurements were taken. Image sourced from google earth.

Figure 27b: Zoom in showing the southern research area with focus sites and locations corresponding to later figures.

Figure 27c: Northern research area showing locations of photos and stereonet compilations.

3.1 Chronology of Field Observations

The first time I went to the field area was back in 2018 during the month of May to begin observing the potential for it becoming a study site. Much of the time was spent hiking around both on Mt. Baldy Road as well as going down the fire access road to see the various rock formations as well as get a general characterization for the area (Fig. 27). The first true time which was spent taking measurements was on July fourth of the same year where observations were mostly focused on the wedge landslide (LS1) as well as the parts on either side of the landslide. No pictures were taken during this first time as I had gone by myself and was having to take many of the measurements in various locations in a safe manner. However, I was provided a photo by Dr. Nourse from 2017 before the rubble was cleared for the first time (Fig. 28). Observed were the differences in the types of rock on one side of the wedge failure plane in comparison to the other with the North side being comprised predominantly of gneiss with the southern plane having abundant quartz diorite intruded by basalt. Photographs included with the site descriptions below are located on index maps of Figs. 27b and 27c.

Figure 28: Wedge landslide photo from Feb. 8, 2017 taken by Dr. Nourse.

The second trip to the field site for thorough measurements occurred on July 20th of 2018 with my mother now accompanying me to make things a bit easier when it came to taking measurements in more awkward positions so that I could call them out with her recording them. Observations were taken along various parts of LS1 within the landslide failure surface noting parts with more felsic gneiss being on the north and basalt intruded granodiorites being on the south. Fractures were noted to be mostly orientated in the NW-SE direction with dips towards the NE and foliations with accompanying fractures to the SW. Some of these fractures though were orientated parallel to the basalt intrusions seen before (Fig. 29).

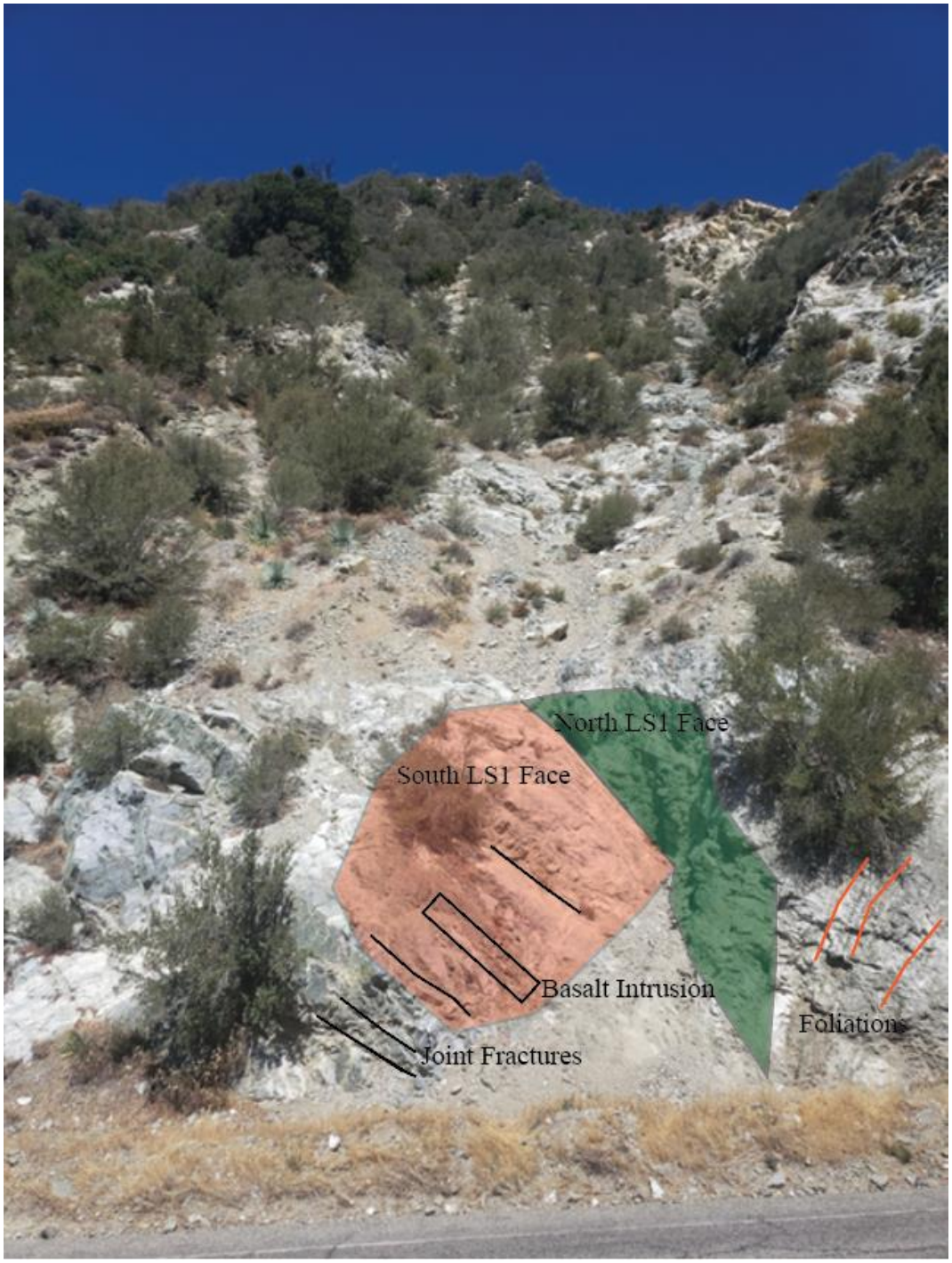

Figure 29: Image taken on July 20th, 2018 of the wedge after having surface cleared.

Another trip to the field site on the Sept. 3, 2018, proved to be more difficult as the temperature was higher than many other days and was found to be almost intolerable. This was a day where only photos were taken to show the different sizes of fractures in the area

below Mt. Baldy Road along the Sierra Powerhouse Access Road (Fig. 30). There were some features that could potentially have been miniature wedge landslides with their shape. Measurements were taken to confirm this later with stereonet analysis.

Figure 30: Measurements being taken below the lookout above the Sierra Powerhouse access road.

Trip number four, on January 19, 2019, to the landslide occurred after a series of winter storms that let loose more debris from the top of the hill and formed little areas of debris along various parts of the roads. Fortunately, it also created a scenario where a debris

cone (Figs. 31, 33) had formed along the bottom of the wedge landslide LS1 that would allow for me to go up higher up in the landslide and get measurements nearer to the top of it which was about twelve meters above the base ground level. Recent rain events had also better exposed epidote patches along the southern side of the landslide to be able to get ten measurements of strike, dip and rake which suggests the past presence of a fault that cut through this portion of the landslide. Due to how unclear these rake striations were, determining the direction that the fault moved was not possible to do. LS2 was observed to the north of LS1 and seemed to have a similar wedge geometry. This area failed in the past and has similar fractures to those of LS1. We took one brief detour under the lookout to measure a fracture (Fig. 32). Temperature began to drop quickly as the sun went over the ridge which forced my mom and me to call it a day and head back home.

Figure 31: View looking south to the debris cone after winter storms from above wedge LS1 taken on 1/19/19.

Figure 32: Fracture about 1.5 inches wide under the lookout.

Figure 33: Hiking on the cone after a storm in the wedge. (LS1)

LS3 was first photographed by Dr. Nourse so I did not have any field excursions yet to the site, but it is important to discuss it here. The LS3 area showed a different type of geometry which was unique to this part north of the parking area (Fig 27c). Instead of

the intersecting fractures which caused for the wedge failures observed to the south, this area had only one plane of failure that was seen (Fig 34). Daylighting surfaces caused for these failures to happen without the necessity of another set of fractures or joints aside from the fractures which occurred along the foliation planes (Fig 35).

Figures 34 and 35: Photos showing the failed landslide surfaces taken on February 11, 2019, by Dr. Nourse.

During the fifth excursion on April 3 out to the field site, I went out to the area with Emmons McKinney to go below Mt. Baldy Road along the fire road and even beyond it. Some of the features here had proven to be difficult for my mother to hike to so Emmons (Fig. 36) and I went exploring in the brush. Some of the features we saw here seemed to suggest the presence of old wedge landslides that now were disguised as other features such as a small waterfall (Fig. 37) which was still active after some of the relatively recent rains. Measurements were taken using methods learned from Dr. Van Buer during some of the other trips we had been on for field assignments to sight from a distance which helped greatly in getting good approximations for strike and dip to be used later on in a stereonet to see if these conditions were right for a failure or if this was natural erosion. This potential

Figure 36: Emmons in the San Antonio Creek after taking measurements down the Sierra Powerhouse Access Road.

Figure 37: Potential mini wedge with small waterfall above the Sierra Powerhouse Access Road.

wedge seemed to be composed of heavily weathered gneiss which was strongly foliated since it could even be seen from about 20 meters away with some confirmation coming from the talus which comprised the parts down in the creek. Much of the other parts in this part of the field site were overgrown and covered with loose soils/talus making many parts inaccessible.

Trip number six on July 30th involved me going to do some research around the area of the parking lot north of the original landslide (LS1) location (Fig. 38) listed as above parking in Fig. 27c. Right away, it was apparent that the walls on the southern side of the parking area was mostly the gneiss that comprises much of the field area north of LS1 showing a clear division between the two parts. Foliation dips were consistently to the southwest which was the same dip direction as that observed on earlier trips to the landslide. Looking around revealed a path to get up higher onto the area which yielded many measurements which otherwise would not have been taken. Much of the gneiss had a brownish tinge to it from extensive weathering (Fig. 39) from weathering of biotite. This helps to distinguish the felsic gneiss from green diorite from quartz diorite unit which contains hornblende and epidote. Up high the dips were also consistent with all the other measurements that characterized the area. One of the other features seemed to be a little wedge like feature that happened along one of the fractures that ran through the rocks as there was a plethora of such fractures in the more heavily worn area. Twenty-four measurements were taken with waypoints attached to them via GPS later cross referenced with maps to ensure they were all in the proper spots.

Figures 38 and 39: Figure 38 (left) shows the area by the parking area where measurements were taken while Figure 39 (right) shows the weathered condition of the felsic gneiss up high.

A seventh trip on August 1st to the area was to confirm some of the measurements along the southern part of LS1 as well as the area further down the road from the wedge. I was able to climb back into the landslide and get a nice picture of the epidote which had striations (Fig. 40). Measurements were noted to have been taken on either foliation, fractures, or epidote surfaces. One clearly defined fault with obvious offset was also measured at the last part of the day.

Figure 40: Striated epidote fault surface on south face of LS1 better exposed in light.

Trip number eight on August 6th to the area weas spent taking many measurements along the fire access road and beneath the lookout point of Mt. Baldy Road. There were possible indications of small-scale failure events due to the orientations of the foliations and fractures within both the gneiss (Fig. 41) and the quartz diorite. Gneiss was predominantly found in the more northern parts of the fire escape road with the occasional parts of granodiorite and other mixed rocks being found nearer to the branch off from Mt. Baldy Road above. One large fault was spotted closer to the top which seemed to have that same distinctive wedge-shaped pattern with one plane being much steeper than another with opposite dip and would later be plotted onto a stereonet. Further down, a large fracture interacted and intersected with foliation in different angles which seemed to be conducive towards the movements of blocks that were roughly three to four feet in length and about

one foot tall. Some of these blocks had been in place on earlier trips but had now dropped down leaving gaps that were approximately 3-4 inches above the fallen boulder. Other pieces which were closer to cobble size also seemed to have shifted between trips and more readily pronounced the various fractures which crisscrossed the entirety of the part beneath the observation area which was above on the eastern side of Mt. Baldy Road. More observations along with 35 measurements containing associated waypoints were done on this day though more measurements would be needed because there were additional features to be notated by my mom (Fig. 42).

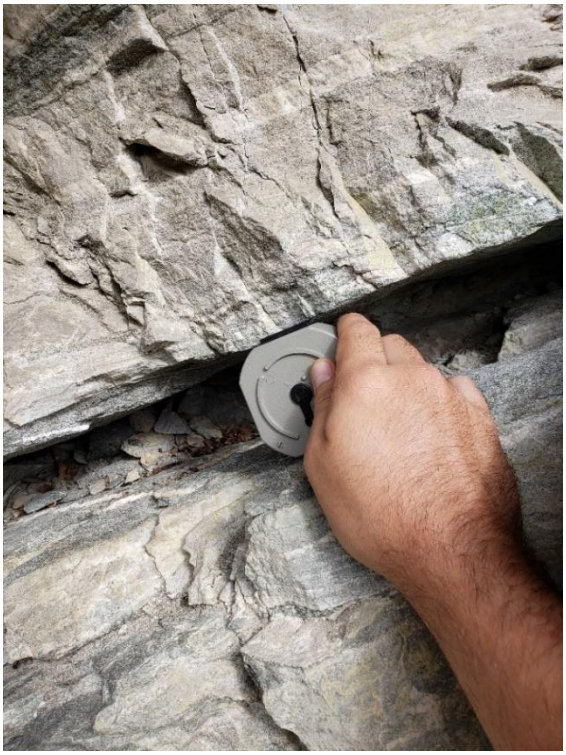

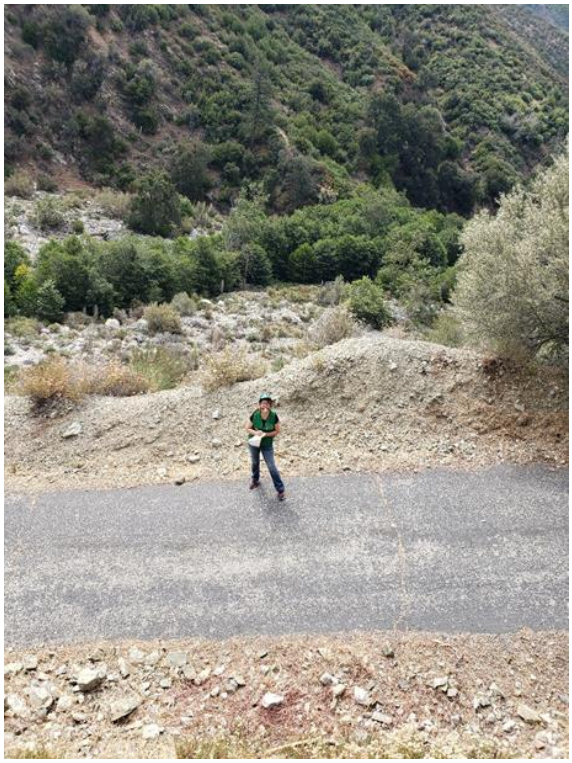

Figures 41 and 42: Figure 41 (left) shows the size of a fracture along the foliation plane in the felsic gneiss by the Sierra Powerhouse Access Road with Figure 42 (right) showing my mom taking notes from measurements.

Trip nine on August 8th to the field site involved an overview of the entire area both above and below Mt. Baldy Road with more of the focus looking more into some of the patterns observed on the previous day which had not been fully explored. One of the more important observations was the water stain around a crack in the rocks which was offset by

a fault (Fig 43). Seeing the evidence of water having been built up enough over time to leech through a small crack slowly so that it would stain brought into focus that there would be a need to determine the safety factor both with the presence and lack of water. This is not surprising since the climate during the winter is generally more wet as seen throughout historical records on weather stations that are around the area, characterized by some years of more wet weather with others that are drier. Water which penetrates these fractures throughout the winter are also prone to freezing which expands the water causing for expansion of the cracks, inducing failures of these surfaces over time. Twenty-eight measurements were taken with fifteen waypoints recorded.

Figure 43: Strongly foliated gneiss underneath the lookout by the fire escape road.

Trip ten, on October 30th, was taken with Dr. Nourse up to the area to look at the whole area along with discussing the specifics of certain areas. These measurements were exclusively taken by Dr. Nourse save for a few which were closer to the ground surface where I could reach them. Among these observations would be the secondary slide that was upslope from the main slide about 15m which was smaller in nature than the main one but similar in fracture geometry suggesting wedge failure. We also took measurements of a fault gauge zone (Fig. 44) that was observed here which was previously not recorded in my notes which was near the secondary slide. Many of the measurements taken at the primary slide were daylighting in nature in relation to the orientation of the road cut which was there previously before the failure. A large breccia zone was in the center of the landslide along the axis which confirmed the previous fault that was suggested by the presence from the epidote striations observed on other trips. We then went north of the parking area to investigate a third landslide (LS3). No notes were taken at LS3 on previous trips so this was an area time was spent on (Fig. 45). Dr. Nourse and I were able to identify a plane failure geometry upslope from where we stood with Dr. Nourse going onto the slope surface to take measurements on it. Foliations were measured as well for comparison to those taken south of this landslide to see if there was a change in how the foliation dips across the totality of the site.

Figure 44: Dr. Nourse measuring a brecciated fault near LS2 on October 30th.

Figure 45: Image of LS3 which is north of the parking area on October 30th, 2019.

3.2 Stereonet Results

Stereonets summarize much of the results of my structural measurements to later be applied in safety factor calculations. Knowing the orientations of the unique features along the various parts of the road would be able to show whether or not certain surfaces are going into slope or are daylighting instead. Daylighting planes are typically the ones with the highest risk for plane failure but not all of the data sets will necessarily reflect such landslide risk because of their into slope nature. However, much of the study area displays two sets of intersecting fractures that create an unstable wedge geometry. Stereonets correspond to locations listed on Fig. 27b and Fig. 27c.

3.2.1 Area South of Parking Lot

Traversing up the southern portion of the parking lot revealed many of the fractures and foliations which would be dealt with throughout the entirety of the field area. More of the contours for poles would be in the northwest quadrant with some being in the two southern quadrants. Figure 46 highlights with bullseyes fractures formed in those parts of the stereonet. This area only contained the felsic gneiss with the occasional quartz intrusions though none of the latter were in areas that could be measured accurately due to the steep nature of the slopes. Fig. 46 shows the major fracture orientations which were observed in the area above the parking lot with there being three distinct orientations for them. Fig. 47 shows the three-dimensional view of the average poles and planes from the stereonet.

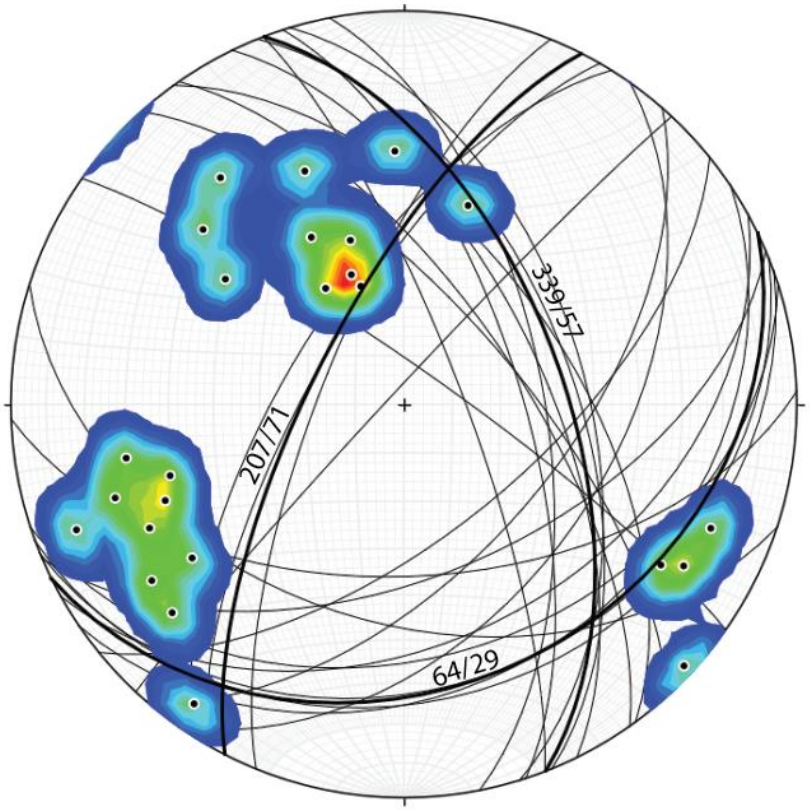

Figure 46: Stereonet showing fractures above the parking lot. Bullseyes represent clusters of poles from these fracture planes.

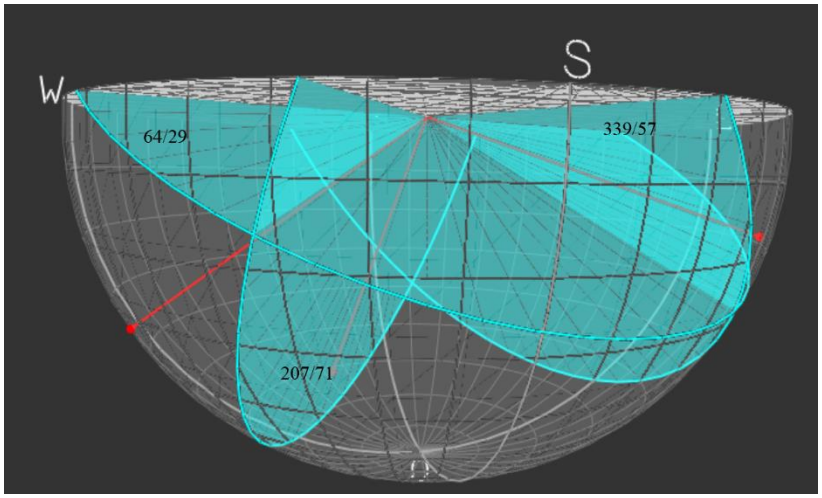

Figure 47: 3D view of the stereonet data.

3.2.2 Wedge Landslide (LS1)

The stereonet of Fig. 48 shows fracture orientations at landslide (LS1) that comprise of the wedge surfaces observed. A multitude of measurements were able to be taken on the southern surface that was dipping to the northeast as it was a larger overall surface area and was overall easier to get access. Looking at the original stereonet without poles or contours plotted reveals the overall tendencies of both of the faces of the surfaces. On the southern side, there is an overall dip to the northeast varying in dip from 19 to 64 degrees and strikes from 300 to 17 degrees. Most of the strikes ranged from 330 to 355 degrees with dips between 33 and 59 degrees. On the northern face of the wedge dips in the foliation of the felsic gneiss were 34 to 78 degrees southwest with the steeper dips on the lower parts closer to the wedge axis. Strikes on this part ranged from 95 to 170 degrees with majority being between 114 and 138 degrees. Contours of the poles from the surfaces show a tighter cluster for the measurements on the southern slope versus those of the northern slope. The stereonet contains the poles to show the contours for these measurements along with the roadcut in green which is orientated N20E with a 70SE dip. Average slopes of the two planes were calculated leading to an intersection which would be the wedge axis. The best fit trend and plunge for this axis was 142/25 to be used in the safety factor section. Figure 49 shows the 3D intersection of these best fit planes and the wedge axis that forms.

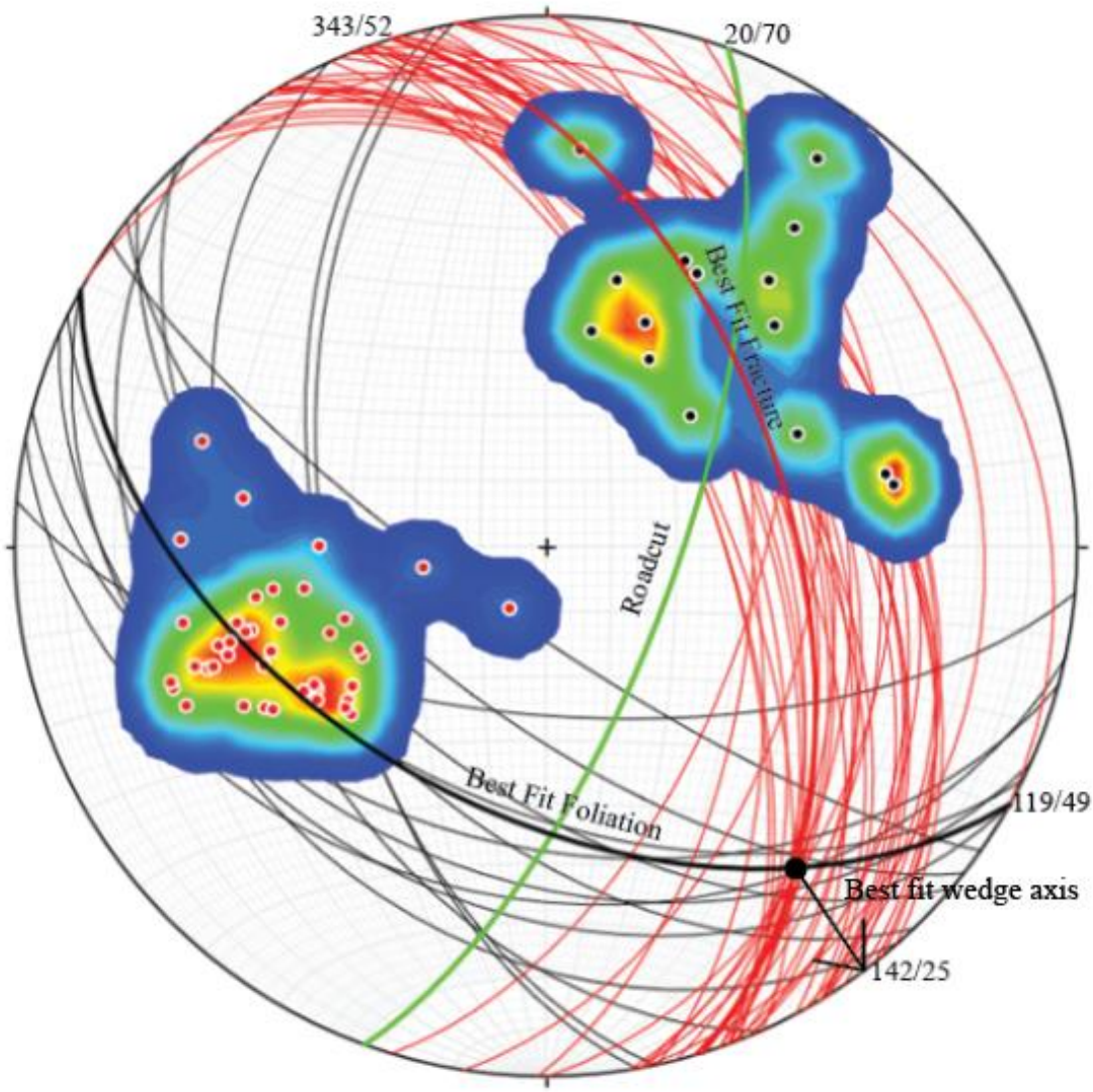

Figure 48: Black lines showing strike and dip on the north face of the wedge (LS1) with red being the south. Parallel fractures follow closely to the red which suggests a fracture pattern in the area. Average strike and dip of the north face is 119/49 while for the south was 343/52, both shown in bold lines. Green line is the roadcut.

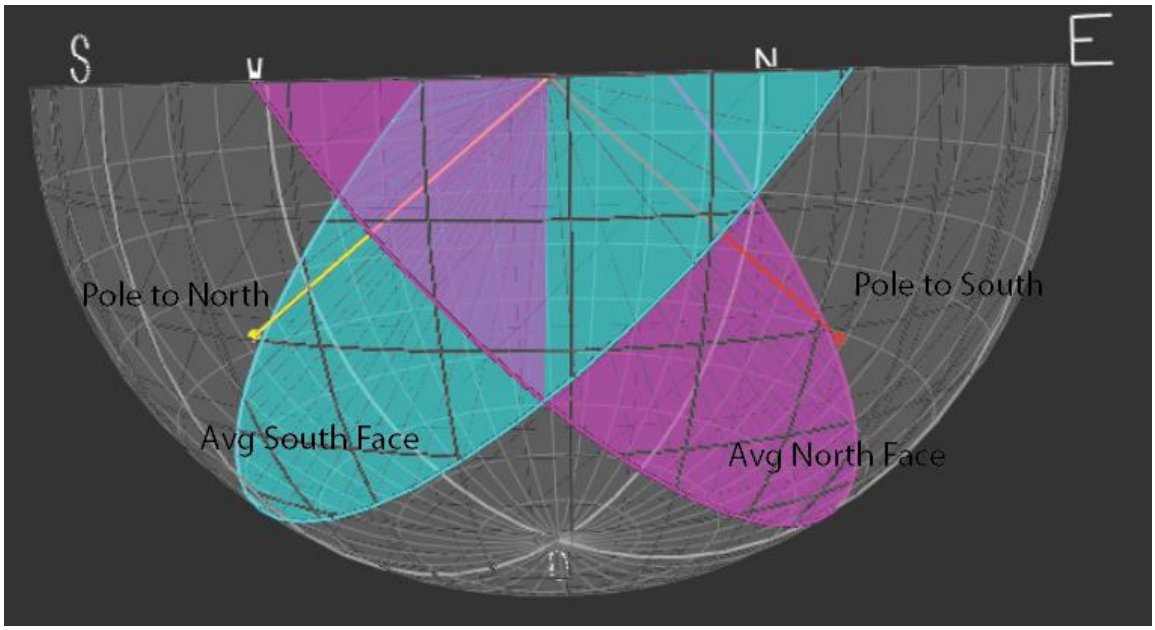

Figure 49: 3D view of the intersections between the planes of the two faces.

3.2.3 Potential Wedges North of Sierra Powerhouse Access Road

Hiking to an area (Fig. 27c) that was loose with talus revealed a few more potential wedge failures that had occurred in the past (Figs. 50 & 51). Both of these were sighted from afar using techniques learned from Dr. Van Buer with a Brunton since the surfaces were inaccessible. Greater than 25 degrees of plunge was observed in both cases with the one on the right having a plunge of 26 and the other having a plunge of 49 degrees. Based on the one set of measurements which could be observed in both of these cases, it is plausible that they experienced a wedge like failure at some time in the past though no true calculations of the volumes of these slides could be down due to the transportation of talus from above. Wedge geometry was observed as two different planes intersected at a point that daylights out of the cut slope. Surfaces were observed to have epidote. As we will see later, plunges above 25 degrees were at risk of having failure with the case of the plunge of 49 degrees prone to failure even under the most optimum conditions were angle of internal friction would be 40 degrees.

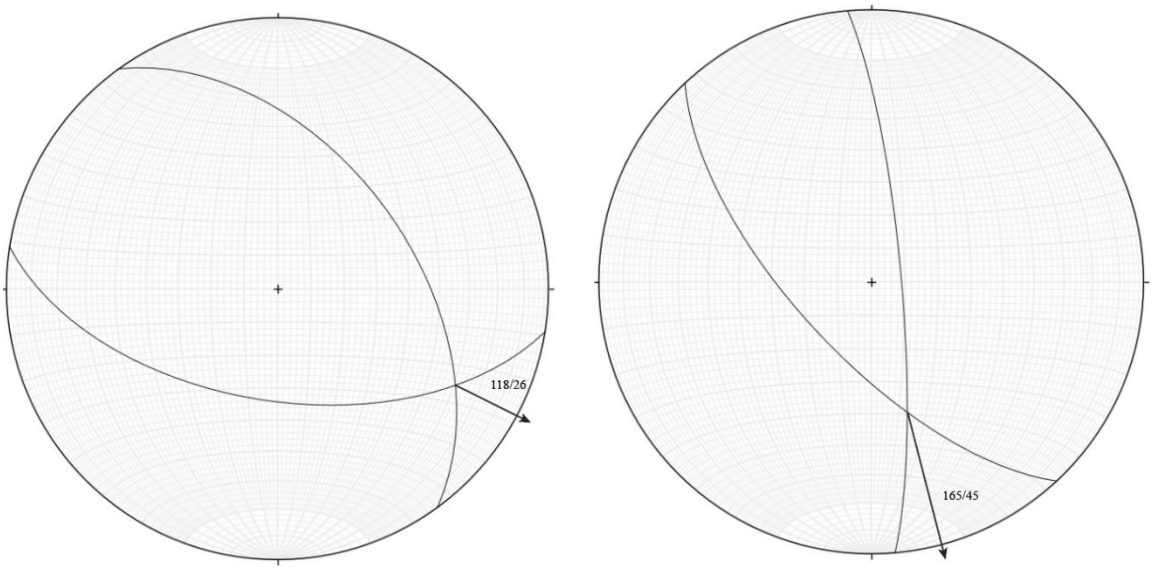

Figures 50 & 51: Showing two potential small wedges north of the Sierra Powerhouse Access Road which were sighted from afar.

3.2.4 Area South of LS1

The area south of the wedge landslide LS1 contains a mix of different rock types that preserve some different fracture orientations (Fig. 27b). Foliations are relatively similar to those from the wedge landslide further north on this stretch of Mt. Baldy Road. One of the major observation differences between the two are the orientations of the fractures which form joints at various places throughout the quartz diorite and felsic gneiss (Fig. 52). Road orientation (N5E-N20E) in comparison to these measurements suggest some daylighting does happen but at areas where there is little to no epidote along with more solid structure would lead to the conclusion that these areas are at a lower risk for failure but do fall under the greater than 40 degrees required to have failures in the future. Some fracture surfaces intersect to the east at areas within the friction circle, so wedge failures are possible along steep plunging axes. Intersections to the southeast are shallow so failure is unlikely.

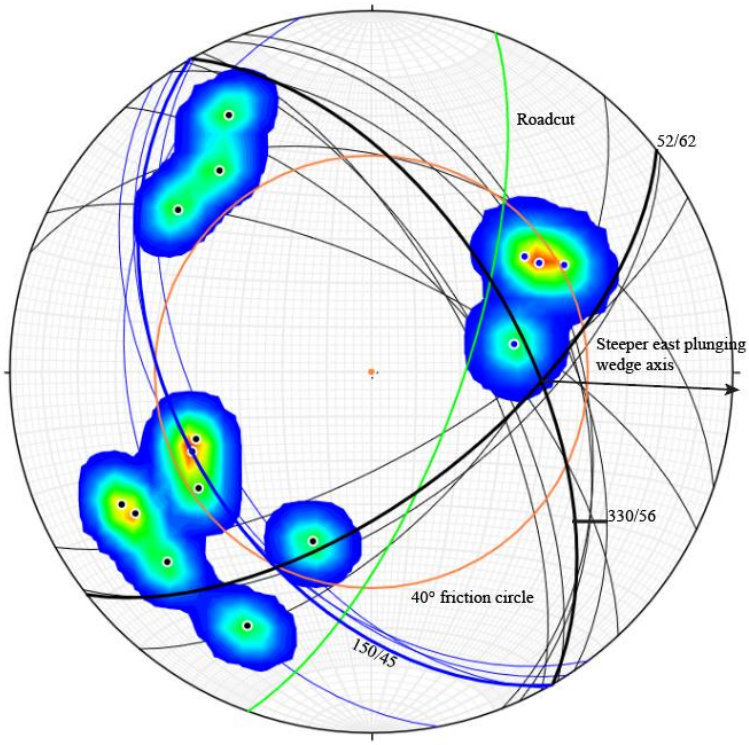

Figure 52: Stereonet showing fracture planes and poles with contours south of LS1.

3.2.5 Area North of LS1, At LS2

Measurements taken around LS2 show that the foliation intersects with most of the fractures at angles less than 40 degrees and much of the major intersections occur outside of the friction circle envelope therefore wedge failure is unlikely unless other factors (e.g lower ϕ, water pressure) are considered (Fig. 53). Some east-dipping fractures in this area are in the daylighting portion though throughout the area north of the wedge landslide. One wedge landslide (LS2) has been observed in this area which was relatively smaller in comparison to LS1 (Fig. 54) and slide LS3 that occurs further north of this part of the study area. Comparing the east dipping fractures to the roadcut suggests that several fractures have a steep enough dip and are within the 15 degrees of strike of the original roadcut to be considered daylighting planes. Some portions of the fractures have epidote while others

do not with the main slide surface containing the mineral. The trend and plunge of this wedge axis is 151/27.

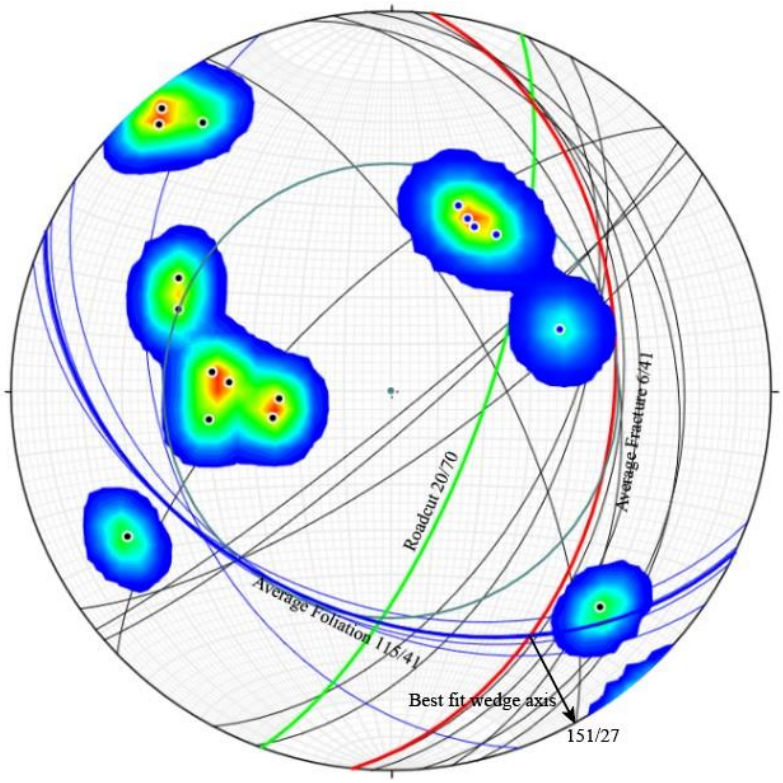

Figure 53: Measured fractures (black) and foliations (blue) with roadcut (green) around LS2. Average fractures in bold red and foliations in bold blue. Circle represents 40 degrees friction circle for reference.

Figure 54: Photo taken of LS2 showing wedge features.

3.2.6 Landslide 3

The landslide site located furthest north from the wedge and north of the parking lot was called LS3. Compared to nearby road cuts, foliation orientations had changed significantly at the base area where things could be measured reasonably by Dr. Nourse. Slopes were slippery and difficult to scramble up so most of the measurements were made on the bottom portion of the landslide no higher than 15 or so feet in elevation from the base (Fig. 55). A few fractures, including the presumed slip surface were sighted from the base of the slope. These foliation-controlled fractures were striking more or less west while dipping to the south from 26 degrees to 41 degrees. The strike of the roadcut was at about N50E with an assumed original dip of 70SE. The strike of the slide surface itself was at about N60E with an approximate dip of 30 degrees to the SE putting it within the daylighting envelop; i.e., within the region where plane intersects with the roadcut causing it to be out of slope. In comparison to the roadcut, the steepest measured foliation was N72E 34SE. It was not difficult to see that the foliations upslope, nearer to where the failure occurred, are subparallel to what the landslide plane was inferred to be (Fig. 56).

Figure 55: LS3 towards the top of the image with the breakaway point the steep surface on top. Seems to have a planar surface.

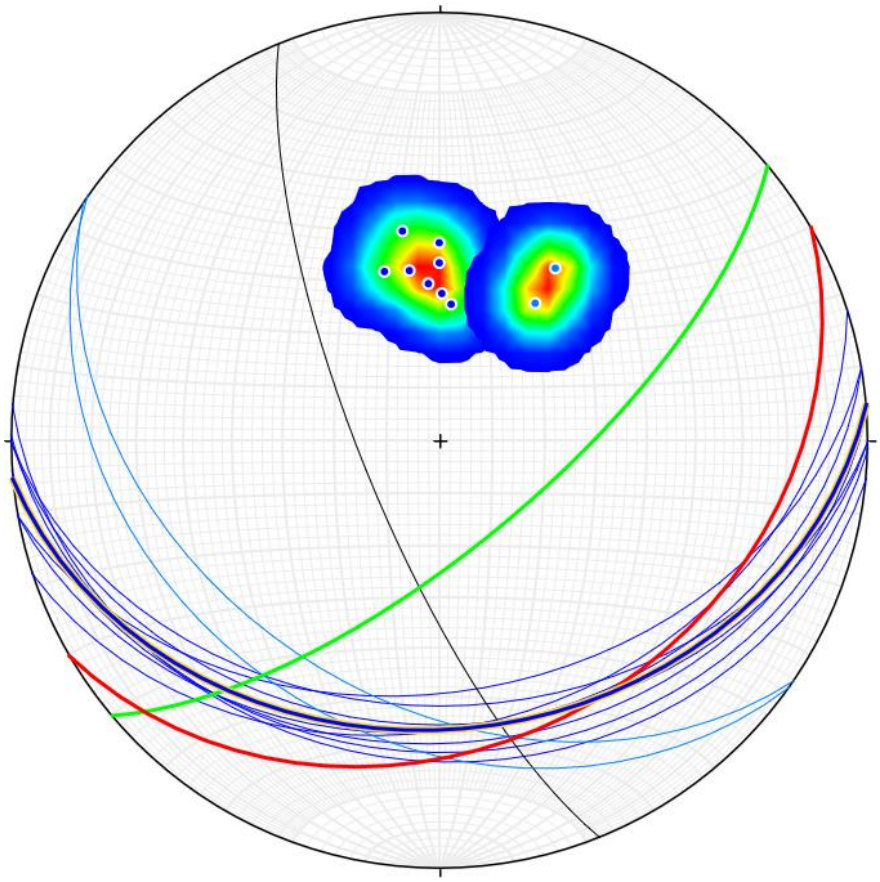

Figure 56: Showing the LS3 surface in red (60/30SE), foliations under the surface in blue with bold being the average strike (85/33SE), normal foliations south in light blue and the roadcut in bold green (50/70SE) with one fracture in black.

3.2.7 Below the Lookout

By far the area with the most diverse and complicated fractures was underneath the lookout between the Mt. Baldy Road and the Sierra Powerhouse access road (Fig. 27c). Foliations were consistent throughout the area and similar to those along the Baldy Rd. above with strikes ranging from N65W to N22W and dips ranging from 23 to 49 degrees to the SW. Fractures were clustered in scattered groups with most dipping to the NE as observed in other parts of the study region. However, there were several other clusters not observed at other sites (Fig. 57). It could be that these measurements were taken on blocks that were out of place as some had peculiar orientations. It was not uncommon to see boulders which had slumped and become out of place because of it (Fig. 58).

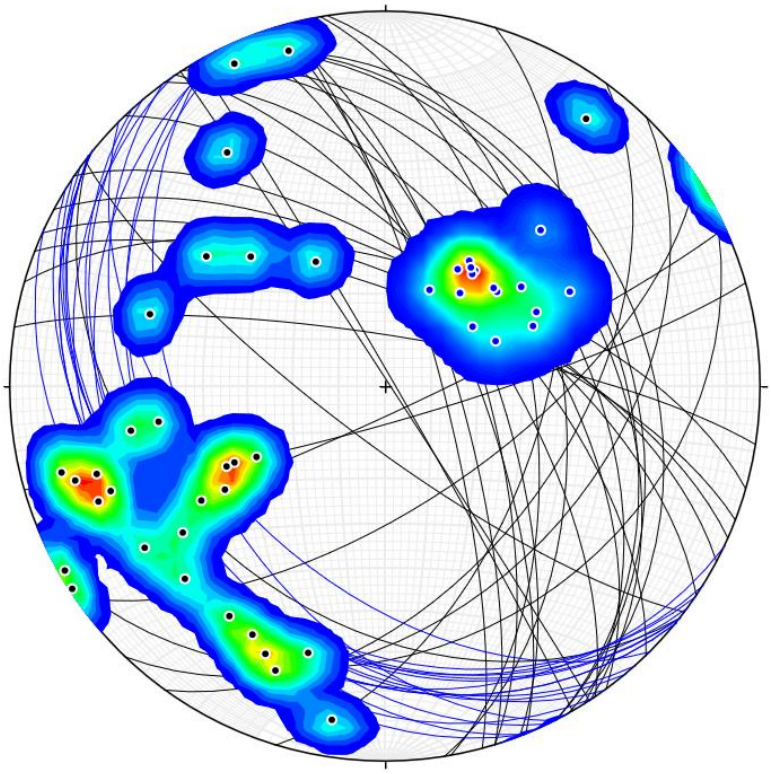

Figure 57: Foliations in blue with fractures in black below the lookout on the Sierra Powerhouse access road. Some outliers of fractures potentially due to out of place blocks which looked in place.

Figure 58: Fractures and foliation below lookout.

3.2.8 Epidote Data (LS1)

Rakes were measured on some of the striated epidote surfaces at the LS1 site. These represent micro faults in the area with some movement on them during time periods in the past (Fig. 59). The shallow to moderately plunging striations represent strike slip fault activity probably related to the ancestral San Antonio Canyon Fault (Nourse, 2003). Much of these measurements were taken along fracture surfaces in and around the area of LS1.

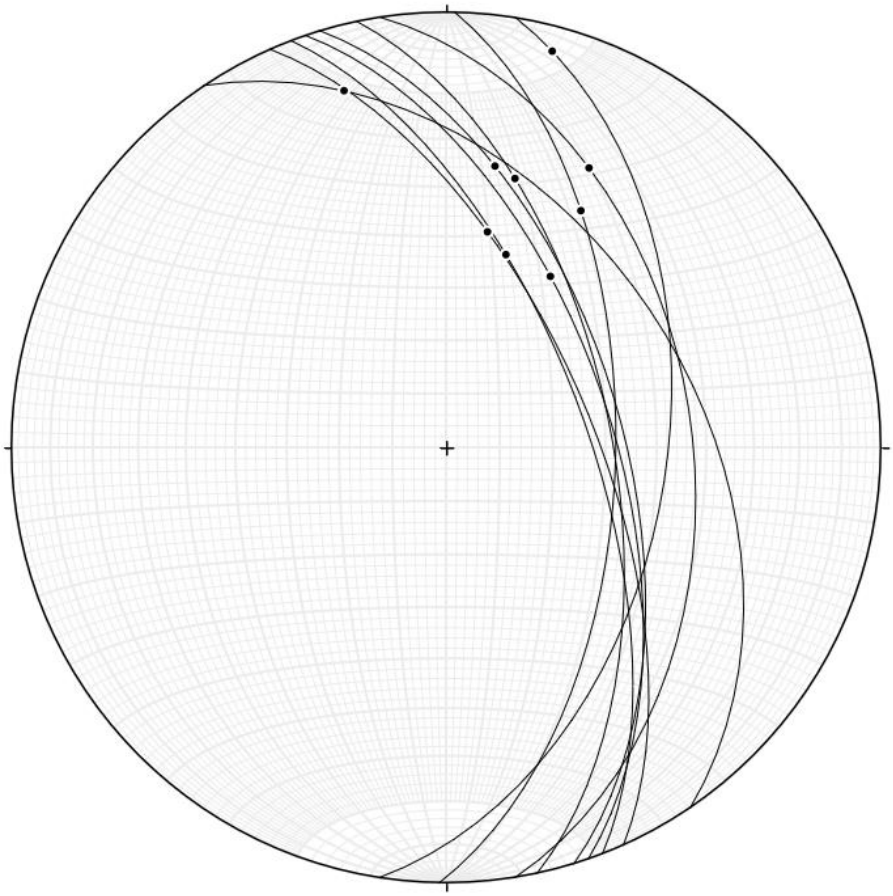

Figure 59: Epidote data where lines are striated fault planes and dots are the striations. Taken within the LS1 surface on the southern plane.

3.3 Laser Range Finder Data Results

Laser rangefinder data was collected over the course of four trips throughout the fall and winter months of 2019-2020 to be able to accomplish a few goals (Fig. 60). One was to help create a topographic map of certain features not resolvable on the standard 40 ft-contour USGS contour map. A second goal was to create a high-resolution map of the failed wedge landslide surface to later be input into ArcGIS to develop a three-dimension image of it. Eventually this data is used to calculate the missing volume above the slide surface.

Figure 60: Mom's perspective of me taking data.

Initial base stations were located with GPS. Each trip the laser rangefinder was set up in the same spot unless a move was necessary. In these cases, the instrument was used to find the distance between the two locations to ensure continuity of data without creating any unnecessary errors. The GPS has a typical error range of 3m depending on the signal from the satellites. Photos from the past that showed landslide debris cones at LS1, LS2 and LS3 (now removed) were cross referenced with the current appearance of the sites. With photos from different perspectives, I was able to trace out the rough dimensions of the cone on the ground for my mom to be able to use an apparatus I made to create a consistent target so that each measurement would be taken at a consistent marking at 1.7m of relief above the ground. This approach was used for all three of the landslide cones at LS1, LS2 and LS3 (Figs. 27b/c) for later volume calculations. Due to the uncertainty of how the landscape was shaped prior to the landslides at the LS2 and LS3, it was difficult to determine an accurate area to cover with the laser rangefinder to input data constraints into the model. Therefore, volume calculations at these sites were done only on the cone data.

Plotting the previously mentioned data with xyz coordinates resulted in a contour map with an interval of 5 m. This topographic data provided ArcGIS the necessary information to create a 3D shape in the program that could be used to calculate the missing volume of the wedge landslide. A zoomed-out map to show the context of the slide is shown in Figure 61.

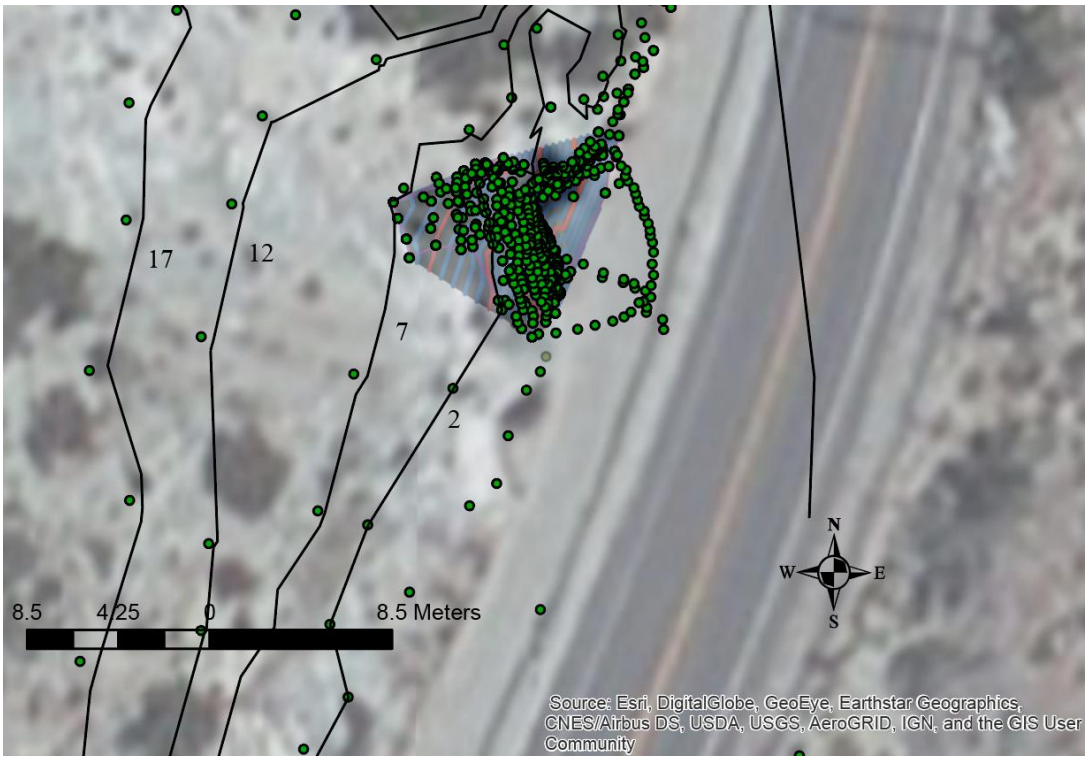

Figure 61: Zoomed out map showing context for volume calculations of Fig. 62. Contours are in m.

Using a series of tins and isolating the points taken on the outermost parts of the landslide, I was able to create a surface that projected how the original appearance of the section was before the wedge landslide failure. Inputting all of this data into ArcGIS allowed for it to calculate a surface difference using a series of polygons between the hypothetical original surface and the surface measured underneath with the laser rangefinder. A secondary calculation of the volume difference between the two surfaces yielded a relatively accurate estimation of the material that was missing (Fig. 62).

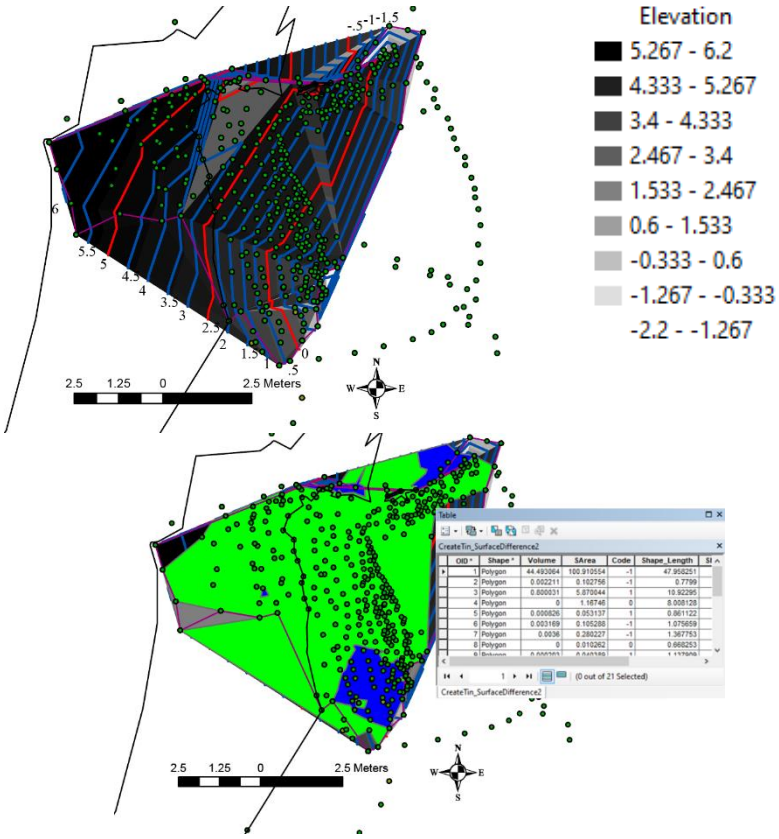

Figure 62: ArcGIS method using various polygons to determine the volume missing under the wedge's (LS1) original surface. Laser rangefinder data was used to first create a 3D model of the wedge followed by using edge points to create an original surface mesh from which individual polygons can be used to see how much volume is missing. Volume units are in m^3. Contours .5 m intervals.

It should be noted that this approach gives a greater volume to that of using the cone method as missing volume represents an aggregate of many past failures while the debris cone represents a single event. Final volume was 43.69m^3 after accounting for a .8m^3 discrepancy. Some of the volume seems to appear to be above that of the original surface but the volumes are insignificant in nature so the outcome of the calculations through the program are unaffected. More detailed description with images of steps can be found in the methods section.

3.4 ArcGIS Data Application to Landslide Cones

Laser rangefinder data was used to approximate the height and width of the debris cone at LS1 that was observed in a 2017 photograph (Fig. 28). In the area next to the road there is a level ditch which seems to have been one of the preventative measures in place to prevent debris going onto the road along with the natural slope which was present. The width of the cone was measured by the rangefinder using control points on the photo. Despite the unusual characteristics of this cone such as steeper on the uphill versus downhill slope, calculations normalized this cone by assuming the volume of material would be the same as long as the radius is well constrained (Fig. 63) and height at the apex of the cone (Fig. 64) is known.

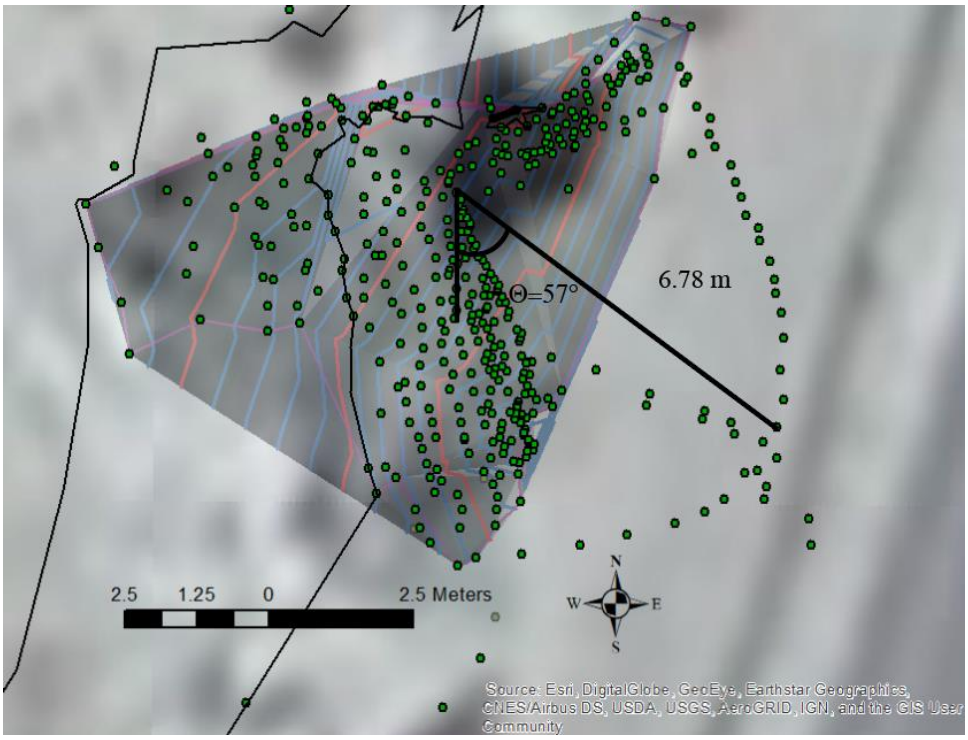

Figure 63: Radius measured on ArcGIS also along the cross-section line.

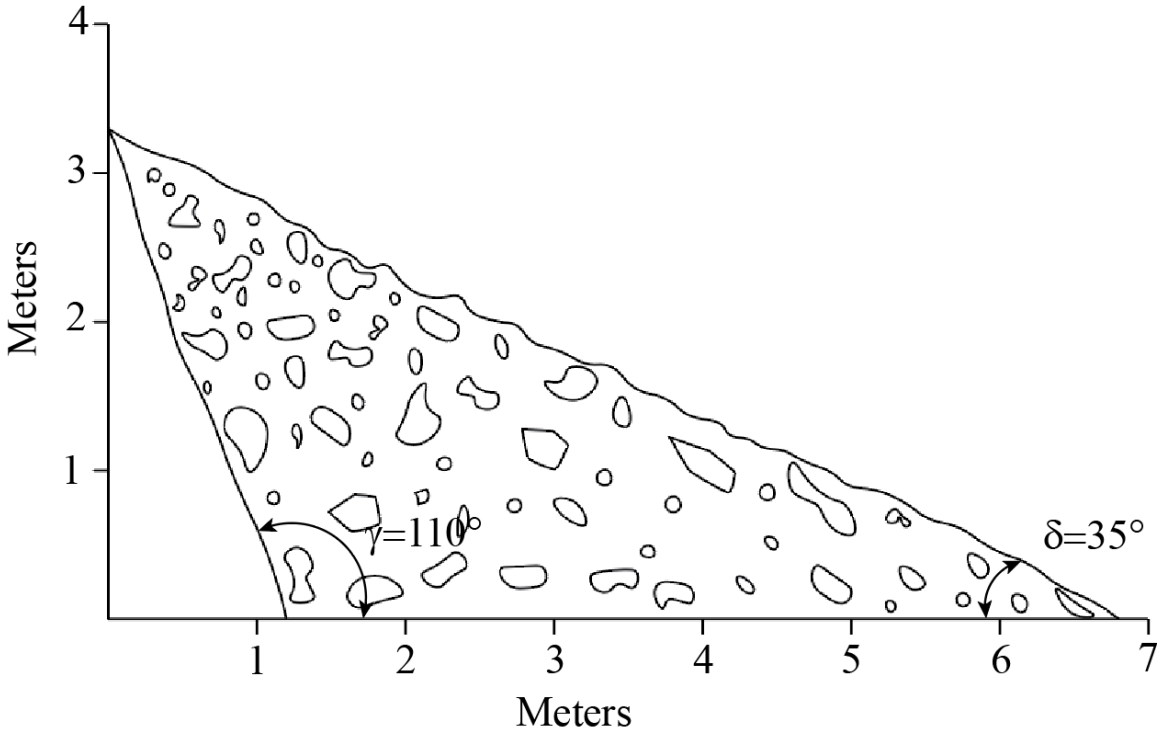

Figure 64: Cross section of cone for LS1.

The following equation will be used to calculate the volume of the cones using dimensions measured from ArcGIS where R is the radius, Θ is the position where the cone is cut in radians, γ is the cut angle (roadcut) and δ is the angle of the base of the cone (Fig. 65). Cut angle will be 110 instead of 70 since the formula below solves for the cut volume

$$V = \frac{R^3}{3}\left\{\Theta \tan\delta + \tan\gamma \sin\Theta \cos^2\Theta - \tan\gamma(\cos\Theta + a)^3 F\right\}$$

$$F = \frac{1}{2(a-1)^2}\left\{-\frac{1+K^2}{K^2}\left(\frac{1}{t+K}+\frac{1}{t-K}\right)+\frac{K^2-1}{K^3}\log\left|\frac{t-K}{t+K}\right|\right\}$$

$$\text{where,}\quad a=\frac{\tan\delta}{\tan\gamma}\quad K=\sqrt{\frac{1+a}{1-a}}\quad t=\tan\frac{\Theta}{2}$$

Note 1. Θ: Position where the cone is cut, expressed in terms of angle [rad] (not degree)
Note 2. log : Natural logarithm (not common logarithm)

and not the uncut one. F is a constant that changes depending on the dimensions a, K and t used to substitute for π through a derivation.

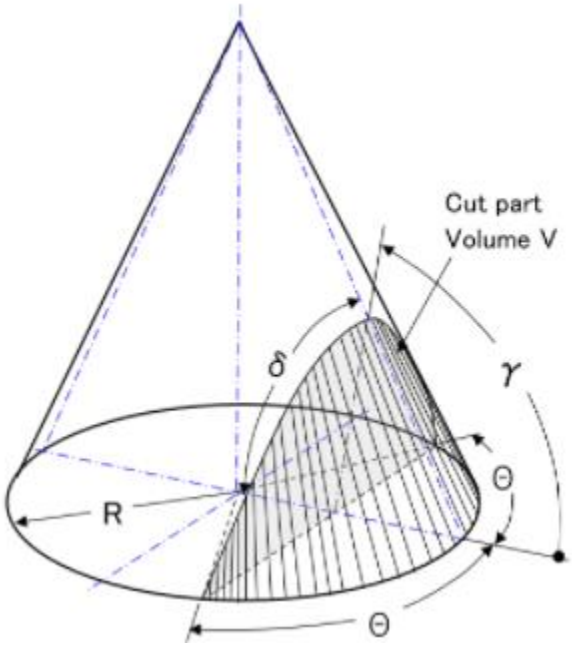

Figure 65: Schematic diagram showing the different angles and dimensions needed for the calculation.

When it comes to the cone of LS1, quite a bit must be assumed about what were the original dimensions of the cone when it initially failed. Even in 2017, the photographs taken seemed to be more for the debris that came down from above versus the actual dimensions of LS1 so comparisons to the LS2 cone were made to get a rough approximation of what they would have been. For larger boulders, the cones seemed to favor being at about a 45-degree angle so the radius would be similar to the height though the height is not used in this instance. However, the cone observed had a base angle of around 35 degrees so that is what is used (Fig. 64). The measured radius was about 6.8m. Cut position of the cone was estimated to be at around 57 degrees with a base angle of 35 degrees and a cutting angle of 110 degrees yielding a volume of 26.5m^3 or 935.8ft^3.

To determine the weight of the slide mass, the cone volume was multiplied by the approximate unit weight of rock which is 160 lbs/ft^3 and also by .7 to account for the 30% porosity estimated for rocks in the cone of a landslide after failure for a final weight of 104,810 lbs. For comparison of the volumes, it is approximated the volume of the cone would be about 18.55m^3 when accounting for porosity while the ArcGIS estimation was 43.69m^3. A larger original cone with a radius of 7.2, base angle of 45 assuming larger and more angular rocks, and a cut position of 60 degrees would yield a cone slightly larger than the one computed on ArcGIS at 44.5m^3.

LS2 required the use of only the cone data in order to be able to approximate the volume of material which had destabilized and come down from the slope since brush in the area caused for unreliable reading on the obscured surfaces. Figure 66 shows the area of the landslide surface was approximated using the laser rangefinder while referencing Figure 67 in the field to be imported into ArcGIS later. Using the interpolate polygon with heights in ArcGIS, the surface area of the slide surface was found to be about 14.1m^2 based off the approximate area in Figure 68. The next step was to take measurements from the cone of LS2 from the images (Fig. 69) and measure the diameter to then get a radius of about 3.68 m, base angle of 45 degrees, 70 degrees on the cut position and a cut angle of 110 yielding a volume of 15.3 m^3. This result multiplied by .7 to take into account 30% porosity yields a volume of 10.7 m^3 which is then converted to 377.9 ft^3 for a final weight of 60,464 lbs.

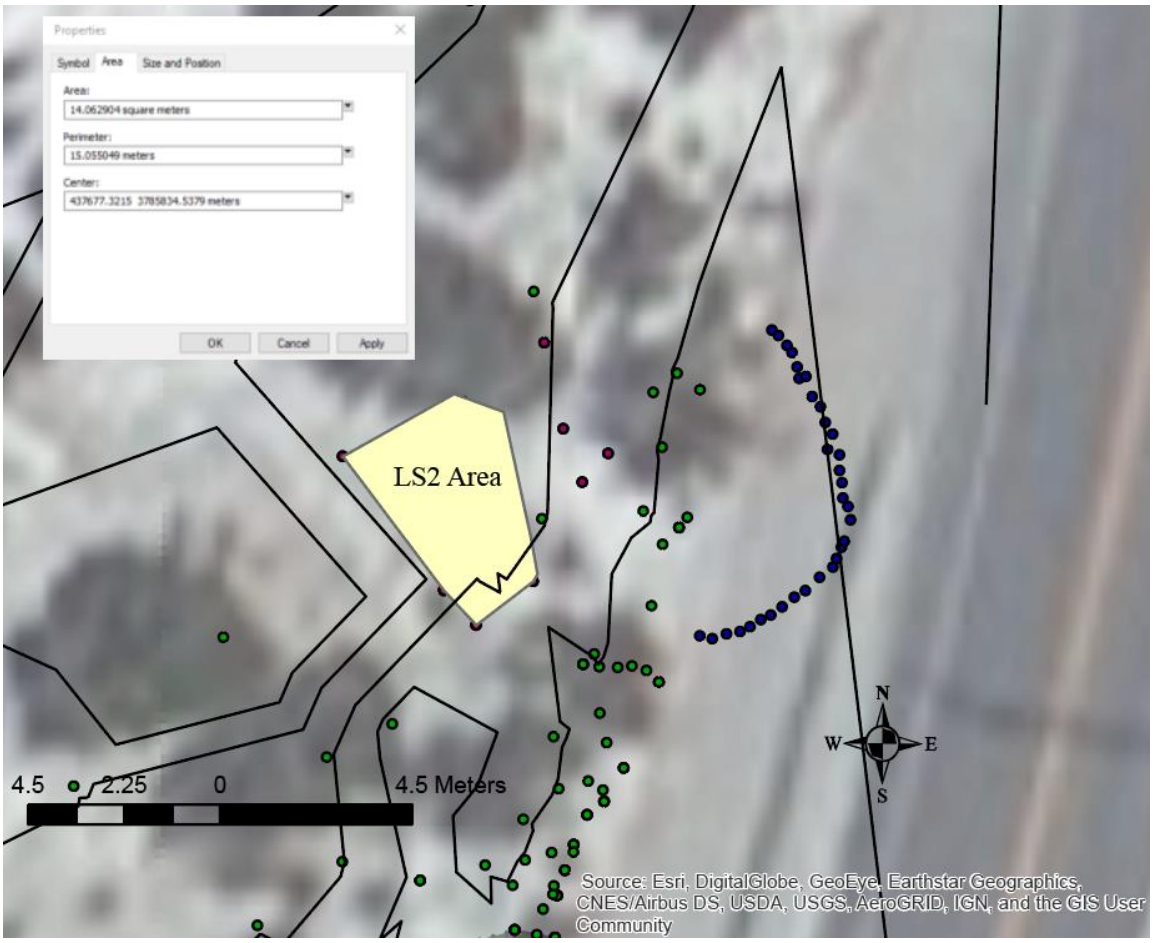

Figure 66: Showing LS2 slide surface in beige with its area measured on the little box. Blue dots represent the outline of the cone for the slide with green dots along the higher parts of it.

Figure 67: Photo of the cone of LS2 which was used to approximate dimensions by Laser Rangefinder after the debris were cleared. Photo taken by Dr. Nourse in 2017.

Figure 68: Photo of the failure surface taken by Dr. Nourse in 2017.

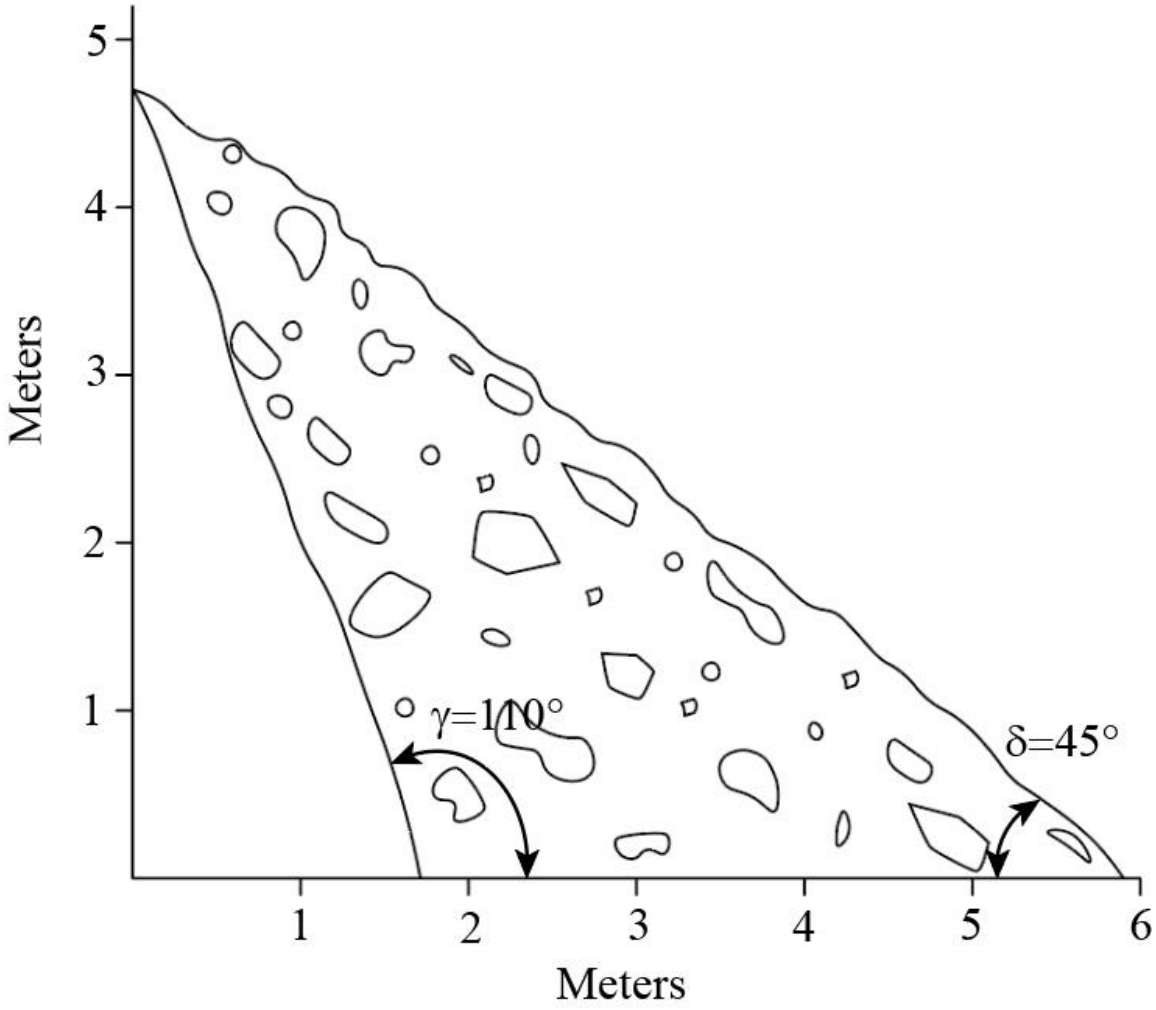

Figure 69: Cross section of cone for LS2.

LS3 data was derived from measurements of the suspected landslide surface (Fig. 71) using the same method as in LS2 to derive an area of 40.9m^2 (Fig. 70). This area could be larger as explained later. Measurements of the debris cone (photographed in 2019; Fig. 72) were done on ArcGIS to calculate the radius of the cone (Fig. 73). It is assumed that the radius from the measured cone of 10.1 m, base angle of 30 degrees, cut position of 70 degrees and a cut angle of 110 degrees resulted in a volume of 155.9 m^3. This result multiplied by .7 to take into account 30% porosity yields a volume of 109.1 m^3 which is then converted to 5505.6 ft^3 to result in a weight of 616,627 lbs (279697 kgs).

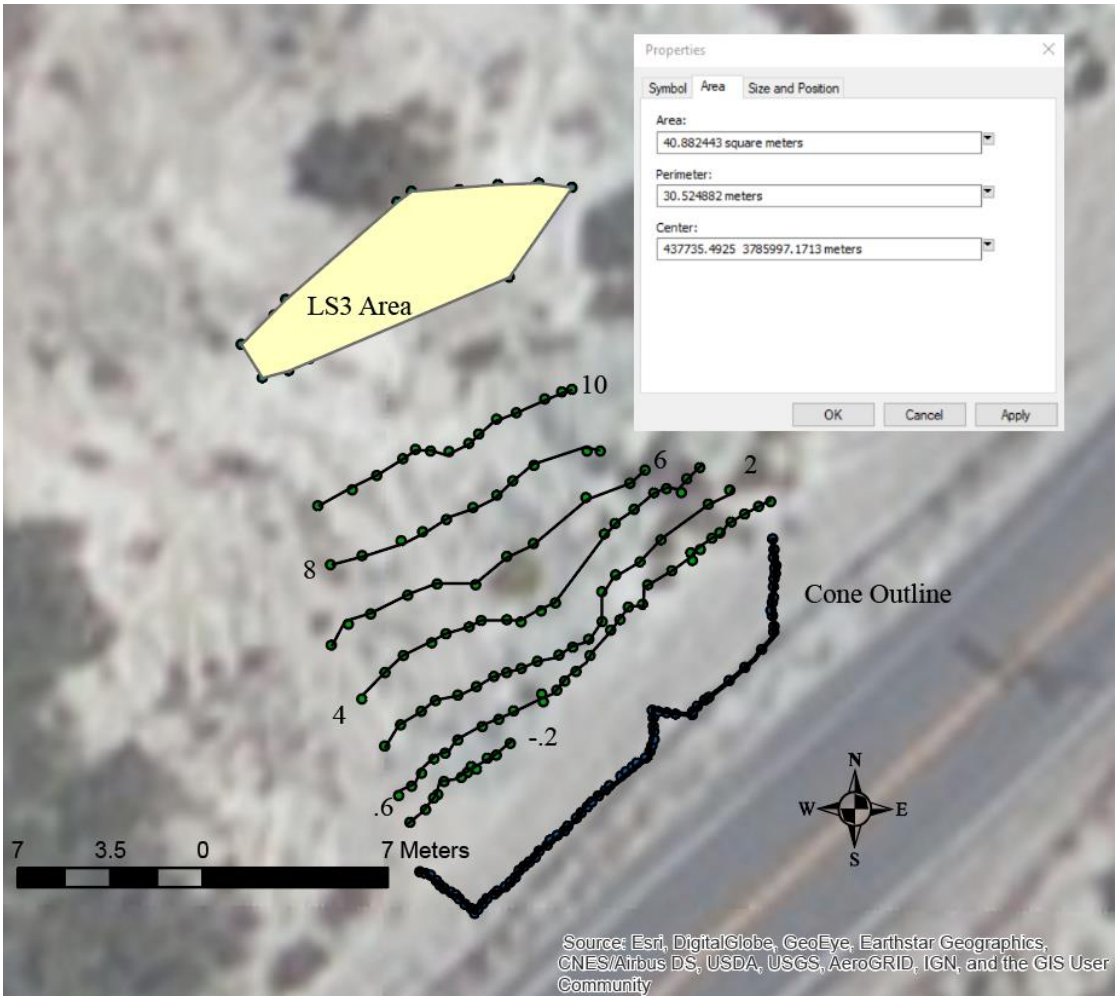

Figure 70: LS3 exposed slide surface area calculated on ArcGIS from imported rangefinder data.

Figure 71: Photo of the failure surface of LS3 taken by Dr. Nourse on February 11, 2019. Suspected failure surface in blue. Some of the slide surface may still be buried so area could be larger. Scarp seen above the failure area.

Figure 72: Image of the LS3 cone used to approximate the volume of material with slide surface in blue. Photo by Dr. Nourse February 11, 2019.

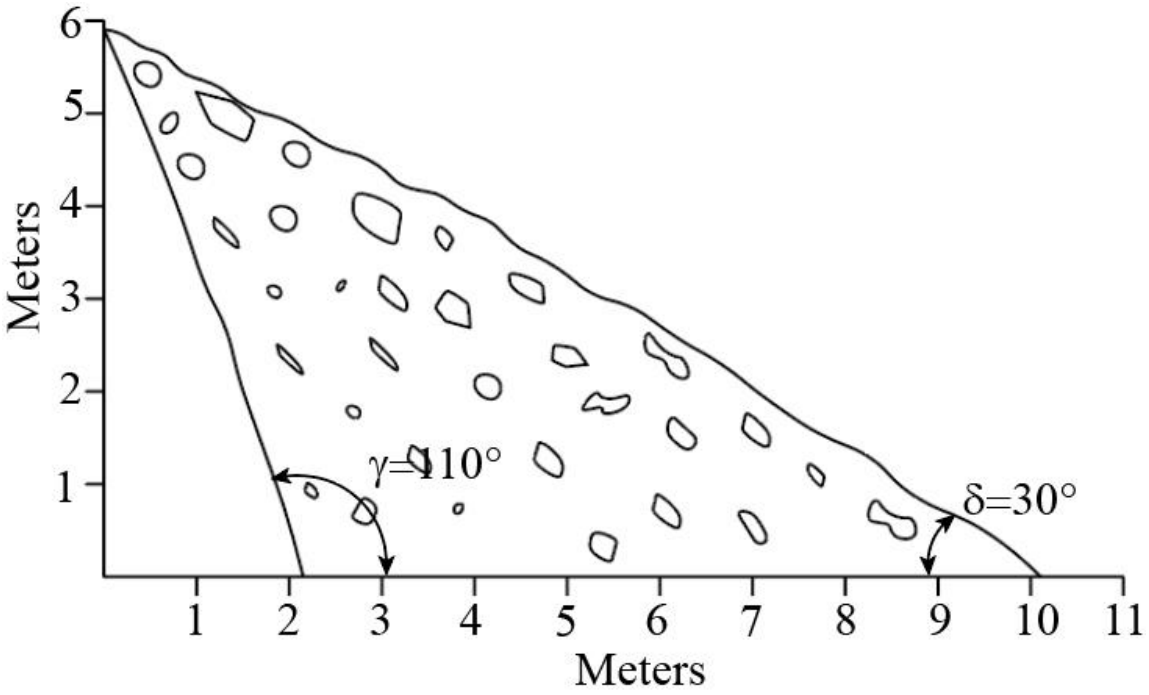

Figure 73: Cross section of cone of LS3.

Volumes were calculated by approximated angles for the different parameters below. This volume was in m^3 so it was converted to ft^3 before multiplying by the standard weight of rock. The result was multiplied by .7 to account for the porosity of the debris cone to give a final weight in pounds. Results for all three landslides are presented in Table 1 with LS1 having an additional volume from the void calculation from ArcGIS.

LS1							
Radius m	Θ	γ	δ	Volume m^3	Volume ft^3	Weight lbs with 30% porosity	Volume m^3 ArcGIS
6.8	57	110	35	26.5	935.8	104810	43.69
LS2							
Radius m	Θ	γ	δ	Volume m^3	Volume ft^3	Weight lbs with 30% porosity	
3.68	70	110	45	10.7	377.9	60464	
LS3							
Area m^2	Radius m	Θ	γ	δ	Volume m^3	Volume ft^3	Weight lbs with 30% porosity
40.88	10.1	70	110	30	155.9	5505.6	616628

Table 1: Calculated parameters for volume of the landslide debris cones at sites LS1, 2 and 3.

CHAPTER 4: SAFETY FACTOR ANALYSIS

4.1 Safety Factor Analysis

Safety factors are calculated below for the three landslides (LS1, LS2 and LS3), using measurements from the sites and also other figures derived through approximation. LS1 and LS2 were both wedge landslides that needed to be calculated using a complex formula that took into consideration cohesion and water while a simpler friction only equation was also be used to compare the cases. LS3 is a planar landslide which required the use of different equations along with the necessity to find a good approximate weight and volume of material. To set up the equations, I followed the approaches detailed in chapters 6 and 7 of Wyllie and Mah, 2004. Stereonets were used for the three landslides to determine the strikes and dips of potential failure surfaces with respect to the roadcut for Mt. Baldy Road and to ensure the direction of failure would be in the direction of the road. They were also used for the angles (Figs. 56, 74, 76, 78 and 80) put into the formulas to determine safety factor. Dimensions and shapes of the failure surfaces were found via laser rangefinder along with the dimensions and volumes of the debris cones.

4.2 Safety Factor Wedge Landslide (Complex Formula)

Calculating the safety factor of the LS1 and LS2 are important in determining the metrics by which the failure occurred. Back calculations were needed for this in that we used a safety factor of 1 as the initiation of the failure to calculate values of cohesion and friction angle which could account for the failure conditions. Two different methods were used in order to calculate the volume: (1) using laser rangefinder data to calculate the volume of the cone of the landslide debris and then adjusting this volume for about 30%

porosity, and (2) using laser rangefinder data imported into ArcGIS with a projection technique to determine the missing volume from the wedge landslide mass. Equations from Hoek and Bray's Rock Slope Engineering: Third Edition (1981) and Wyllie and Mah's Rock Slope Engineering: Civil and Mining (2004) were used to calculate the various parameters to determine the final safety factor:

$$F = \frac{3c_A}{\gamma H} \cdot X + \frac{3c_B}{\gamma H} \cdot Y + \left(A - \frac{\gamma_w}{2\gamma} \cdot X\right) \tan\phi_A + \left(B - \frac{\gamma_w}{2\gamma} \cdot Y\right) \tan\phi_B$$

F is the Safety factor which is being solved for. Cohesive strengths for the two slopes for the wedge failure are shown as c_A and c_B. γ is the unit weight of rock while γ_w represents the unit weight of water. H is the total height of the wedge from the base of the failure surface to the top of it. Φ_A and Φ_B are the angles of friction on plane A and plane B.

In the previous equation, there are four additional variables which have not been discussed as of yet which are X, Y, A, and B. These variables are dimensionless factors that depend on the geometry of the wedge:

$$X = \frac{\sin \theta_{24}}{\sin \theta_{45} \cos \theta_{2.\mathrm{na}}}$$

$$Y = \frac{\sin \theta_{13}}{\sin \theta_{35} \cos \theta_{1.nb}}$$

$$A = \frac{\cos \psi_a - \cos \psi_b \cos \theta_{na.nb}}{\sin \psi_5 \sin^2 \theta_{na.nb}}$$

$$B = \frac{\cos \psi_b - \cos \psi_a \cos \theta_{na.nb}}{\sin \psi_5 \sin^2 \theta_{na.nb}}$$

All of the angles needed for the equations rely on angles found on a stereonet (Fig. 25) between different intersections of planes. These are denoted by the multiple subscripts. ψ_a and ψ_b are the dips of planes A and B with ψ_5 is the plunge angle in the direction of failure at the intersection of planes A and B.

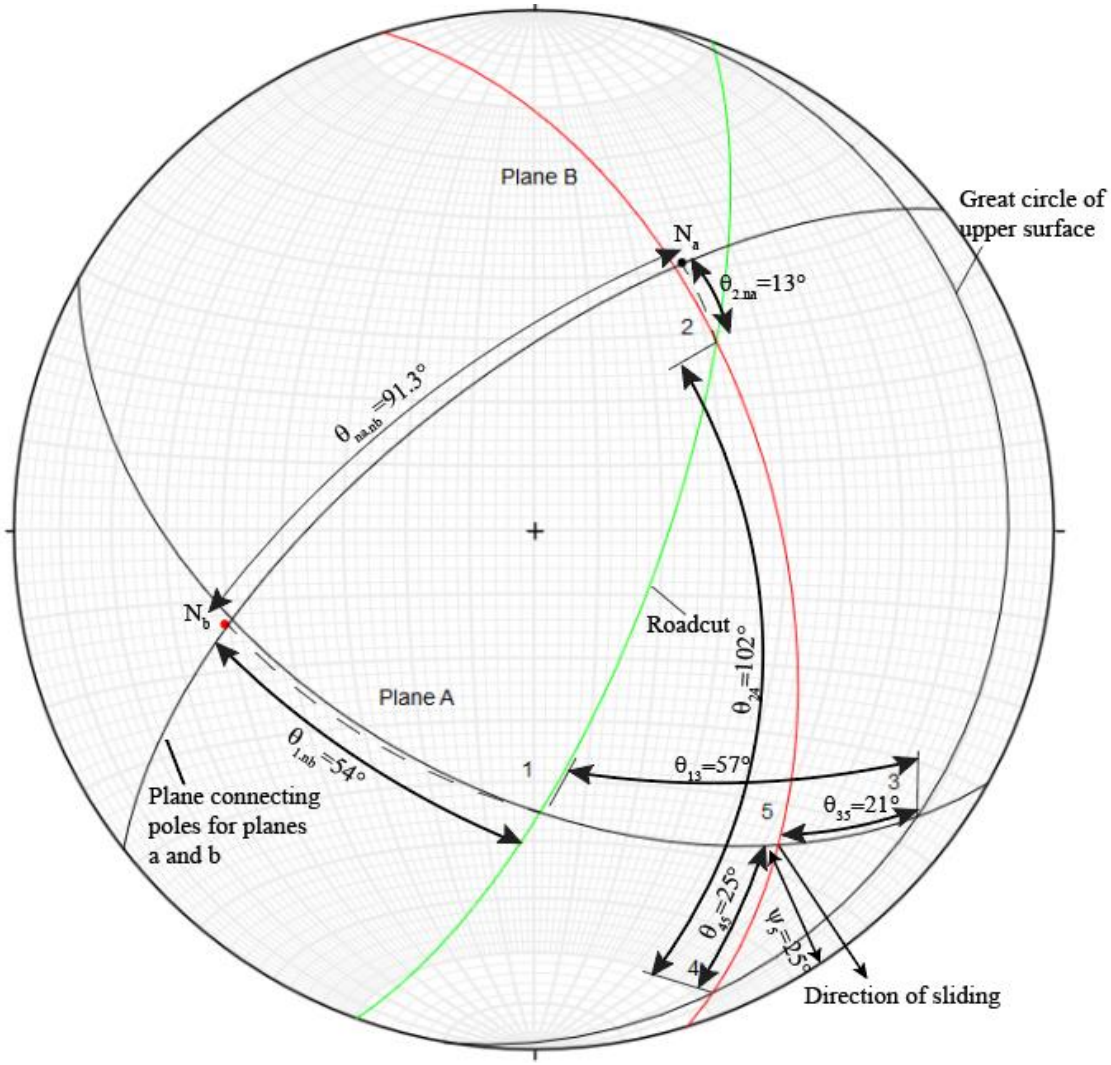

Figure 74: Stereonet showing pertinent planes and angles used in LS1 complex safety factor equation.

Safety factor under dry conditions involves a formula with a 0 value for the weight factor of water. This affects X and Y in the second part of the equation where these constants are multiplied by the unit weight of water thereby cancelling them out. The two constants are still used when used in the first part of the equation involving cohesion along with the unit weight of the rock.

Under wet conditions, a unit weight factor of water of 62.4 lbs/ft^3 was used to calculate the safety factor (Hoek and Bray, 1981.) Water along the wedge failure plane acts

as a buoyant force which increases the driving stress in relationship to the resisting stress, causing the safety factor to be lower than what it otherwise would be. It is assumed that there will be an even distribution of water from the top of the surface to the bottom.

Table 2 shows the way in which the four variables for the equation are solved for using the parameters measured on the stereonet in Figure 74. Once these values were solved, they were input into excel using the standard weights for both the rock and water with one of the water weights being set at 0 for the dry case in Table 3. The resulting values of cohesion necessary to maintain a safety factor of 1 after the point where the friction angle goes down to a critical point.

Wedge Stability Calculation Sheet		
Input Data	Function Value	Calculated Answer
$\psi_a = 49°$ $\psi_b = 52°$ $\psi_5 = 25°$ $\theta_{na.nb} = 91.3°$	$\cos \psi_a = .6561$ $\cos \psi_b = .6157$ $\sin \psi_5 = .4226$ $\cos \theta_{na.nb} = -.0227$ $\sin^2 \theta_{na.nb} = .9995$	$A = \frac{cos\psi_a - cos\psi_b * cos\theta_{na.nb}}{sin\psi_5 * sin^2\theta_{na.nb}}$ $A = \frac{.6561 + .6157 * .0227}{.4226 * .9995}$ $A = 1.5864$ $B = \frac{cos\psi_b - cos\psi_a * cos\theta_{na.nb}}{sin\psi_5 * sin^2\theta_{na.nb}}$ $B = \frac{.6157 + .6561 * .0227}{.4226 * .9995}$ $B = 1.4929$
$\theta_{2\,4} = 102°$ $\theta_{4\,5} = 25°$ $\theta_{2.na} = 13°$	$\sin\theta_{2\,4} = .9781$ $\sin\theta_{4\,5} = .4226$ $\cos\theta_{2.na} = .9744$	$X = \frac{sin\theta_{24}}{sin\theta_{45} * cos\theta_{2.na}}$ $X = \frac{.9781}{.4226 * .9744}$ $X = 2.3753$
$\theta_{1\,3} = 57°$ $\theta_{3\,5} = 21°$ $\theta_{1.nb} = 54°$	$\sin\theta_{1\,3} = .8387$ $\sin\theta_{3\,5} = .3584$ $\cos\theta_{1.nb} = .5878$	$Y = \frac{sin\theta_{13}}{sin\theta_{35} * cos\theta_{1.nb}}$ $Y = \frac{.8387}{.3584 * .5878}$ $Y = 3.981$

Table 2: Showing the calculations needed to solve for the four variables needed for the complex wedge landslide equation for LS1.

Dry Case					
Cohesian A lbs/ft^2	Cohesion B lbs/ft^2	Friction A	Friction B	Safety Factor	Rock Weight(lb/ft^3)
0	0	45	45	3.08	160
0	0	40	40	2.58	Water Weight(lb/ft^3)
0	0	35	35	2.16	62.4
0	0	30	30	1.78	Height (ft)
0	0	25	25	1.44	28.5
0	0	20	20	1.12	Water Weight(lb/ft^3) dry
0	0	18	18	1.00	0
42	42	15	15	1.00	X
110	110	10	10	1.00	2.3753
149	149	7	7	1.00	Y
Wet					3.981
Cohesian A lbs/ft^2	Cohesion B lbs/ft^2	Friction A	Friction B	Safety Factor	A
0	0	45	45	1.84	1.5864
0	0	40	40	1.54	B
0	0	35	35	1.29	1.4929
0	0	30	30	1.06	
0	0	28.7	28.7	1.01	
35	35	25	25	1.00	
80	80	20	20	1.00	
122	122	15	15	1.00	
162	162	10	10	1.00	
186	186	7	7	1.00	

Table 3: Results of the safety factor calculations using the more complex equation to account for cohesion, friction and (in the wet case) water for LS1. Those cohesion and friction values when the safety factor is at 1 are the results of "back calculation" to understand possible parameters for failure.

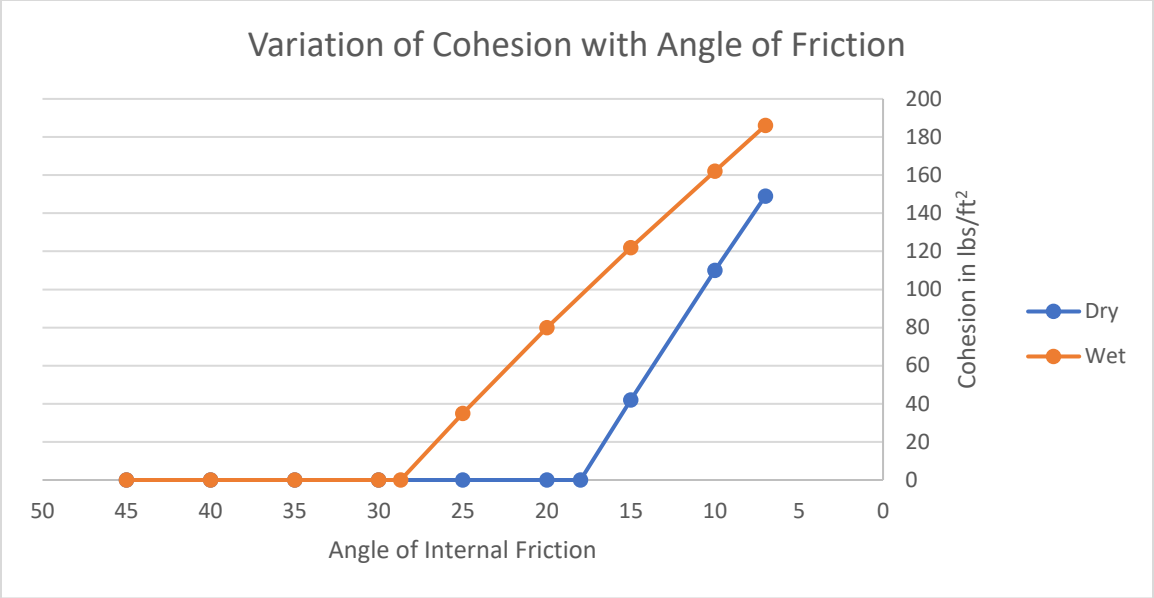

Figure 75: Chart showing the variation of cohesion with respect to the angle of friction needed to create a safety factor of 1 under dry and wet conditions.

Graphical analysis of the results (Fig. 75) shows some reasonable patterns under the dry and wet conditions. In the dry case, cohesion is not necessary to stabilize the slide mass until friction angle dips below 18 degrees. This landslide was stable under normal conditions that assume a 25 degrees friction angle for epidote but failed because of the change under wet conditions as cohesion was needed for values below 28 degrees. Cohesion values required for stability are low which should be expected due to the small scale of this slide and the material that consist of the plane (Appendix B). Low values correlated by infilled fractures as shown in the table of the plate. Larger cohesion values likely would be needed to overcome any driving forces to the magnitude of those observed in the Hogback Landslide. All of these values seem to be reasonable given the conditions under which these events took place.

LS2 used the same approaches as LS1 when it comes to finding the values needed from a stereonet (Fig. 76) to plug into the equations to solve for the variables X, Y, A and B for the complex equation. These values are then written down in Table 4 to solve for the four variables before going on to the final step of solving for the values. Parameters are plugged in to solve for cohesion values to maintain a safety factor of 1 in Table 5.

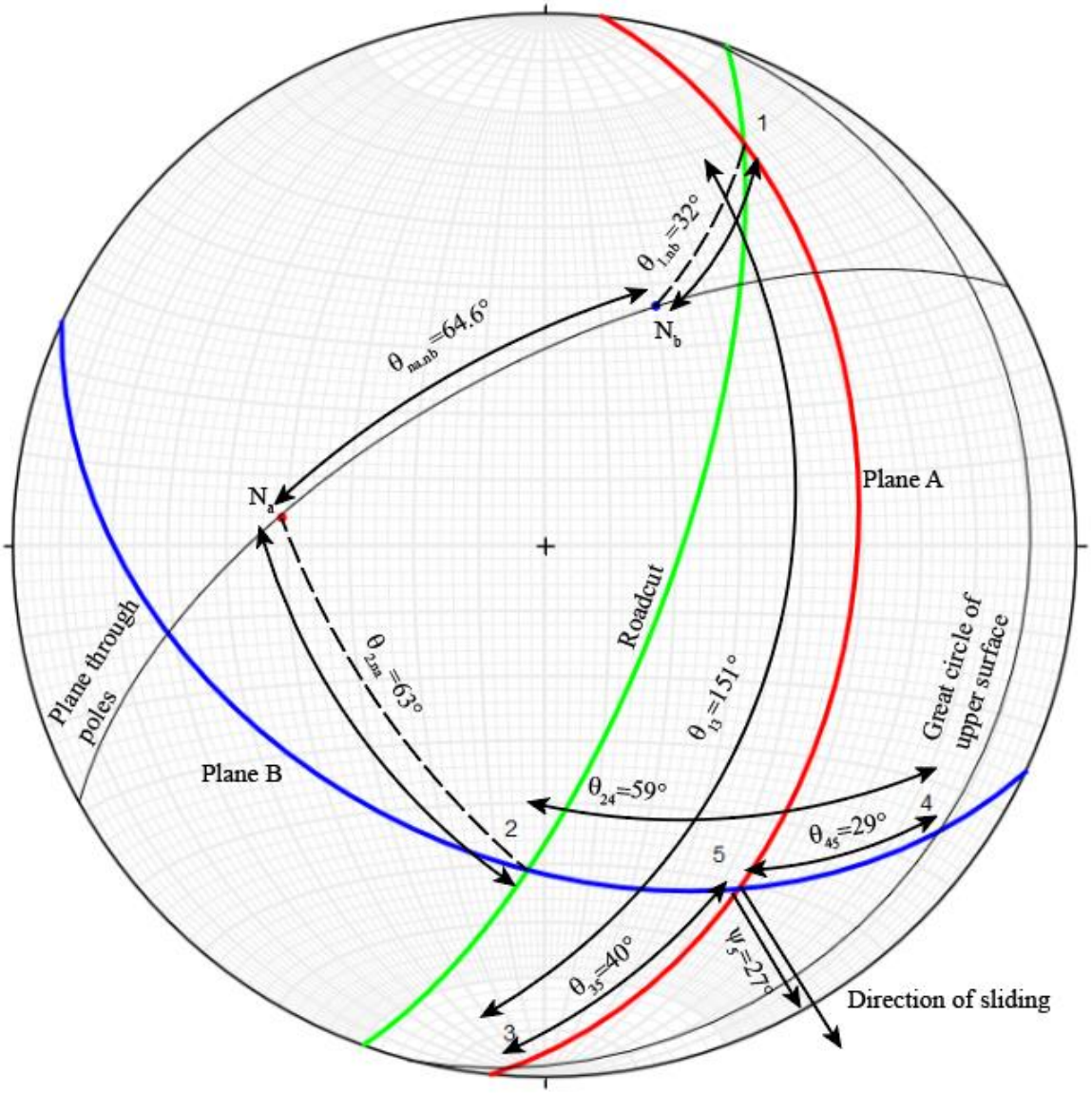

Figure 76: Stereonet showing pertinent planes and angles used in LS2 complex safety factor equation.

Wedge Stability Calculation Sheet		
Input Data	Function Value	Calculated Answer
$\psi_a = 41°$ $\psi_b = 41°$ $\psi_5 = 27°$ $\theta_{na.nb} = 64.6°$	$\cos \psi_a = .7547$ $\cos \psi_b = .7547$ $\sin \psi_5 = .4540$ $\cos \theta_{na.nb} = .4289$ $\sin^2 \theta_{na.nb} = .8160$	$A = \frac{cos\psi_a - cos\psi_b * cos\theta_{na.nb}}{sin\psi_5 * sin^2\theta_{na.nb}}$ $A = \frac{.7547 - .7547 * .4289}{.4540 * .8160}$ $A = 1.1634$ $B = \frac{cos\psi_b - cos\psi_a * cos\theta_{na.nb}}{sin\psi_5 * sin^2\theta_{na.nb}}$ $B = \frac{.7457 - .7457 * .4289}{.4540 * .8160}$ $B = 1.1634$
$\theta_{2\,4} = 59°$ $\theta_{4\,5} = 29°$ $\theta_{2.na} = 63°$	$\sin\theta_{2\,4} = .8572$ $\sin\theta_{4\,5} = .4848$ $\cos\theta_{2.na} = .4540$	$X = \frac{sin\theta_{24}}{sin\theta_{45} * cos\theta_{2.na}}$ $X = \frac{.8572}{.4848 * .4540}$ $X = 3.8946$
$\theta_{1\,3} = 151°$ $\theta_{3\,5} = 40°$ $\theta_{1.nb} = 32°$	$\sin\theta_{1\,3} = .4848$ $\sin\theta_{3\,5} = .6428$ $\cos\theta_{1.nb} = .8480$	$Y = \frac{sin\theta_{13}}{sin\theta_{35} * cos\theta_{1.nb}}$ $Y = \frac{.4848}{.6428 * .8480}$ $Y = .8894$

Table 4: Showing the calculations needed to solve for the four variables needed for the complex wedge landslide equation for LS2.

Dry					
Cohesian A lbs/ft^2	Cohesion B lbs/ft^2	Friction A	Friction B	Safety Factor	Rock Weight(ft^3)
0	0	45	45	2.33	160
0	0	40	40	1.95	Water Weight(ft^3)
0	0	35	35	1.63	62.4
0	0	30	30	1.34	Height (ft)
0	0	25	25	1.09	13.1
0	0	23.3	23.3	1.00	Water Weight(ft^3) dry
22	22	20	20	1.00	0
55	55	15	15	1.00	X
86	86	10	10	1.00	3.8946
104	104	7	7	1.00	Y
					0.8894
Wet					A
Cohesian A lbs/ft^2	Cohesion B lbs/ft^2	Friction A	Friction B	Safety Factor	1.1634
0	0	45	45	1.39	B
0	0	40	40	1.17	1.1634
0	0	35.7	35.7	1.00	
4	4	35	35	1.00	
29	29	30	30	1.00	
51	51	25	25	1.00	
72	72	20	20	1.00	
92	92	15	15	1.00	
110	110	10	10	1.00	
121	121	7	7	1.00	

Table 5: Results of the safety factor calculations using the more complex equation to account for cohesion, friction and (in the wet case) water for LS2. Those cohesion and friction values when the safety factor is at 1 are the results of "back calculation" to understand possible parameters for failure.

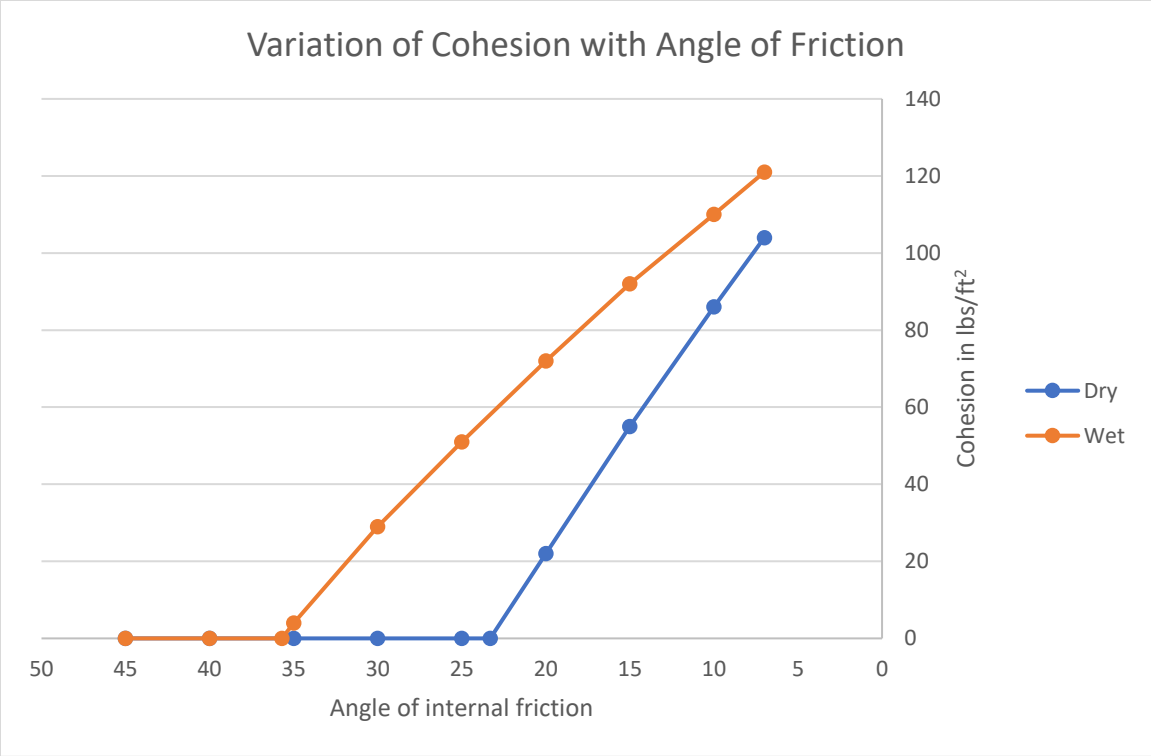

Figure 77: Chart showing the variation of cohesion with respect to the angle of friction needed to create a safety factor of 1 for LS2.

Graphical analysis of the results (Fig. 77) shows some reasonable patterns under the dry and wet conditions for LS2. Cohesion is not necessary to stabilize the slide mass until friction angle dips below 23 degrees under dry conditions. This landslide was stable under normal conditions that assume a 25 degrees friction angle for epidote but failed when wet conditions were introduced as cohesion was needed for values below 35 degrees. Low values of cohesion were once again expected like in the case of LS1 due to the small size of the failure. All of these values seem to be reasonable given the conditions under which these events took place in with infilled fractures dictating cohesion (Appendix B).

4.3 Wedge Analysis (Friction Only Where C=0)

A simpler calculation which was done to be under the dry conditions without cohesion was done to determine what the safety factor would be when friction was the only

determining factor for the case. This scenario may be more appropriate for an earthquake September. This one had far less variables but necessitated the use of a stereonet to determine the angles needed in order to solve the equation. $FS = \frac{(R_A+R_B)tan\Phi}{Wsin\psi_i}$ along with $R_A + R_B = \frac{W*cos\psi_i*sin\beta}{sin\frac{1}{2}\xi}$. Plugging in these values back into the equation creates a situation in which the W values cancel out due to them being in the numerator and denominator, so weight is not necessary to solve for the FS value and instead leaves over a dimensionless ratio that defines the safety factor. The equation also has cos over sin so that simplifies to a tan value leading to the following equation $FS = \frac{sin\beta}{\sin(\frac{\xi}{2})} * \frac{tan\Phi}{tan\psi_i}$.

Values needed to input into the equation above will be found on the stereonet in Figure 78 which were measured in the stereonet program to solve for LS1. Half of the angle between the planes along with the one from the center to the ground surface were measured along the stereonet for input into the safety factor equation. Weight cancels out in the zero-cohesion case so it will be displayed as a comparison between the two methods to find volume but is not relevant to the final equation setup in Table 6. Plunge of the wedge axis was also referenced on the stereonet though an additional one would be solved for assuming a steeper wedge axis in Table 7.

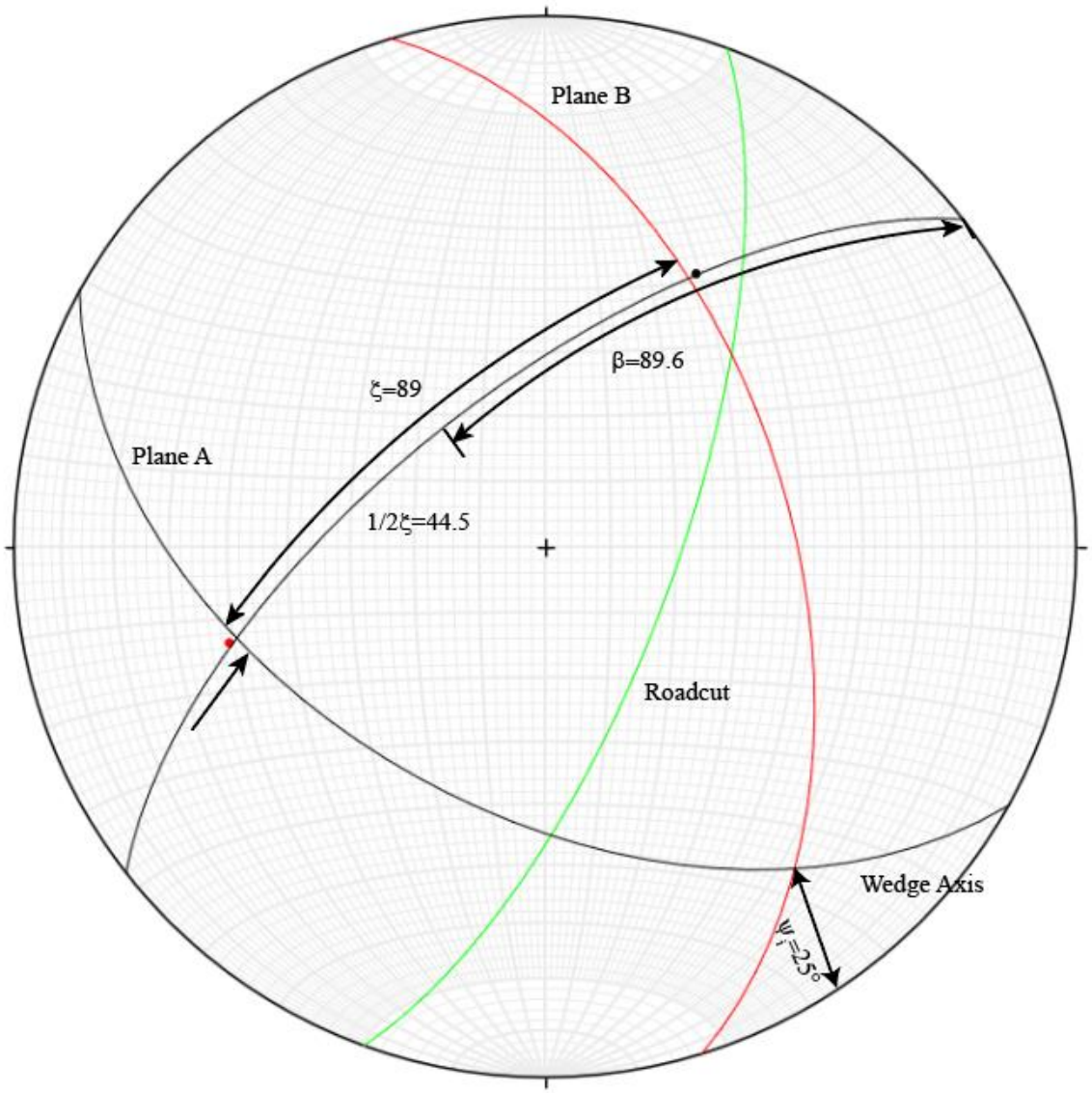

Figure 78: Summary stereonet diagram showing planes and angles used in friction only safety factor calculation at LS1.

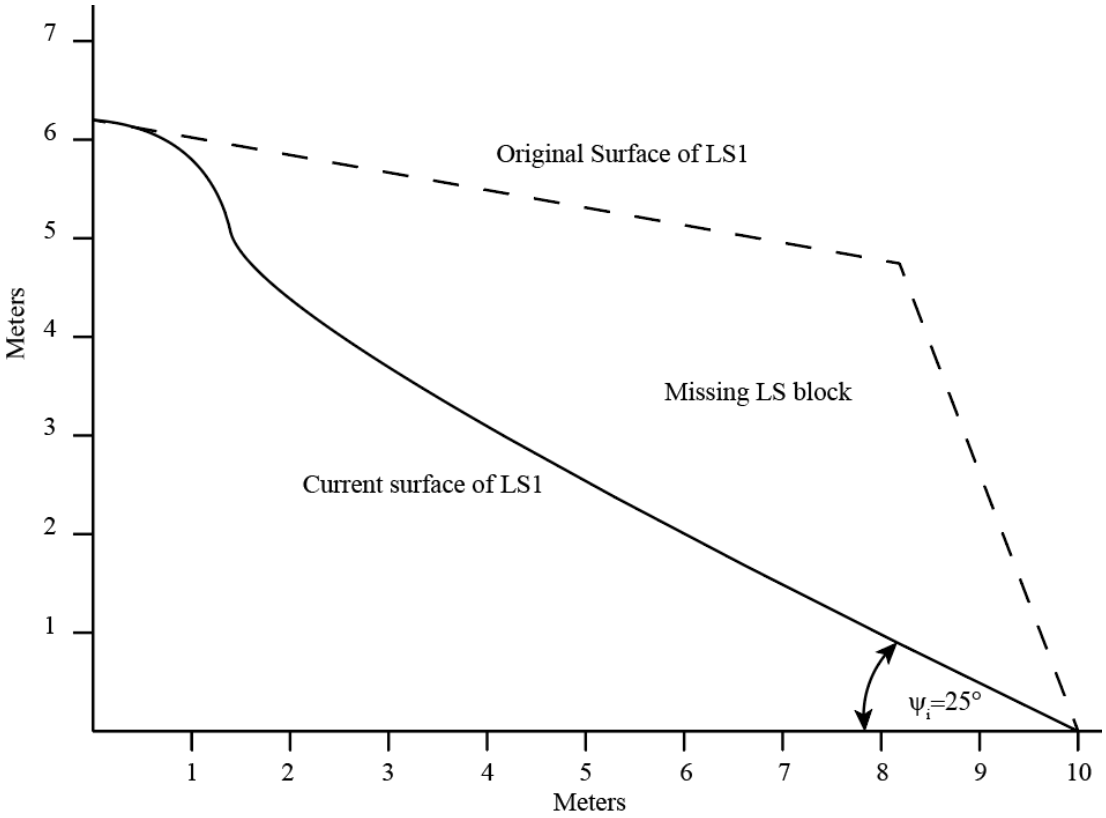

Figure 79: Cross section of LS1 showing the approximate original surface and the current surface showing the line of intersection of the two planes also known as the wedge axis.

Friction					
Friction angle Φ	ψ_i	W lbs	ArcGIS W lbs	1/2 ξ	β
25	25, 30	248120	251403	44.5	89.6

Table 6: Values needed for friction only case and comparison of weights derived from ArcGIS and cone. Weights are not used in the calculations below.

$$FS = \frac{sin\beta}{\sin\left(\frac{\xi}{2}\right)} * \frac{tan\Phi}{tan\psi_i} = \frac{sin51.7}{sin44.5} * \frac{tan25}{tan25} = 1.12$$

ψ_i	25	ψ_i	30
Φ	Safety Factor	Φ	Safety Factor
40	2.57	40	2.07
30	1.77	30	1.43
25	1.43	25	1.15
20	1.11	22	1.00
18	1.00	20	0.90
15	0.82	15	0.66
7	0.38	7	0.30

Table 7: Results of the friction only case with ψ_i being 25 degrees on the left and 30 on the right.

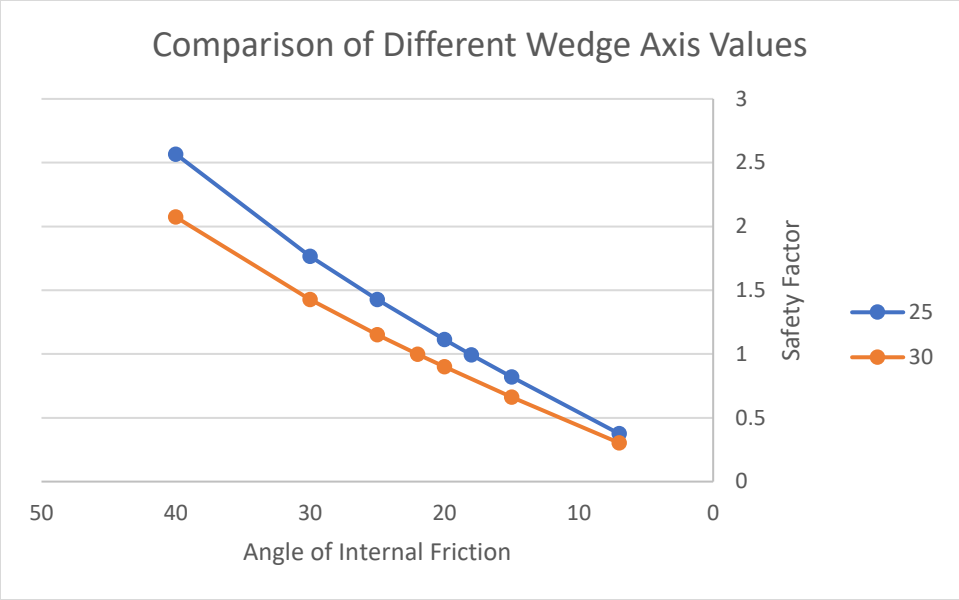

Figure 80: Chart comparing safety factor values with ψ_i values of 25 (blue) and 30 (orange) for LS1 under friction only case with C=0.

It can therefore be concluded that under conditions in which there are no other outside influences, this wedge failure would not have begun due to a safety factor higher than one. A lower friction angle would be needed in order to drive the safety factor low enough to be unstable. There still is enough of a drop-off that the difference a few degrees would put this landslide into the failure zone at a slightly higher dip value. This is displayed in Figure 80 where ψ_i are solved for values of 25 and 30 degrees. The reason why a higher angle was also solved for was to see the effect of a higher value due to other intersections happening at these increased dips show in Figure 48. Back calculations are not possible for cohesion since the only variable which is able to be changed is the angle of friction.

The same procedures to find the friction only case for LS1 was applied to LS2 when using a stereonet (Fig. 81) to find the values of ξ and β for use in the formulas. Table 8 shows the results of the calculations for both the measured ψ_i value of 27 and one of the steeper angles which was suggested on the stereonet from Figure 53. A cross section was created in Figure 82 to show the angle of wedge axis needed schematically.

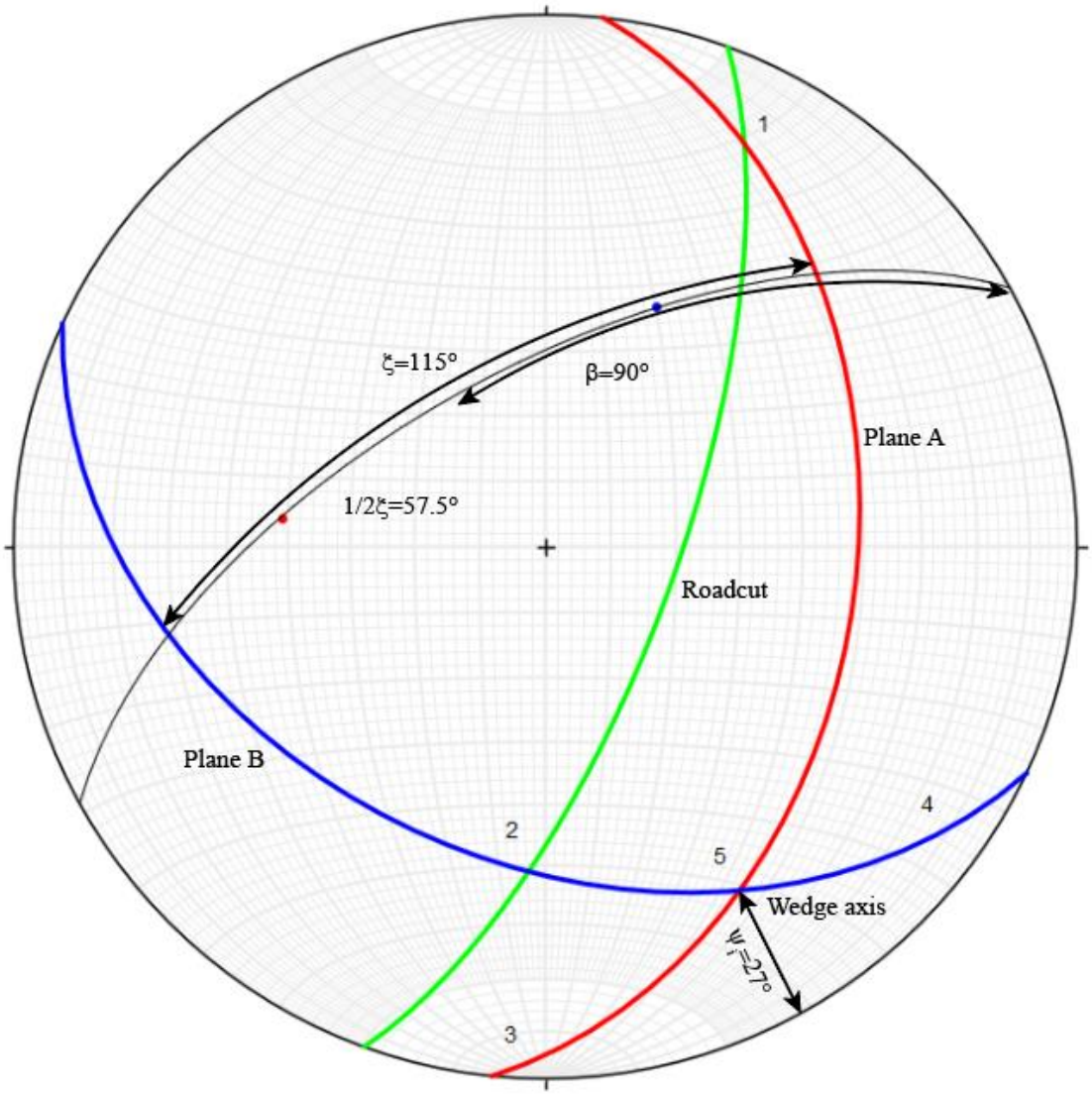

Figure 81: Stereonet showing friction only parameters for LS2 to be used in the friction only equation.

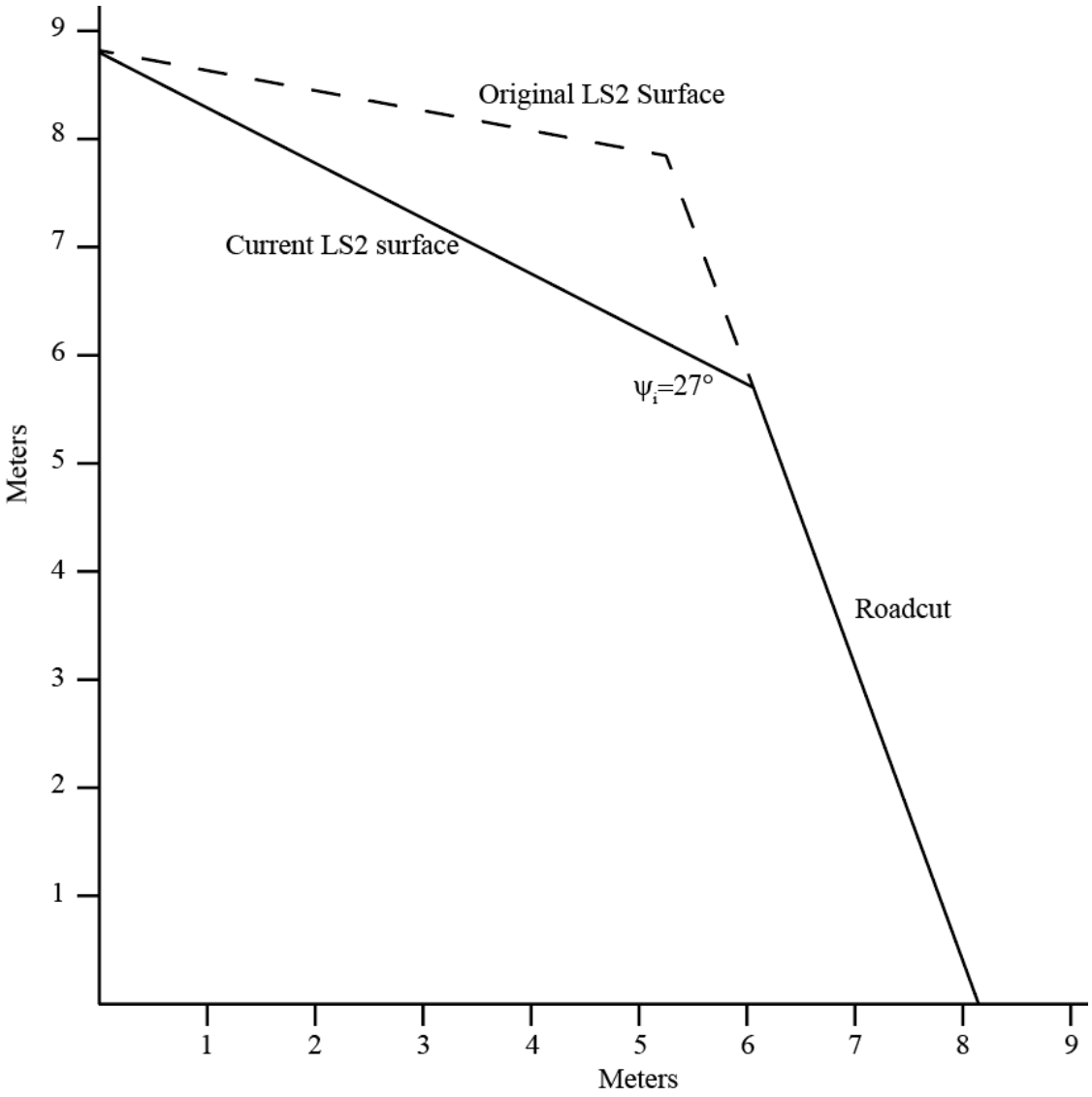

Figure 82: Cross section of LS2.

ψ_i	1/2 ξ	β	ψ_i	1/2 ξ	β
27	57.5	90	32	57.5	90
Φ	Safety Factor		Φ	Safety Factor	Φ
40	1.95		1.59	40	
30	1.34		1.10	30	
25	1.09		1.00	28	
23	1.00		0.88	25	
20	0.85		0.69	20	
15	0.62		0.51	15	

Table 8: Safety factor under friction only comparing ψ_i values of 27 and 32.

$$FS = \frac{sin\beta}{\sin\left(\frac{\xi}{2}\right)} * \frac{tan\Phi}{tan\psi_i} = \frac{sin45.6}{sin57.5} * \frac{tan25}{tan27} = .78$$

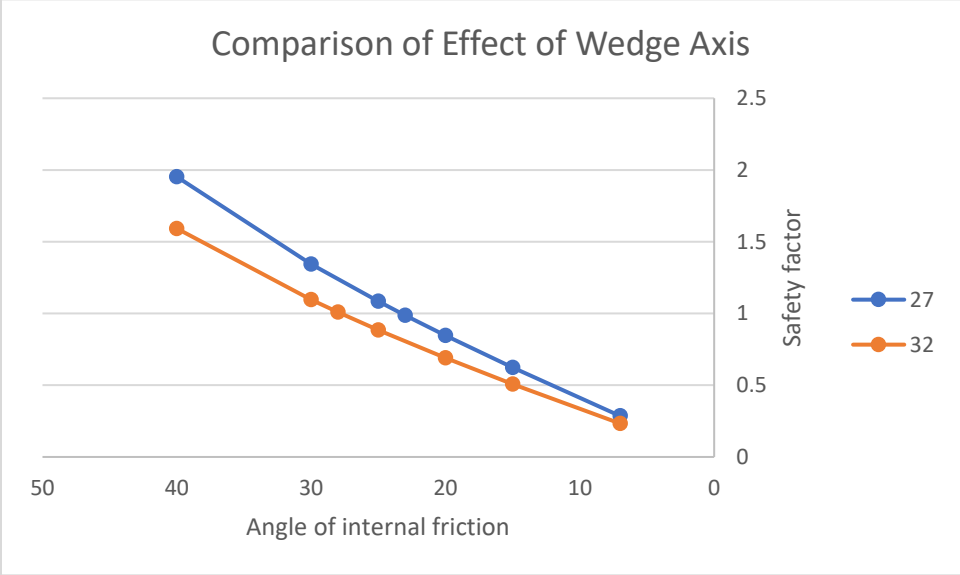

Figure 83: Effects of an increase in wedge axis on the resulting safety factor solution.

Wedge failure would not have occurred in circumstances where only friction was affecting the failure as seen in Table 8. Outside variables were in play in order to have failure occur at that point. An increase in the ψ_i value from 27 to 32 decreases the safety factor values at each respective angle with the most noticeable decrease occurring at the larger values (Fig. 83). This adjustment shows that more angles with the higher value could potentially have made it closer to the failure point at the average angle observed in the stereonet from Figure 80.

4.4 Planar Landslide Safety Factor Analysis of LS3

Landslide 3 was identified to be a classic plane failure scenario which would not involve the complexities of the wedge calculations where far more factors played a role in the ability for the plane to fail. In this analysis, it is possible to include P_{H2O} effects along base of the slide and at the rear.

As the most northern of the three studied landslides, this one had a unique characteristic in comparison to the other two in that it had a failure along the daylighting foliation plane (Figs. 56, 84) and not along intersecting fractures which were observed in other areas to the south. Foliations which were orientated differently until just south of the landslide. Foliations observed along the area below the failure surface are denoted in dark blue on Fig. 56 and strike more easterly. Those that are orientated more closely to others observed in the southern portions of the study area are annotated in light blue. The landslide failure plane (in red) was sighted from a distance to be close to the foliation planes observed. This means that the master slide plane that formed most likely was parallel to the foliation.

Figure 84: Photograph showing the LS3 failure surface up above.

Access to parts higher up was difficult as the surface was too loose to traverse up safely and gather measurements. However excellent 3D exposure allowed good distal estimations of strike and dip.

All the foliations shown on Figures 56 and 84 would be considered daylighting or close to daylighting in respect to the orientation of the road cut since they strike close to or within 15 degrees of the strike of the cut and this was assumed to have had a dip of about 70 degrees.

Under dry conditions, the following equation will be used to determine the factor of safety for these translational landslides: $SF = \frac{Resisting\ Stress}{Driving\ Stress} = \frac{C+tan\Phi[\frac{(W)cos\theta}{A}]}{\frac{(W)sin\theta}{A}}$ where SF is the safety factor, Φ is the friction angle, θ is the dip angle of the failure plane, W is the weight of the failure block (approximated with the debris cone), A is the area of the failure plane and C is the cohesion. Back calculations to find the point where SF = 1 would be done as this is considered the failing point to see what the conditions for failure in the past were.

Under wet conditions, a modification of the equation for the dry case will be used to calculate the factor of safety for translational landslides: $SF = \frac{Resisting\ Stress}{Driving\ Stress} = \frac{C+tan\Phi[\frac{(W)cos\theta-F_{H2O}\sin(50)}{A}-average\ P_{H2O}Up]}{\frac{(W)sin\theta+F_{H2O}\cos(50)}{A}}$ where the variables before are the same with the added subtraction of the pressure of water which acts within the slide plane. The first term which the pressure is being subtracted from is the pressure exerted per unit area of which the water pressure cannot be greater than. With a weight about 1/3 of the of the unit weight of the rock, it is safe to assume that the pressure within the slide plane area would be normally 1/3 of the of the pressure exerted by the weight on the surface. Figure 85 displays the different parameters needed to plug into this equation.

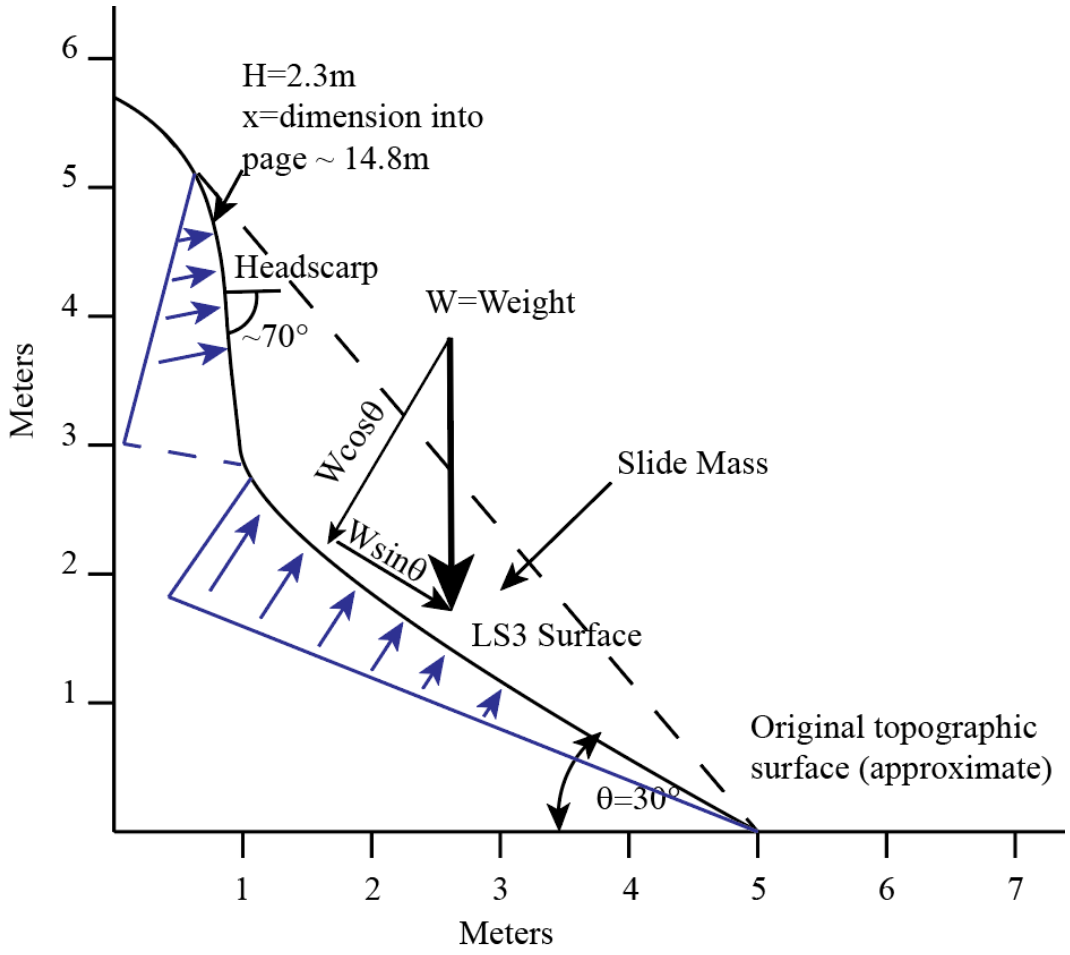

Figure 85: Cross section through LS3 showing water pressure effects.

Tables 9 and 10 are some of the parameters that were needed to plug into the safety factor calculation under both dry and wet conditions. Some of these values were solved using measurements from ArcGIS to approximate volume and weight of the landslide mass while the area was also measured using the program. Table 9 has the area directly measured from ArcGIS while Table 10 has an increase of $10m^2$ to account for any possible slide surface which was obscured by debris.

LS3				
Area m^2	Height m	Radius m	Volume m^3	Volume with Porosity
40.88	2.8	10.1	155.9	109.1
Area ft^2	Volume ft^3	Weight constant	Weight lbs	θ
440.03232	3852.8	160	616627	30

Table 9: Parameters used for safety factor calculations for LS3.

Area: 440 ft^2 (calculated by ArcGIS using the 3D function accounting for a 30 degree slope)

θ = dip of sliding plane = 30°

V = Slide volume (calculated from cone) = 3852.8 ft^3

W = Weight of slide block with a unit weight of 160 lbs/ft^3 * V = 616,627 lbs

LS3				
Area m^2	Height m	Radius m	Volume m^3	Volume with Porosity
50.88	2.8	10.1	155.9	109.1
Area ft^2	Volume ft^3	Weight constant	Weight lbs	θ
547.67	3852.8	160	616628	30

Table 10: Values for an increased area assuming some of LS3 surface is obscured.

Table 11 uses the area which was measured on ArcGIS. Comparison of values under dry and wet conditions are shown in the table and a graphical comparison of the two conditions is provided in Figure 86.

LS3					
Area m^2	Height m	Radius m	Volume m^3	Volume with Porosity	Max P Water
40.88	2.8	9.18	155.9	109.13	572.832
Area ft^2	Volume ft^3	Weight constant	Weight lbs	θ	Avg P Water
440.03232	3853.92595	160	616628.152	30	286.416
Water Constant	Height Fracture ft	Width ft	Distance ft		Tension Force Water
62.4	7.5	2	48.5		22698
Dry			Wet		
Friction Angle	Cohesion lbs/ft^2	Safety Factor	Friction Angle	Cohesion lbs/ft^2	Safety Factor
45	0	1.73	45	0	1.21
40	0	1.45	40	0	1.02
35	0	1.21	39.6	0	1.00
30	0	1.00	35	112	1.00
25	135	1.00	30	221	1.00
20	259	1.00	25	320	1.00
15	375	1.00	20	411	1.00
10	487	1.00	15	496	1.00
7	552	1.00	10	577	1.00
			7	625	1.00

Table 11: Comparison of results of safety factor calculations for LS3 under dry and wet conditions showing possible cohesion and friction angle variations.

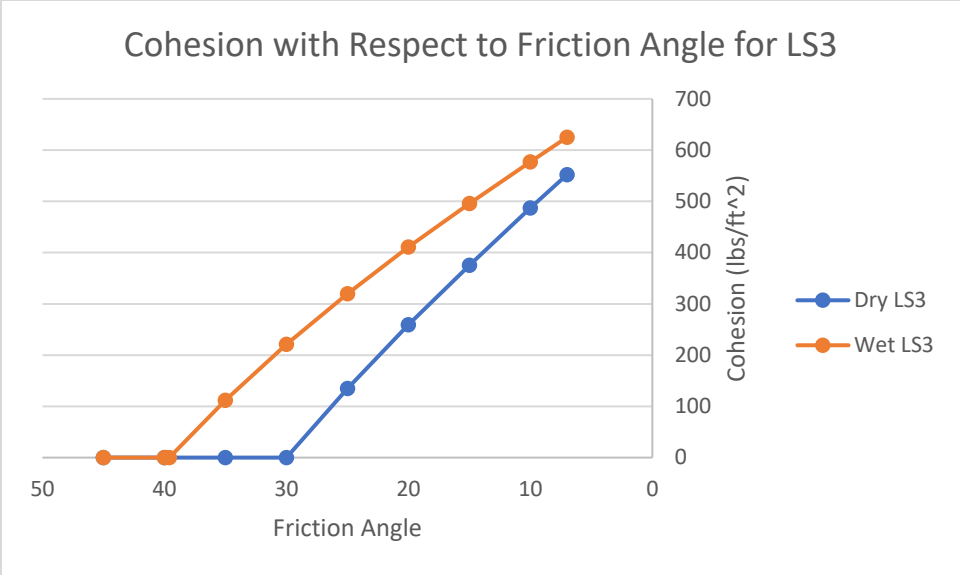

Figure 86: Values of cohesion and friction needed to maintain a safety factor of 1 for LS3.

Table 12 and Figure 87 show the effects of an increase of $10m^2$ on cohesion values in comparison to what was originally calculated initially. This increase in area was chosen in case some of the surface area was not visible. A decrease in the cohesion needed was observed.

LS3					
Area m^2	Height m	Radius m	Volume m^3	Volume with Porosity	Max P Water
50.88	2.8	9.18	155.9	109.13	572.832
Area ft^2	Volume ft^3	Weight constant	Weight lbs	θ	Avg P Water
547.67232	3853.93	160	616628.15	30	286.416
Water Constant	Height Fracture ft	Width ft	Distance ft		Tension Force Water
62.4	7.5	2	48.5		22698
Dry			Wet		
Friction Angle	Cohesion lbs/ft^2	Safety Factor	Friction Angle	Cohesion lbs/ft^2	Safety Factor
45	0	1.73	45	0	1.11
40	0	1.45	42	0	1.00
35	0	1.21	40	38	1.00
30	0	1.00	35	130	1.00
25	108	1.00	30	210	1.00
20	208	1.00	25	283	1.00
15	302	1.00	20	351	1.00
10	391	1.00	15	414	1.00
7	443	1.00	10	474	1.00
			7	509	1.00

Table 12: Adjusted values for a larger slide surface area.

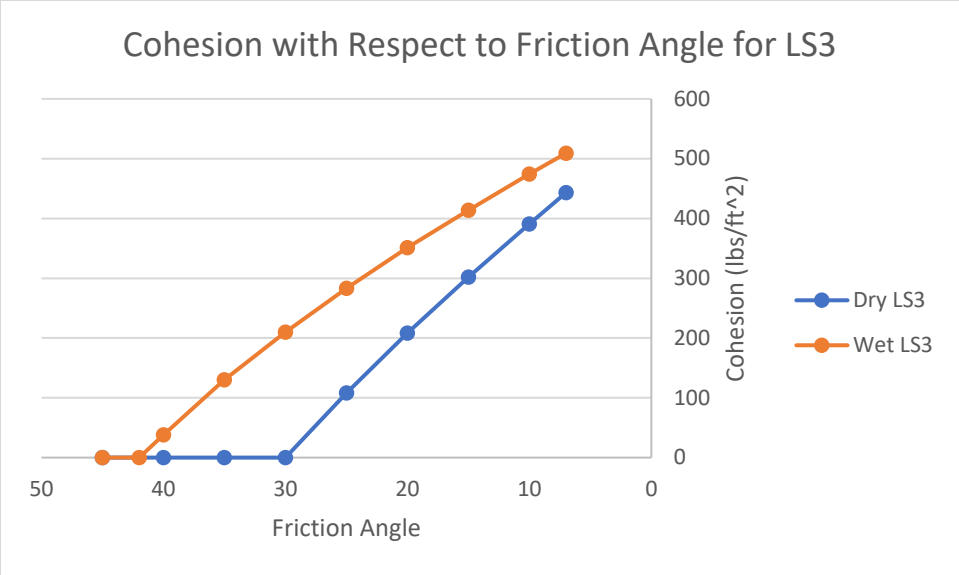

Figure 87: Adjusted graph for an increase in 10m^2 of surface area.

Landslide 3 failed along a surface with a dip (θ) of approximately 30 degrees which is about equivalent with the dip of foliation. Foliations were daylighting on this northernmost slide which did have some fractures along the foliation planes. If the rock was blocky instead of having fractures along the foliation planes, a friction angle (Φ) 40 degrees instead of the 30 would have been applied. No epidote was seen up high, but the cohesion values needed for stability were 135 lbs/ft^2 (6.46 kN/m^2) under dry conditions and 320 lbs/ft^2 (15.32 kN/m^2) under wet conditions if epidote was present causing the angle of internal friction of failure to be 25 degrees under the measured area. Appendix B confirms that these lower values of cohesion are to be expected for infilled fractures. Cohesion was needed earlier for wet conditions to keep the safety factor one by an angle of internal friction of about 39.6 degrees which is to be expected due to the hydrostatic pressure which acts in the opposite direction of weight. An increase in the surface area of the slide surface to account for some potentially buried slide surface caused for lower

cohesion values to be observed in comparison to those calculations based off the area calculated from ArcGIS.

CHAPTER 5: INTERPRETATION AND DISCUSSION OF RESULTS

I discuss below the results that were derived using various methods in relationship with my proposed hypothesis: Specially orientated fracture and fault systems are the cause of repeated small-scale failures along Mt. Baldy Road. Back calculation of the different safety factor equations can yield reasonable shear strength parameters for C and Φ which will allow for seeing how these variables affect the safety factor itself. All five of the research questions will be addressed in this section along with all safety factor calculations.

1. What are the predominant fracture orientations along the road cut at each of the failure sites?

Fracture orientations play a key role in whether or not any surfaces would be able to fail along Mt. Baldy Road as they are the main driving force behind many of the smaller landslides observed in the area. Some of these would be orientated in such a way that they would be into slope, causing the surface to not be able to fail since it was supported by the material all around it ensuring a high safety factor no matter what the conditions of the rock were. Susceptibility of failure was reliant on both the orientation of the fractures along with the orientation of the roadcut which varied slightly depending on the location of where the measurements were. Another thing which needed to be considered were the interactions between these fracture surfaces and if they had the potential to be jointed or orientated in such a way that it could promote other small-scale landslides.

The fractures which were of the most interest were the ones which had a daylighting orientation in relationship to the road cut on the western side of Mt. Baldy Road. Daylighting fractures are inclined toward the road at a shallower dip then the roadcut and

strike near parallel to the cut. Foliations to the south of LS3 were mostly orientated in such a way that they were not in the daylighting envelop (Fig. 48) so they would be ignored for the planar landslide failure type. However, in an around LS3 they were orientated in such a way where fractures were along the foliation plane and were also in a daylighting condition so planar failure was possible (Fig. 56).

For both LS1 and LS2, the wedge axis for the intersection between the foliations that dip to the southwest and the fractures which dip to the northeast (Figs. 48 & 53) goes out of slope in comparison to the roadcut. Such a trend with the interactions between these two features is prevalent in not only the area on the landslides but also to the south of LS1 (Fig. 52).

Underneath the outlook, fracture patterns (shown in black) were less consistent though there were still a high concentration of them that dipped towards the northeast in comparison to the other directions which is consistent with what has been notated around the field site (Fig. 57). Some of the blocks which were measured seemed to have been slightly out of place which most likely accounts for the one which dipped to the southwest. The ones which dipped to the southeast where a few that seemed to be unique and were not the norm to characterize this area as a whole. An overall assessment of the outlook in comparison to the fire escape road (green) reveals that very few of these fractures are orientated in a way which would be considered daylighting posing minimal risk to the area below.

2. Can past landslides be modeled as simple plane, wedge, or complex combinations of these?

All the past landslides which were studied during this thesis seemed to be able to be modeled as simple plane or wedge landslides, using approaches of Hoek and Bray 1981 and Wyllie and Mah 2004. This does not mean that there are other potential slides that are difficult to access which could fall under complex combinations of these slides. LS1 and LS2 could only be modeled as a wedge slide because of the geometry of the two slide planes is not daylighting, so the calculation and modeling reflected it. LS3 in contrast only had one visible plane of failure without containing a steep enough dip in conjunction with a secondary failure plane to create the necessary environment to allow for a wedge shape to form. There is always the potential for another slide in the future to contain characteristics of both which would complicate the modeling process along with safety factor calculations.

3. What are the likely quantitative effects of water saturation during heavy storm events?

It is no surprise that water plays a critical role in the failure points for the various slides no matter what type of slide it is. With the number of fractures that are present along the rocks, water would have the ability to infiltrate through until it finds a plane which is orientated correctly to induce a failure. Water creates a hydrostatic force which is in the opposite direction of the weight of the rock mass above, decreasing the overall normal stress that the rock places against the plane of the potential slide surface. Heavier rainstorms could create events where so much water percolates into the slide plane that it induces a failure at a lower dip of slide plane or shallower plunge of wedge axis than that which would be expected. For instance, something which may ordinarily be stable at up to 40 degrees of dip would instead be able to fail in a way that could be considered unexpected since the driving stress has been increased to the point of failure.

When the safety factor is already at one, reducing the Φ value would cause for failure to occur at an earlier point. Cohesion would need to be increased in order to compensate for the friction angle decreasing substantially due to the presence of water. This is observed in Table 9 for the wedge case where stability was lost sooner so cohesion was needed in order to create a safety factor of 1 which is at the point where failures can happen.

Looking at the Mt. Baldy area, some years in the last 100 years have had months with heavy precipitation as seen from a historic database provided by NOAA. Some months scattered from 1926 through 2020 where the last nearby station was still recording precipitation values recorded upwards of 10 inches of rain and/or 20 inches of snow on a single day. Such extreme precipitation values are sure to have an effect on the amount of water going into the fractures as well as the spaces in foliations where it applies. A critical thing to note is that many of these events occurred during the winter months where temperatures are often below freezing during the evening hours and during some colder days. Freezing of water causes fractures to crack open more through the process of expansion of water as it turns into ice, wedging into the rock and causing fractures to propagate into previously unfractured rock while also causing the original fracture to grow in width. There is an additional potential as water which had made it to the slide planes could freeze so that it creates an additional driving stress which could overcome the resisting stress of the rock.

01/31/2019	0.58	1
02/01/2019	0.02	1
02/02/2019	3.57	1
02/03/2019	1.24	1
02/04/2019	2.86	1
02/05/2019	0.61	1
02/06/2019	0.04	1

Table 13: Sample of precipitation in inches provided by Steven Chang from LACPW for the Sierra Powerhouse daily from gauge#619 during part of my study period.

4. What are the appropriate safety factor equations to use in different situations?

Several safety factor equations were used for both the wedge and planar slide situations in this thesis due to having to test under different conditions. One wedge equation was appropriate for times only friction was the resisting force, one for when there was cohesion and one for wet conditions. Same conditions applied for the planar landslide except cohesion was in both equations so there were only two of them that were needed to solve for. All things are solved for using procedures from Hoek and Bray, 1981 and from Wyllie and Mah, 2004.

5.1 Wedge Under Friction Only

This case analyzes when the wedge is only held in place by friction (cohesion = 0) and that both friction angles are the same (friction angle represented by Φ) on the two planes. The side view (Fig. 24) shows the angles of how weight is distributed by the forces with ψi representing the angle of dip of the slide surface at the axis. ξ represents the angle between the two planes as β is the angle from horizontal to ½ of ξ. R_A and R_B represent the normal reactions of planes A and B with A always being the plane with a shallower dip (Figs. 48&49). Three equation components were used to solve for this. $FS = \frac{(R_A+R_B)tan\Phi}{Wsin\psi_i}$

and $R_A + R_B = \frac{W*cos\psi_i*sin\beta}{sin\frac{1}{2}\xi}$ (Hoek and Bray, 1981) with it simplifying to $FS = \frac{sin\beta}{\sin(\frac{\xi}{2})} * \frac{tan\Phi}{tan\psi_i}$ (Wyllie and Mah, 2004). These were solved for the factor of safety for this instance.

5.2 Wedge with Friction, Cohesion, and/or Water

With more variables comes many more equations and constants to solve for. This is a much more complex problem due to the nature of the various new parameters that need to be taken account of along with new constants that are dependent on the orientation and interaction between the slide surfaces and the road cut. It is important to annotate everything accurately or else have calculations become difficult to follow. Fig. 26 shows the different angles which need to be measured between points on a stereonet. This was done on the stereonet 11 program which has a feature to measure the angle between planes. Factor of safety was calculated with the following equation:

$$F = \frac{3c_A}{\gamma H} \cdot X + \frac{3c_B}{\gamma H} \cdot Y + (A - \frac{\gamma_w}{2\gamma} \cdot X)Tan\phi_A + (B - \frac{\gamma_w}{2\gamma} \cdot Y)Tan\phi_B$$

Variables c_A and c_B are the cohesive strengths of planes A and B. Φ_A and Φ_B are the friction angles of planes A and B. γ is the unit weight of rock while γ_W is the unit weight of water. H is the total height of the wedge. X, Y, A, and B are dimensionless factors which would be solved for by the following equations.

$$A = \frac{cos\psi_a - cos\psi_b * cos\theta_{na.nb}}{sin\psi_5 * sin^2\theta_{na.nb}}$$

$$B = \frac{cos\psi_b - cos\psi_a * cos\theta_{na.nb}}{sin\psi_5 * sin^2\theta_{na.nb}}$$

$$X = \frac{sin\theta_{24}}{sin\theta_{45} * cos\theta_{2.na}}$$

$$Y = \frac{sin\theta_{13}}{sin\theta_{35} * cos\theta_{1.nb}}$$

5.3 Planar Landslides

Two equations were used to calculate the safety factor: (1) one under dry conditions with cohesion, (2) the other involving the presence of water. Under dry conditions the equation is as follows: $SF = \frac{Resisting\ Stress}{Driving\ Stress} = \frac{C+tan\Phi[\frac{(Weight)cos\theta}{Area}]}{\frac{(Weight)sin\theta}{Area}}$ with C representing cohesion, Φ representing the angle of friction and θ the dip of the failure plane. These also apply to the following equation with weight and area also being constant. Under wet conditions the equation is as follows: $SF = \frac{Resisting\ Stress}{Driving\ Stress} = \frac{C+tan\Phi[\frac{(W)cos\theta - F_{H2O}\sin(50)}{A} - average\ P_{H2O}Up]}{\frac{(W)sin\theta + F_{H2O}\cos(50)}{A}}$ with the added variable $P_{H2O}Up$ representing the pressure of water acting upward along the slide surface and F_{H2O} as the force of water acting in a tension crack. Pressure is generally thought to be at about 1/3 of the pressure of the normal stress component of the weight of the slide mass on top.

5. What terms of the safety factor equations can be directly measured or reasonably estimated?

All terms from the equations above can be either directly measured or reasonably estimated except for the ones involving cohesion and angle of friction. The reason is that many of the dips can be thoroughly analyzed using stereonets which are based off of a multitude of field measurements. Height of the landslides were measured by the use of a laser rangefinder giving a good estimate of it as well as using plotted measurements in ArcGIS to give approximate values for the area of the failure plane. Measurement of the

cone from these landslides using the laser rangefinder allowed the volume of the failure material to be calculated assuming a 30% porosity with the alternative method being used in the wedge to use ArcGIS to approximate the volume missing from that landslide. Weight was then be approximated using the volume of material and knowing that the plutonic and metamorphic rock averages at about 160 lb/ft^3. Dip of the planes can be sighted reasonably or measured directly on the surface.

Cohesion and friction angles are the only slope stability parameters which cannot be directly measured in the field. A range of possible values may be obtained from tables in Hoek and Bray (1981) or from rock mechanics experiments summarized by Wyllie and Mah (2004) (Appendix B). Another way in which to find the values of these numbers is through back calculation from the safety factor so that it equals 1 to find the point at which failure can occur. This was a key objective of my SF modeling performed in the previous section—to determine a range of likely C and phi values corresponding to failure under dry and water saturated conditions.

CONCLUSIONS

I studied three landslide sites (LS1, LS2 and LS3) along the Mt. Baldy Road. Analyzed data included Brunton compass measurements (foliations, fractures, joints, epidote surfaces and faults), stereonet plots of fracture orientations, laser rangefinder surveying and referencing of past photographs yielded. The following conclusions are made about the stability of features as well as the modeling of landslides:

- Each landslide happened along daylighting features and/or foliations that formed either translational or wedge landslides. Composition and roughness of the slide surfaces affected what angle of dip (for plane failure) or inclination (for wedge failure) was needed to cause a safety factor of one. These factors are shown in Plates 2-6 that have done studies on the effect of infillings and heavy weathering on rocks.
- Stereonet plots aided in evaluating what orientations of fractures and foliations were unstable with respect to the roadcut at each of the three landslide sites. along with respect to the road cut. For the wedge failure at LS1, the mean strikes and dips of the foliations was 119/49 and for the fractures was 343/52. The mean strikes and dips associated with the wedge failure of LS2 were 115/41 for foliations and 6/41 for fractures. For the plane failure LS3, the mean strikes and dips associated with it is 60/30.
- All measurements were taken on either quartz diorite or felsic gneiss. The felsic gneiss seemed to be the one which was more prone to fractures in both orientation of foliation and in the other orientation mentioned above.
- Volumes for LS2 and LS3 were determined from debris cones surveyed by laser rangefinder. These could be slightly different from true because measurement

points were based off previous photographs of the landslides that had been cleared away.

- ArcGIS proved to be a reliable method by which the volume of a void within a known landslide failure area could be calculated directly without the use of a debris cone. High amounts of points recorded by a laser rangefinder which are imported into GIS via Excel allow for the program to create a high-resolution model of the area of interest so that further calculations in the program could be done. Using the outside points along the edge of the landslide let the program create a surface that closely approximated the original one and calculate the volume missing between the hypothetical surface and the current one.
- Safety factor calculations yielded reasonable combinations of cohesion (C) and friction angle (Φ) for SF=1. For LS1 under dry conditions, C values ranged from 0 to 149 lbs/ft^2 and friction angles from 18 to 7 degrees respectively. Under wet conditions the C values ranged from 0 to 186 lbs/ft^2 (0 to 8.91 kN/m^2) for friction angles of 28.7 to 7 degrees respectively. LS2 under dry conditions had C values from 0 to 104 lbs/ft^2 (0 to 4.98 kN/m2) for friction angles of 23.3 to 7 degrees respectively, while under wet conditions C values ranged from 0 to 121 lbs/ft^2 (0 to 5.79 kN/m^2) for friction angles between 35.7 and 7 degrees. LS3 under dry conditions had C values from 0 to 552 lbs/ft^2 (0 to 26.43 kN/m^2) for friction angles of 30 to 7 degrees respectively, while under wet conditions C values ranged from 0 to 625 lbs/ft^2 (0 to 29.93 kN/m^2) for friction angles between 39.6 and 7 degrees with an area of 440 ft^2 (40.88 m^2). Applying an area of 548 ft^2 (50.88 m^2), LS3 had under dry conditions C values from 0 to 443 lbs/ft^2 (0 to 21.21 kN/m^2) for friction

angles of 30 to 7 degrees respectively, while under wet conditions C values ranged from 0 to 509 lbs/ft^2 (0 to 24.37 kN/m^2) for friction angles of 42 to 7 degrees. All cohesion values when compared to what was expected from Plates 2-6 seem to be reasonable as lower cohesion values are observed in different conditions.

- Fractures that both crosscut and followed the foliation planes allowed for water to flow deeper into the rocks. This helped to facilitate the failures by lowering resisting stress, increasing driving stress, and/or reducing cohesion. Much of the precipitation can go into the fractures and begin processes which would weaken the resisting stresses that allowed for these slopes to have remained stable. Mechanical weathering done by the formation of ice in these fractures would widen them and lower cohesion. Chemical weathering associated with long term infiltration of water creates clay that would cause for a further decrease in the friction angle.

REFERENCES

Agliardi, Federico & Crosta, Giovanni & F, Meloni & Valle, Claudio & C, Rivolta. 2013, Structurally-controlled instability, damage and slope failure in a porphyry rock mass. Tectonophysics. 605. 34-47. 10.1016/j.tecto.2013.05.033.

Agumwah, Reginald, 2020, Geology and Fracture Geometry in Source Region of Hog Backk Landslide, Eastern San Gabriel Mountains, with Implications for Failure Mechanism [Master's Thesis]: California Polytechnic University, Pomona

Gschwind, Sophie, 2019, Multi-Stage Structural and Kinematic Analysis of a Retrogressive Rock Slope Instability Complex (Preonzo, Switzerland). Engineering geology. 252 (2019): 27–42.

Herber, Lawrence J., 1987, Hog Back: A Grossly Stable Prehistoric Translatory Rock Block Slide, San Antonio Canyon, Southern California. Geological Society of America Centennial Field Guide

Herber, Lawrence J., Hibner, Thomas H., Ressel Jr., Michael W., Vrabel, Craig, Rogers, J. David. 1991, Failure Mechanisms of Catastrophic Subalpine Paleolandslides in Crystalline Rock of the Central San Gabriel Mountains; San Antonio Canyon, Southern California. Geologic Society of America.

Hoek, H. and Bray, J.W. I981 Rock Slope Engineering. 3rd Edition, Institution of Mining and Metallurgy, London, 202 p.

Hoek, E., Kaiser, P.K., Bawden, W.F., 1995. Support of Underground Excavations in

Hard Rock. A.A. Balkema, Rotterdam, Netherlands

Kumar Raghuvanshi, Tarun. 2017. Plane failure in Rock slopes – A review on stability analysis techniques. Journal of King Saud University - Science. 10.1016/j.jksus.2017.06.004.

Morton, Douglas M., Miller, Fred K., 2003, Preliminary Geologic Map of the San Bernardino 30' x 60' Quadrangle, California: US Forest Service (San Bernardino National Forest) and the California Geological Survey, scale 1:100,000

Nourse, Jonathan A., Diblee, Thomas W., Jr., Weigand, Peter W., 2003, Late Cenozoic Magmatism, Faulting, Uplift, Flooding, and Erosion in the Eastern San Gabriel Mountains and Pomona Valley

Rogers, J. David, Herber, Lawrence J., Hibner, Thomas H., 1992, Paleolandslides in San Antonio Canyon, eastern San Gabriel Mountains, California. Association of Engineering Geologists: Sudbury, MA, United States.

Wicks, Logan, 2010, Failure Analysis of a Rockslide on Sunset Ridge Fire Access Road San Gabriel Mountains, California [Undergraduate Thesis]: California Polytechnic University, Pomona

Wyllie, Duncan C., Mah, Christopher W., 2004, Rock Slope Engineering Civil and Mining 4th Edition: Spon Press, p. 129-175

APPENDIX A

Compilation of ArcGIS data for a topographic map.

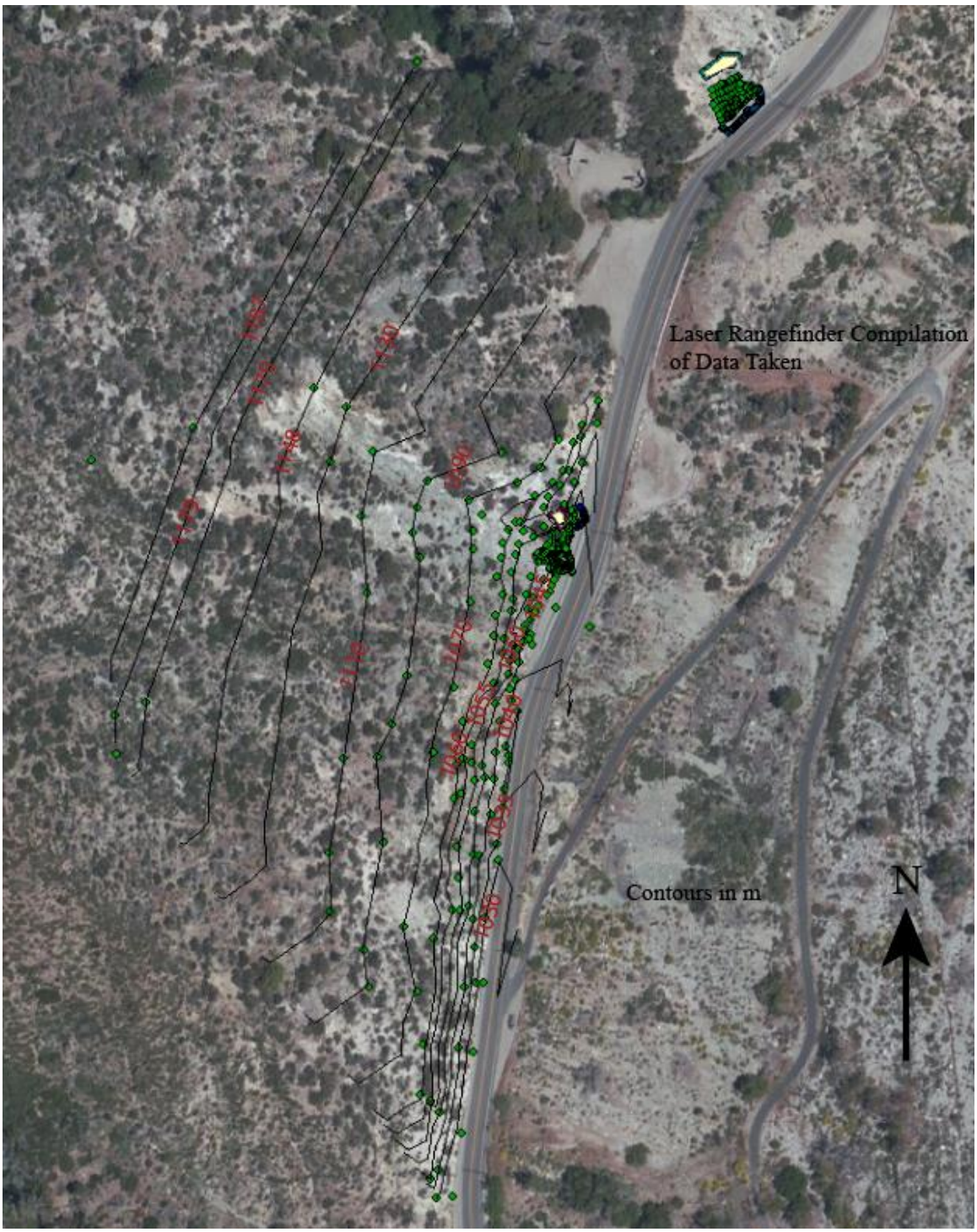

APPENDIX B

Table of Experimentally Determined Soil and Rock Properties

Based off graphs from Wyllie and Mah (2004). Infilled values from Barton (1970). Observed properties of whole rocks from different sources. Inspired by a table from Hoek and Bray (1981). Shows both measured values of specific rocks/infillings along with potential values of different clays and rocks. Values of specific rocks from previous studies cited alongside the measured properties.

Description			Friction Angle	Cohesion		Source of Values
Type		Material		lbs/ft^2	kN/m^2	
Cohesionless	Sand	Loose sand, uniform grain size	28-34			Hoek and Bray (1981)
		Dense sand, uniform grain size	32-40			“ ”
		Loose sand, mixed grain size	34-40			“ ”
		Dense sand, mixed grain size	38-46			“ ”
	Gravel	Gravel, uniform grain size	34-37			“ ”
		Sand and gravel, mixed grain size	45-48			“ ”
	Blasted/ broken rock	Basalt	40-50			“ ”
		Chalk	30-40			“ ”
		Granite	45-50			“ ”
		Limestone	35-40			“ ”
		Sandstone	35-45			“ ”
		Shale	30-35			“ ”
Cohesive	Clay	Soft bentonite	7-13	200-400	10-20	“ ”
		Bentonite/clay	8	366	17.5	Fleming et al. (1970)
		Very soft organic clay	12-16	200-600	10-30	Hoek and Bray (1981)
		Soft, slightly organic clay	22-27	400-100	20-50	“ ”
		Soft glacial clay	27-32	600-1500	30-70	“ ”
		Stiff glacial clay	30-32	1500-3000	70-150	“ ”
		Glacial till mixed grain size	32-35	3000-5000	150-250	“ ”
		London clay, stiff	21.5	317	15.2	Skempton and Hutchinson (1969)
		Clay shale	10	570	27.3	Middlebrook (1942)
		Clay shale	12	261	12.5	Fleming et al. (1970)
		Clay	21	1542	73.8	Fleming et al. (1970)
	Rock	Hard igneous rocks – granite, basalt, porphyry, diorite, andesite, rhyolite, gabbro	35-45	720000-1150000	35000-55000	Hoek and Bray (1981)
		Jointed porphyry	36	2873	137.6	Hoek (1970)
		Ore body hanging wall in granite rocks	42	10056	481.5	Hoek (1974)
		Rock slopes with slope angles of 50-60°	31	6338	303.5	Ross-Brown (1973)
		Faulted rhyolite	38	1232	59	Hamel (1971a)
		Kaolinized granite	35	324	15.5	Ley (1972)

		Weathered granites	38	761	36.4	Hoek and Richards (1974)
		Weathered volcanics	30	803	38.4	Hoek and Richards (1974)
		Metamorphic rocks – quartzite, gneiss, slate	30-40	400000-800000	20000-40000	Hoek and Bray (1981)
		Disturbed slates and quartzite's	34	824	39.5	Coates et al. (1965)
		Hard sedimentary rocks/soft metamorphic rock – limestone, dolomite, sandstone, conglomerate/schist, marble, phyllite	34-45	720000-1150000	35000-55000	Hoek and Bray (1981)
		Bedding planes in limestone	21	1993	95.4	Roberts and Hoek (1972)
		Sedimentary series	26	1127	54	Hamel (1971b)
		Soft sedimentary rock	25-35	20000-400000	1000-20000	Hoek and Bray (1981)
		Sandstone, siltstone	31	2049	98.1	Wyllie and Munn (1979)
		Argillite	29	1092	52.3	Wyllie (project files)
		Gravelly Alluvium	22	1218	58.3	Hamel (1970)
		Soil	32	289	13.8	Whitman and Bailey (1967)
		Chalk	42	800	38.3	Hutchinson (1970)
Infilled Material Properties						
Description			Friction angle	Cohesion		Source of values
Type		Material		lbs/ft2	kN/m2	
Cohesive	Material of infillings	Bentonite shale	18-28	2970-58833	142.2-281.7	Barton (1970)
		Bentonite shale seams in chalk	7	409	19.6	" "
		Bentonite; thin layers	11-16	1907-2569	91.3-123	" "
		Bentonite; triaxial tests	13	2109	101	" "
		Clay, over consolidated	12	136	6.5	" "
		Limestone, 10-20 mm clay infillings	15	2088	100	" "
		Lignite and underlying clay contact	14-17	336-700	16.1-33.5	" "
		Coal measures; clay mylonite seams	16	317	15.2	" "
		Limestone; <1 mm clay infillings	16	1117	53.5	" "
		Montmorillonite clay	13	7429	355.7	" "
		Montmorillonite; 80 mm clay seam in chalk	7-11	418-518	20-24.8	" "
		Schists/quartzites; stratification, thick clay	31	1117	53.5	" "
		Schists/quartzites; stratification, thick clay	31	7891	377.8	" "
		Basalt; clayey, basaltic breccia	41	5094	243.9	" "

		Clay shale; triaxial tests	31	1372	65.7	“ ”
		Dolomite; altered shale bed	15	881	42.2	“ ”
		Diorite/granodiorite; clay gouge	27	155	7.4	“ ”
		Granite; clay filled faults	24	155	7.4	“ ”
		Granite; sandy-loam fault fillings	40	1153	55.2	“ ”
		Granite; shear zone, rock and gouge	41	5094	243.9	“ ”
		Lignite/marl contact	10	2109	101	“ ”
		Limestone/marl/lignites; lignite layers	37	1817	87	“ ”
		Limestone; marlaceous joints	25	155	7.4	“ ”
		Quartz/kaolin/pyrolusite; remolded triaxial	35-37	1009-2015	48.3-96.5	“ ”
		Slates; finely laminated and altered	32	1145	54.8	“ ”
		Limestone; 10-20mm clay infillings	12	2471	118.3	“ ”

TABLE 1 - TYPICAL SOIL AND ROCK PROPERTIES

Description			Unit weight (Saturated/dry)		Friction angle	Cohesion	
Type		*Material*	*lb/ft³*	*kN/m³*	*degrees*	*lb/ft²*	*kPa*
Cohesionless	*Sand*	Loose sand , uniform grain size	118/90	19/14	28-34*		
		Dense sand, uniform grain size	130/109	21/17	32-40*		
		Loose sand, mixed grain size	124/99	20/16	34-40*		
		Dense sand, mixed grain size	135/116	21/18	38-46*		
	Gravel	Gravel, uniform grain size	140/130	22/20	34-37*		
		Sand and gravel, mixed grain size	120/110	19/17	48-45*		
	Blasted/broken rock	Basalt	140/110	22/17	40-50*		
		Chalk	80/62	13/10	30-40*		
		Granite	125/110	20/17	45-50*		
		Limestone	120/100	19/16	35-40*		
		Sandstone	110/80	17/13	35-45*		
		Shale	125/100	20/16	30-35*		
Cohesive	*Clay*	Soft bentonite	80/30	13/6	7-13	200-400	10-20
		Very soft organic clay	90/40	14/6	12-16	200-600	10-30
		Soft, slightly organic clay	100/60	16/10	22-27	400-1000	20-50
		Soft glacial clay	110/76	17/12	27-32	600-1500	30-70
		Stiff glacial clay	130/105	20/17	30-32	1500-3000	70-150
		Glacial till, mixed grain size	145/130	23/20	32-35	3000-5000	150-250
	Rock	Hard igneous rocks - granite, basalt, porphyry, diorite, andesite, rhyolite, gabbro	** 160 to 190	25 to 30	35-45	720000-1150000	35000-55000
		Metamorphic rocks - quartzite, gneiss, slate	160 to 180	25 to 28	30-40	400000-800000	20000-40000
		Hard sedimentary rocks/soft metamorphic rock limestone, dolomite, sandstone, conglomerate/schist, marble, phyllite	150 to 180	23 to 28	35-45	200000-600000	10000-30000
		Soft sedimentary rock - poorly cemented conglomerate or sandstone; coal, chalk, shale, evaporite, siltstone	110 to 150	17 to 23	25-35	20000 - 400000	1000-20000

Table 1 from Hoek and Bray (1981) showing various tested values of different materials.

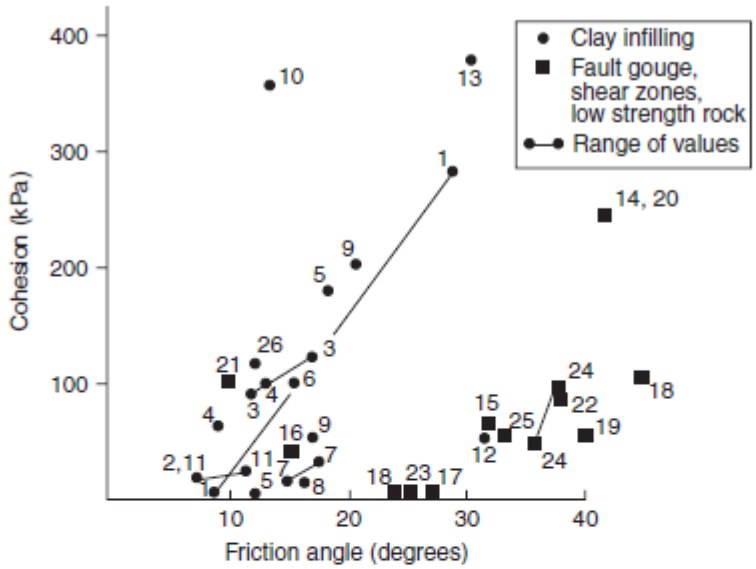

1. Bentonite shale
2. Bentonite seams in chalk
3. Bentonite; thin layers
4. Bentonite; triaxial tests
5. Clay, over consolidated
6. Limestone, 10–20 mm clay infillings
7. Lignite and underlying clay contact
8. Coal measures; clay mylonite seams
9. Limestone; <1 mm clay infillings
10. Montmorillonite clay
11. Montmorillonite; 80 mm clay seam in chalk
12. Schists/quartzites; stratification, thick clay
13. Schists/quartzites; stratification, thick clay
14. Basalt; clayey, basaltic breccia
15. Clay shale; triaxial tests
16. Dolomite, altered shale bed
17. Diorite/granodiorite; clay gouge
18. Granite; clay-filled faults
19. Granite; sandy-loam fault fillings
20. Granite; shear zone, rock and gouge
21. Lignite/marl contact
22. Limestone/marl/lignites; lignite layers
23. Limestone; marlaceous joints
24. Quartz/kaolin/pyrolusite; remolded triaxial
25. Slates; finely laminated and altered
26. Limestone; 10–20 mm clay infillings

Graph based on Barton (1970) showing different tested values of rocks with infillings or the infill material.

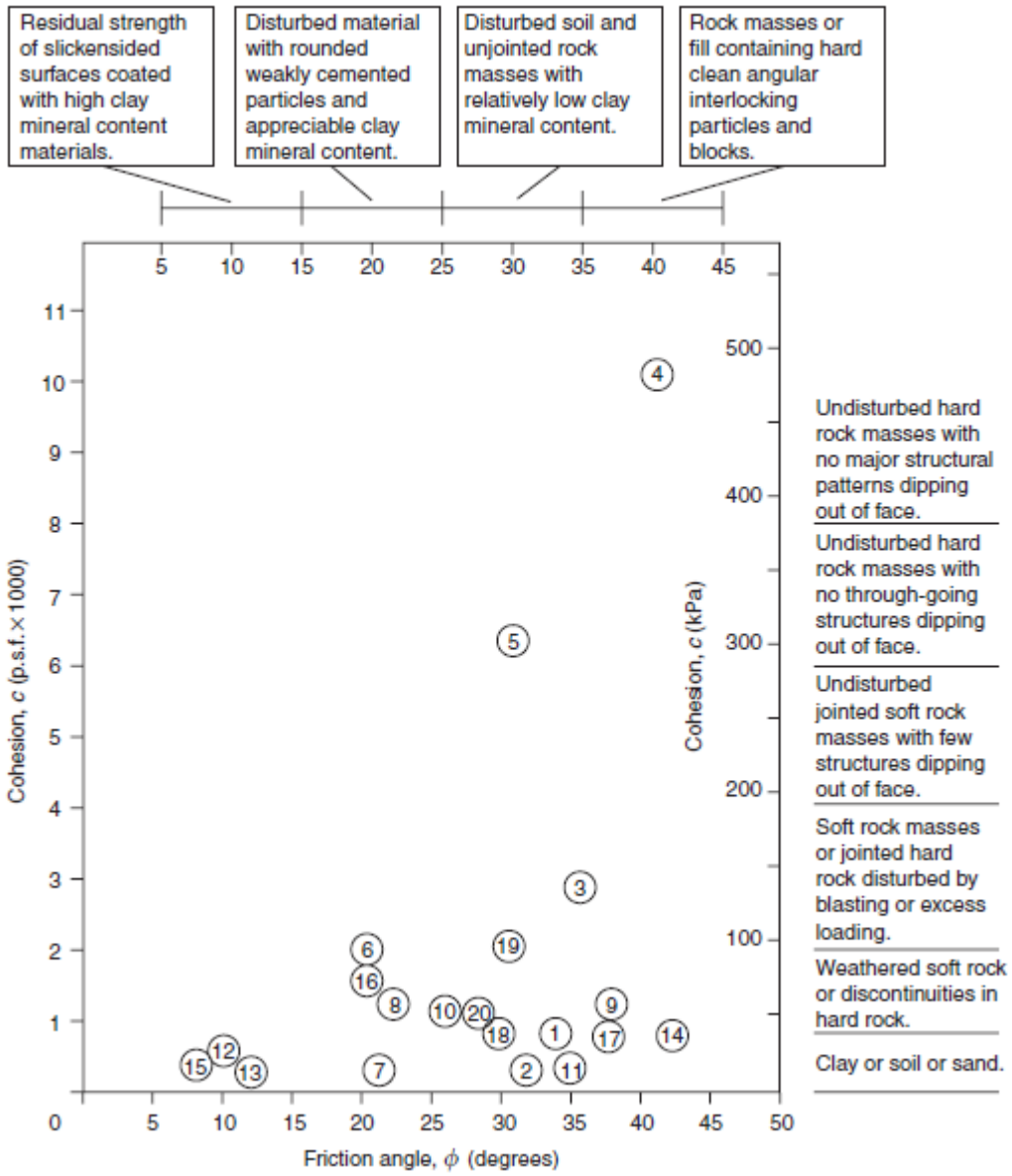

Graph based on research of whole rocks from various studies (Wyllie and Mah, 2004).

Point number	*Material*	*Location*	*Slope height (m)*	*Reference*
1	Disturbed slates and quartzite's	Knob Lake, Canada	—	Coates *et al.* (1965)
2	Soil	Any location	—	Whitman and Bailey (1967)
3	Jointed porphyry	Rio Tinto, Spain	50–110	Hoek (1970)
4	Ore body hanging wall in granite rocks	Grangesberg, Sweden	60–240	Hoek (1974)
5	Rock slopes with slope angles of 50–60°	Any location	300	Ross–Brown (1973)
6	Bedding planes in limestone	Somerset, England	60	Roberts and Hoek (1972)
7	London clay, stiff	England	—	Skempton and Hutchinson (1969)
8	Gravelly alluvium	Pima, Arizona	—	Hamel (1970)
9	Faulted rhyolite	Ruth, Nevada	—	Hamel (1971a)
10	Sedimentary series	Pittsburgh, Pennsylvania	—	Hamel (1971b)
11	Kaolinized granite	Cornwall, England	75	Ley (1972)
12	Clay shale	Fort Peck Dam, Montana	—	Middlebrook (1942)
13	Clay shale	Gardiner Dam, Canada	—	Fleming *et al.* (1970)
14	Chalk	Chalk Cliffs, England	15	Hutchinson (1970)
15	Bentonite/clay	Oahe Dam, South Dakota	—	Fleming *et al.* (1970)
16	Clay	Garrison Dam, North Dakota	—	Fleming *et al.* (1970)
17	Weathered granites	Hong Kong	13–30	Hoek and Richards (1974)
18	Weathered volcanics	Hong Kong	30–100	Hoek and Richards (1974)
19	Sandstone, siltstone	Alberta, Canada	240	Wyllie and Munn (1979)
20	Argillite	Yukon, Canada	100	Wyllie (project files)

Values for the table for plate 5 from Wyllie and Mah (2004).